POLITECNICO DI TORINO

Master’s Degree in Automotive Engineering

Master’s degree Thesis

NUMERICAL SIMULATIONS OF CAVITATION IN THE OIL PUMP AND THIN-FLUID-BEARING FOR AUTOMOTIVE APPLICATIONS

Supervisors	Candidate
Prof. Colombo Federico	Jiaqi Xu
Prof. Vesselina Roussinova	

October 2022

DECLARATION OF ORIGINALITY

I hereby certify that I am the sole author of this thesis and that no part of this thesis has been published or submitted for publication.

I certify that, to the best of my knowledge, my thesis does not infringe upon anyone's copyright nor violate any proprietary rights and that any ideas, techniques, quotations, or any other material from the work of other people included in my thesis, published or otherwise, are fully acknowledged in accordance with the standard referencing practices. Furthermore, to the extent that I have included copyrighted material that surpasses the bounds of fair dealing within the meaning of the Canada Copyright Act, I certify that I have obtained a written permission from the copyright owner(s) to include such material(s) in my thesis and have included copies of such copyright clearances to my appendix.

I declare that this is a true copy of my thesis, including any final revisions, as approved by my thesis committee and the Graduate Studies office, and that this thesis has not been submitted for a higher degree to any other University or Institution.

ABSTRACT

The cavitation in hydraulic pumps and fluid bearings could cause system instability, wearing, and failure. Modern commercial computational fluid dynamics (CFD) solvers such as Simerics Inc and GT-Suite have the capabilities of predicting cavitation. However, the fidelity and accuracy of those models require further evaluation. The aim of the thesis is to develop a methodology to improve the analysis of oil flow and cavitation in the oil circuit. The research project is conducted jointly by the University of Windsor and Politecnico di Torino. 3D CFD models of the vane pump and journal bearing are simulated using Simerics Inc to evaluate the cavitation and pump performance. The pump sensitivity tests of different eccentricity ring designs and gas fractions are conducted, and its corresponding influence on the effective flow rate is discussed. The 3D CFD model also predicts cavitation development inside the journal bearing clearance. The CFD model is validated using original equipment manufacturer (OEM) experimental data. The validated CFD results are converted into input for the 1D GT-Suite model to be integrated into the oil circuit model. This research developed the methodology to build a reliable oil circuit using a 1D approximation based on the high-fidelity 3D CFD simulations for the vane pump and bearings. It is concluded that this research demonstrates the cavitation prediction capability of the oil circuit components resulting in robust design of automotive components and systems.

.

DEDICATION

To my parents, Mr. Xu Yitao and Mrs. Zhang Zhizhen.

To the two years of my life

致我的父母徐以涛先生和张志珍女士

致我人生中的两年

ACKNOWLEDGEMENTS

I sincerely thank my academic advisor Prof. Colombo Federico and Prof. Vesselina Roussinova for their support. I benefit from their throughout guidance and suggestions. Their dedication to research is always a true inspiration to me.

Special thanks to Agostino Iorio, Marie Mills, and Owais Iqbal for their experience, supervision, and guidance. I will not complete this journey without their support and help. I also would like to thank my colleagues Eliana Russo, Shuran Cheng, Francesco Fortunato, and Cong Shen. They have provided valuable suggestions and helped me understand the concept of this project.

I would also acknowledge Doug Hunter and Rayhan Ahmed for their support. They provided valuable data and support to the completion of this thesis.

Thank University of Windsor and Politecnico di Torino for funding this program.

Thank SLPT automotive as the designer and tester of the variable displacement vane pump in this thesis, and for providing general support. - Acknowledgements

Last but not least, thank all my friends in Windsor, London, and Torino. Your friendship has always been the warmth to me in this difficult time.

TABLE OF CONTENTS

LIST OF TABLES

LIST OF APPENDICES

LIST OF FIGURES

Figures included in the APPENDICES

CHAPTER 1 Introduction

The hydraulic circuit is a critical component of the powertrain design in the automotive industry. The oil flow driven by the vane pumps and the oil circuit, including the journal bearing, is essential for vehicle operation. The durability and performance of the oil flow and pumps are critical for engine development. An important factor to maintain engine workability, durability, and efficiency is optimizing the oil flow through modeling to predict and prevent cavitation. Cavitation leads to large pressure changes in the fluid circuit, and the rapid pressure changes can result in excessive noise, oil starvation, and premature wearing. This research will investigate the performance of variable displacement vane pump and journal bearing, along with the effect of cavitation in these components.

Cavitation is the presence of vapor or gas bubbles inside the fluid. The liquid will transform into vapor when the local pressure drops below the vapor pressure; the gaseous cavitation occurs when the dissolved gas or small gas nuclei grows under low pressure. [1] Based on these two mechanisms, three types of cavitation are commonly observed: transient isolated cavities, sheet or cloud cavities, and vortex cavities. [2] [3] [4]. Singhal et al. [5] utilizes the Rayleigh-Plesset equation to propose a cavitation model that characterizes the vapor and liquid mass transfer on the bubble boundary when the vapor bubble develops. This model is implemented [6] and developed into the 3D CFD tool Simerics. The 1D simulation tool GT-suite, which adopts the lump parameter system, is also capable of CFD analyse. [7] The capability of these numerical tools to perform cavitation analysis of the vane pump and bearings are compared in this thesis.

The vane pump has been used as the automotive oil pump because of its advantages in handling gas-oil mixture and delivering low viscosity and high-temperature liquid. The conventional pump tends to deliver extra flow rate than required; however, the variable displacement vane pump can deliver the precise amount of flow rate as required by the downstream oil circuit. Consequently, this will reduce the amount of energy wasted and improve thermal efficiency. The main and connecting rod bearings are the critical components at the end of the oil circuit. The bearings require necessary oil from the upstream oil passage for lubrication and cooling, and therefore, the cavitation inside the pump or bearing will affect the oil delivery and functionality of the components.

The rest of the thesis consists of four chapters. Chapter two includes the literature review of the cavitation mechanism and types, the mechanism of variable displacement vane pump (VDVP), and the engine oil circuit leading to the journal bearings. The cavitation models implemented in the numerical simulation tools are also discussed. Chapter three explains the numerical procedures of the 3D and 1D models for the VDVP and bearings. Chapter four includes discussion of the results obtained from the 3D and 1D simulations. Furthermore, the results from the 3D and 1D models of VDVP are compared with the available experimental data. The pump's responses to different initial gas contents and eccentricity ring designs are discussed. In addition, the outlet flow rate, flow split between the main bearing and conrod bearing, and the visualization of cavitation development are included. Lastly, chapter provides summary of the key findings and ideas for future work.

CHAPTER 2 Objectives

The objective of this research is to analyze numerically the cavitation in the vane pump and fluid film bearings using 3D model using commercial CFD software Simerics Inc. The validated results such as volumetric flow rate vs. pump rotational speed are used to create a database and develop further a methodology for integrating them into the oil circuit using 1D GT-Suite model. The 3D model is used to establish a standard for cavitation assessment of vane pumps and bearings. Additionally, the models are validated with experimental data to ensure their accuracy. A methodology is developed to convert the validated Simerics 3D CFD models into 1D GT Suite models. Validation of the 1D pump and bearing models against experimental data are presented. The 1D models have more general applicability among different engine prototypes and agility in development with various requirements. The overall project can be divided into three main phases: 3D CFD cavitation simulations of the oil pump and journal bearing, validation of the cavitation models, and implementation of the 1D GT-Suite model for integration with the oil circuit model.

The detailed research sub-objectives are listed below:

I. Build a 3D CFD oil vane pump and journal bearings model using Simerics MP+ to analyze the cavitation.
II. Validate the vane pump model performance with available experimental data and establish the reference to alleviate the bearing and pump cavitation.
III. Develop a methodology to convert the bearing and pump 3D models into 1D GT-Suite models to be integrated with the oil circuit GT model.

I. *3D CFD oil vane pump and journal bearings models using Simerics MP+*

For the first and second sub-objective, the original equipment manufacturer (OEM) provides the CAD models and geometrical specifications of the vane pump and bearing models. From the CAD, 3D meshes are build and modeled with the commercial CFD tool Simerics MP+, where the cavitation at different rotational speeds and fluid properties are investigated. After the 3D geometry was imported into Simerics, the model was setup by creating the computational domain, defining the physical and fluid conditions: The fluid domain inside the vane pump is defined by the CAD surfaces including the inlet, chamber volume, rotating entities, and outlet. The pump chambers mesh is automatically generated after the geometrical parameters are entered such as the vane tip gaps, vanes number, etc. The grid of other domains is built with the binary tree hexahedral mesh. The last step of building the CFD model requires defining the operating, boundary inlet, outlet conditions, dynamics boundary conditions of the moving entities, and fluid properties. After building the model, the unsteady simulation is run with the optimized number of iterations and time steps. After the steady state is reached, the post-processing of the simulation results and validation of the simulation with available experimental data is performed.

The workflow and process of building a journal bearing model in Simerics are very similar to the one described for a vane pump model. The current journal bearing template available in Simerics is used along with the provided OEM geometry data to setup the geometry. The procedure of creating the computational domain, building the mesh, and defining the physics and operating conditions are similar to the one outlined above for the vane pump model. The bearing fluid domain is a thin fluid film between the journal and housing which requires careful meshing. The journal bearing template is used to mesh the inlet, outlet, and groove domain to create suitable mesh in the bearing. The fluid properties are entered based on the OEM data. After successfully performing the simulation, the results are post-processed and analyzed.

II. *Validation of pump performance model*

The experimental data are obtained from the OEM to validate the 3D CFD models. The 3D pump model is validated to ensure that the model can simulate different operating conditions. Specifically, the model is successfully validated once the post-processing simulation results including the outlet port pressure, delivery flow rate, etc. agree well with the experimental data. For the 3D bearing model, the comparison with the results from the 1D simulation at the same conditions is performed due to the lack of the available experimental data.

These models are utilized to predict the pumps and bearings performance and cavitation. Various post-processing methods are used: the pressure and velocity contours are employed to analyze the pressure and velocity distribution inside the pump. The vapor and gas volume fraction contours are used to visualize the cavitation development inside the pump and bearings. The 3D CFD models predict the average outlet pressure, flow rate, and cavitation volumes of the pump and bearing and can provide data for the overall pump performance. Additionally, different initial gas contents and designs are examined for the pump to determine their influence on cavitation. These parameters will be the reference to alleviate the pump and bearing cavitation for the prototype design and future research.

III. *Methodology to convert the 3D bearing and pump models to 1D model for integration into the oil circuit model*

Although the complete 3D CFD model has the advantage of providing detailed information for flow and cavitation, it is complicated and time-consuming to run. After detailed information for the flow, pressure, and cavitation inside the pump and bearing is obtained from the 3D CFD model, it is desired to switch to the 1D model where the pump and bearing models can be integrated with the entire oil circuit flow for large-scale analysis. This methodology completes the third sub-objective.

3.1 Mechanism of Cavitation

Cavitation is the presence of vapor bubbles inside a liquid medium. In engineering practice, this often includes the presence of dissolved gas in liquid such as mixture of air in pre-aerated oil. In general, the two macro-level cavitation mechanisms include gaseous cavitation and vaporous cavitation, and the micro-level cavitation mechanism are based on the bubble dynamics. The cavitation mechanism is different from the cavitation types, which will be discussed in the next section.

3.1.1 Gaseous cavities

The caseous occur in regions of low pressure because of the presence of small or dissolved gaseous nuclei within the liquid. Henry's law states the solubility of dissolved gas is proportional to the fluid pressure. The gaseous nuclei will grow under low pressure, become cavity, and collapsed under higher pressure. [1] The engine oil pan often contains certain amounts of oil foam, so the inlet of the oil pump might have a certain fraction of gas in the volume. The gas volume will expand during the suction phase when the pressure is low and will collapse on the delivery side of the pump when the pressure is significantly higher. This phenomenon is observed in the experiments and appears also in the simulation.

3.1.2 Vaporous cavitation

The vaporous cavitation occurs whenever the pressure within the liquid is less or equal to the saturation vapor pressure of the liquid. Vapor cavities spontaneously form within the liquid due to an abruptly change of fluid movement, and the momentum of fluid will cause the local fluid pressure lower than the saturation vapor pressure of the liquid. Alternatively, the local pressure fluctuation sometimes drops below the vapor pressure. Either case can force the formation of vapor cavities. In practice, the engine oil contaminated with water tend to experience more vapor cavitation as the absolute vapor pressure of water is higher than oil vapor pressure over the operation temperature 20-140°C. [8]

The fluid considered in this study is SAE OW-20 oil. Depending on the conditions, the gaseous cavitation usually happens before vaporous cavitation. In extreme cases, both gaseous and vaporous cavitation could occur.

As the bubbles burst, two primary phenomena occur almost immediately. [9] The first phenomenon is observed as the bubble interact with the solid wall during implosion, creating a ring-shaped size and introducing a micro jet. Secondly, due to the pressure wave formed by the implosion, the cavitation bubbles will affect and damage the material surface of the pump internals. Over time, if not properly handled, a reduction in efficiency, noise, vibrations, and ultimately, pump failure will increase the budget over time for replacement costs.

The gaseous and vaporous cavitations are cavitation mechanisms occurring at the macro level. This micro-level mechanism includes the bubble dynamics model, which should describe the bubble's behavior in detail.

3.1.3 Bubble dynamics

The bubble dynamics in the cavitating flows must account for bubble growth and collapse. In a flowing liquid with zero slip between the fluid and the bubbles, the bubble dynamics is described by the generalized Rayleigh-Plesset equation. [10]

$$R\frac{d^2R}{dt^2}+\frac{3}{2}\left(\frac{dR}{dt}\right)^2+\frac{4v_L}{R}\frac{dR}{dt}+\frac{2\gamma}{\rho_L R}+\frac{\Delta P(t)}{\rho_L}=0 \qquad (1)$$

where, ρ_L is the density of the liquid assumed to be constant, $R(t)$ is the radius of the bubble, v_L is the kinematic viscosity of the liquid, γ is the surface tension of the bubble-liquid interface and $\Delta P(t)=P_\infty(t)-P_b(t)$, in which $P_b(t)$ is the pressure within the bubble assumed to be uniform and $P_\infty(t)$ is the external liquid pressure infinitely away from the bubble.

Arndt's [10] has studied the relationship between these variables and the formation of cavitation bubbles. Since this research focuses on the macro-level cavitation instead of bubble dynamics, the topic of bubble dynamics will not be further discussed in this thesis.

3.2 Cavitation Types

There are three main types of cavitation that are commonly observed and discussed in the literature. They depend on the flow conditions and fluid properties.

3.2.1 Transient isolated cavities (or gaseous cavities)

The transient isolated cavities occur in regions of low pressure as a result of present small or dissolved gaseous nuclei within the liquid. The phenomenon is widely observed in hydraulic applications such as positive displacement pumps and thin fluid bearings. In experiments with hydrofoils, the nuclei grow into isolated bubbles and move along the hydrofoil surface in the free stream velocity. This phenomenon is sometimes referred as travelling bubbles as well. As the Fig. 3.1 below shows, the bubbles are no longer spherical when they collapse. A microjet develops at where the arrow is pointing and forces the bubble into a toroidal shape. When the microjet penetrates the bubble and reaches the surface, it creates a micro shockwave. This is one of the reasons of surface erosion.

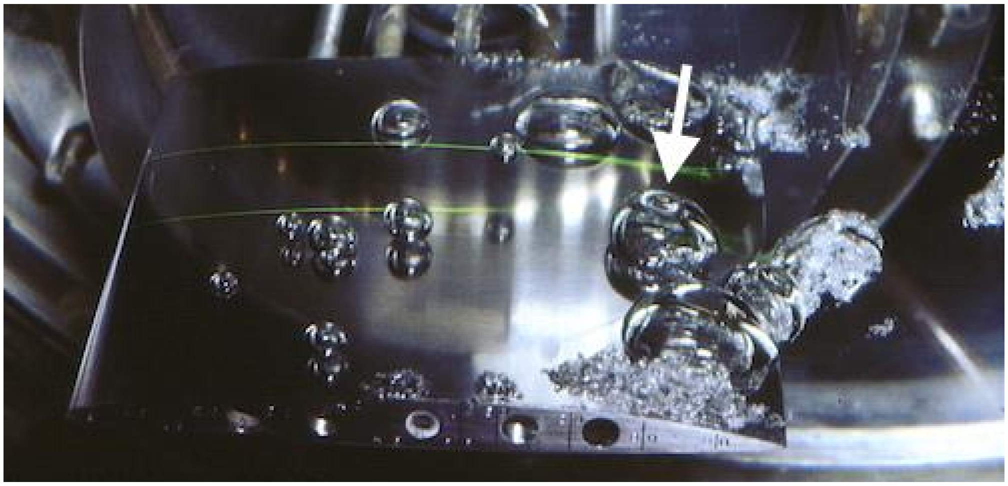

Fig. 3.1 Travelling bubbles on the surface of hydrofoil [3]

3.2.2 Sheet or cloud cavities

The sheet or cloud cavities present as large non-uniform cavities. They often occur in the vane pump or turbine blade, and they attach to the leading edges of moving mechanical components. The sheet or attached cavitation are also observed in the experiments with hydrofoils, where the small, attached cavities merge and extend to a longer form as sheet cavitation. Depending on the rate of bubbles formation and collapse, the length of sheet cavitation can be more or less. The circulation flow around the body can form a reverse flow/re-entrant jet that penetrates the sheet cavities. Then the shedding of sheet cavitation develops into cloud cavitation. The cloud cavitation is shown in the right figure below, where the sheet cavitation sheds into cloud cavitation and another cloud cavitation collapses near the trailing edge.

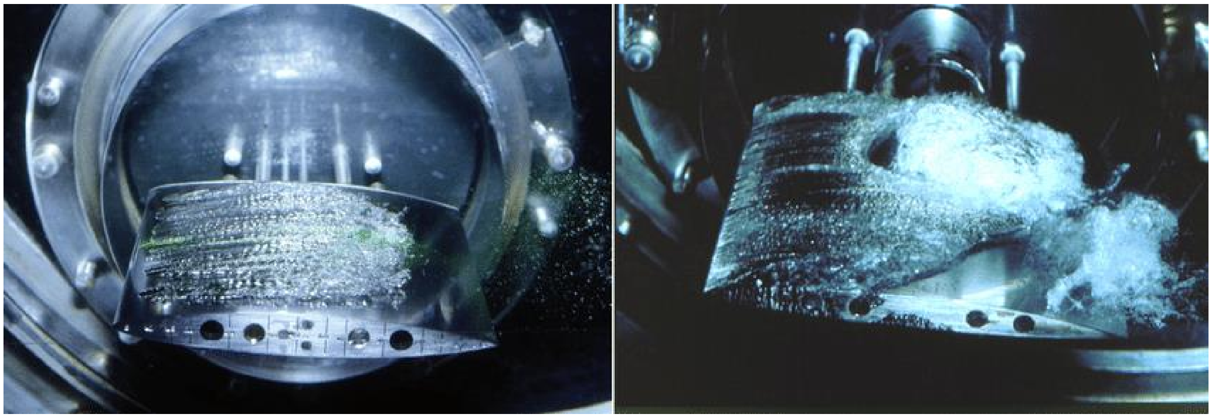

Fig. 3.2 Sheet and cloud cavitation on the hydrofoil [2]

3.2.3 Cavitating vortices

The cavitating cortices appear in the low-pressure core of vortices in the wakes of turbulent flows. It is commonly observed at the tip of ship propeller blades. Because of the clearance between blade and housing, the leakage flow generates vorticity near the blade-tip as it rolls up the blade and passes the clearance duct. The tip leakage vortex often develops into cavitation vortices on the suction side of the pump. The figure below shows vortex cavitation on the hub and at the tip of the blades on a scaled propeller model. [4]

The hub cavitation is due to the center low pressure zoom from fluid rotation, and the tip cavitation is caused by tip vortex.

Fig. 3.3 Hub and the blade tip vortex cavitation [4]

3.3 Pump

There are three basic types of pumps: positive-displacement, centrifugal and axial-flow pumps. A positive-displacement pump makes a fluid move by trapping a fixed amount and forcing (displacing) that trapped volume into the discharge port. As one of the positive-displacement pumps, the vane pump has been commonly used for automotive engine oil delivery due to its capability of handling liquid containing mixture of liquid and gas, as well as delivering low viscosity fluid at high temperature.

3.3.1 The traditional vane pump

The traditional vane pump is driven by the engine shaft and has fixed displacement. The figure below shows a schematic of the pump including the shaft which drive the vane in a rotational motion. The vanes pump housing and rotor form several vane chambers that the fluid can enter and exit. The vanes are retractable to provide proper sealing for each chamber. Due to the eccentricity between the shaft and housing center, each vane chamber has different volume at different angular position. The vane chambers on the inlet side have smaller volumes. As they rotate because of the drive shaft motion, their volume gradually increase and cause the local pressure to decrease, which leads to suction power. As the vane chambers move to the delivery side, their volume decrease, which causes the local pressure to increase and provides delivery flow and pressure.

The schematics in below show the vane pump with different eccentricities. The high eccentricity causes more chamber volume variation, which leads to a higher displacement.

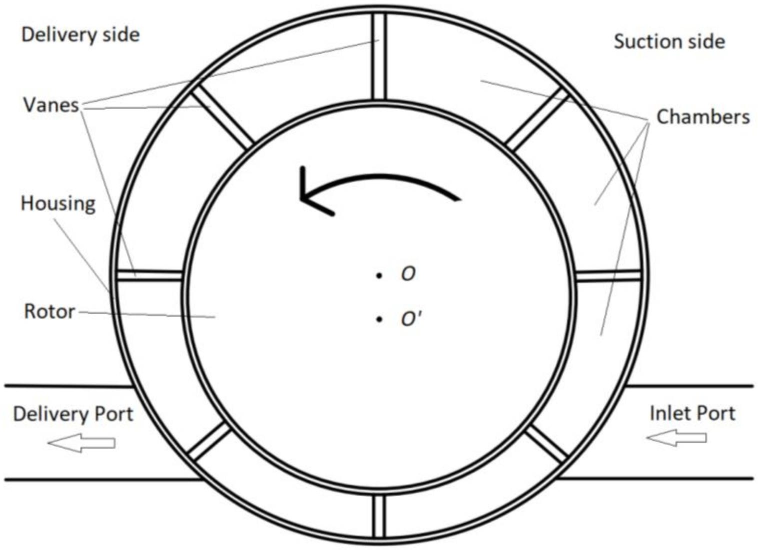

Fig. 3.4 Schematic of vane pump with low eccentricity

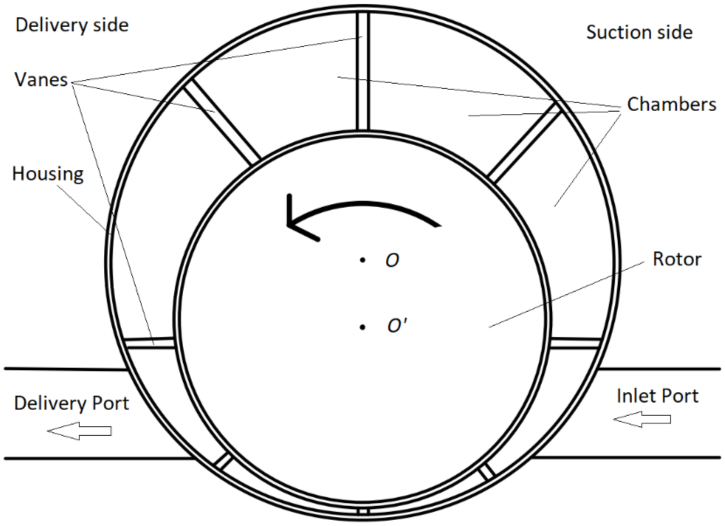

Fig. 3.5 Schematic of vane pump with higher eccentricity

The conventional vane pump must deliver excessive flow and pressure to meet the operation target during the operating engine rpm range. The excessive flow must be discharged by the pressure relief valve. As a result, it wastes energy and affects thermal efficiency improvement. To be more adaptive to various oil targets, a better solution as a variable displacement vane pump is sought.

3.3.2 Variable displacement vane pump (VDVP)

The geometry of variable displacement vane pump (VDVP) is adapted from the conventional vane pump. Comparing to the conventional vane pump, the VDVP has an additional eccentricity ring (often referred as E-ring or Cam-ring) adjacent to the chamber housing. Similarly, to the vane pump, the VDVP still relies on the eccentricity and rotation motion to generate suction and delivery power. However, the eccentricity can be adjusted so that it can provides different displacement, which leads to various delivery flow rate. As the figure Fig. 3.6 and

Fig. 3.7 show, the eccentricity of the cam-ring is controlled by the mechanical or hydraulic mechanism, so that the displacement can vary based on the user's need.

3.3.2.1 Pivoting type

As figure Fig. 3.6 shows, the displacement of pivoting VDVP is decided by the rotation of the eccentricity ring. As it rotates about the pivot point clockwise, it will push the entire chamber downward. Consequently, the chamber center O moves closer to the rotor center O', and the eccentricity decrease. Therefore, clockwise rotation of the E-ring will decrease the eccentricity and displacement. Counter-clockwise rotation of the E-ring will increase the eccentricity and the displacement. Under steady operation conditions, the angular position of the E-ring is a result of force balance of the external force F, spring force, and the fluid force on the E-ring. Under dynamic operation conditions, the friction force also needs to be included. The details are discussed in the modelling section. The external force F can be applied by a mechanical or hydraulic entity and controlled by the user. Therefore, users can control the pump displacement by using external force to control the E-ring position.

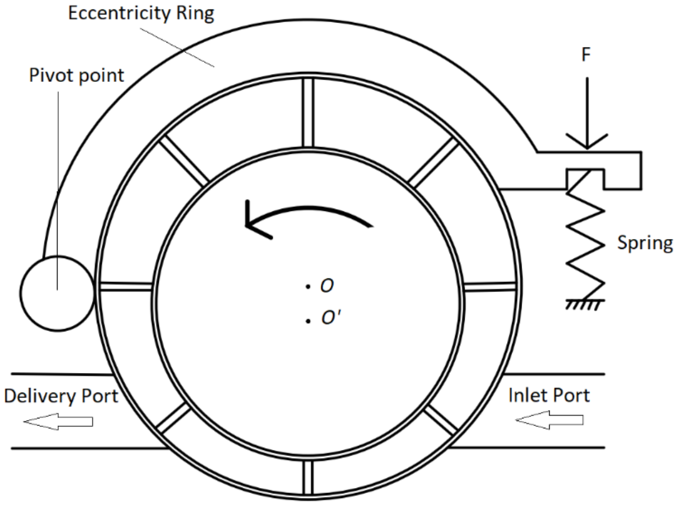

Fig. 3.6 Variable displacement vane pump: pivoting type

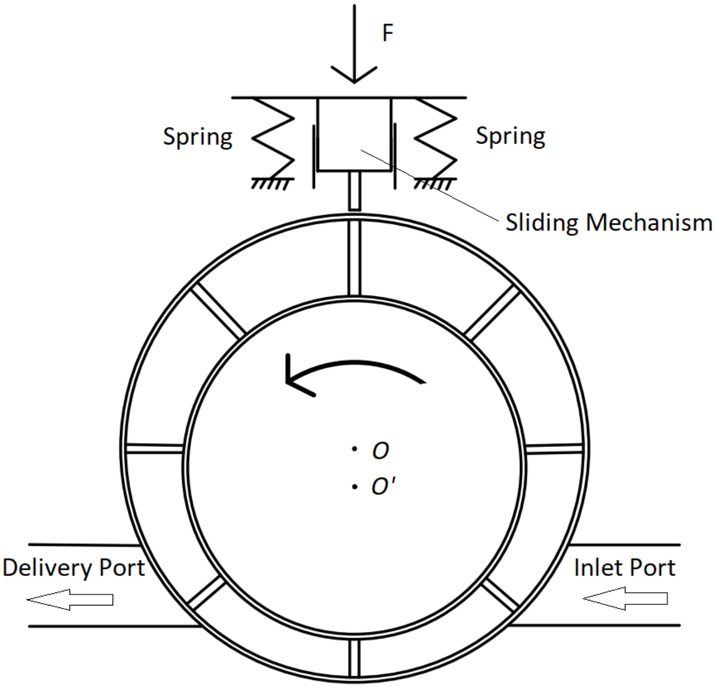

Fig. 3.7 Variable displacement vane pump: sliding type

3.3.2.2 Sliding type

The sliding VDVP uses a sliding mechanism to control the pump displacement. As an external force is applied, the sliding mechanism will push the chamber housing downward. The downward movement of chamber center O and decrease of eccentricity will lead to decrease of displacement. If the spring force restore the mechanism to the original position, the displacement will increase.

There are various numerical studies of VDVP. Frosina et al [11] used a 3D computational fluid dynamic (CFD) software Simerics to simulate the sliding type variable vane pump in terms of P-Q performance, force balance and cavitation. This thesis will further expand on it with pivoting type variable displacement vane pump.

3.4 Engine lubrication system-wet sump circuit

There are mainly two types of lubrication for the internal combustion engine: the one with the flow generation unit and the one without the flow generation unit. Lubrication systems without flow generation units, including splash lubrication and mixture lubrication, are mainly for two-stroke engines or small four-stroke engines. The lubrication system with flow generation unit, which includes wet sump and dry sump design, is widely applied for automotive, motorcycle, and aircraft engines.

Modern passenger cars generally adopt the wet oil sump design. More specifically, the crankcase sump (often referred to as the oil pan) also functions as an oil reservoir. The oil pump is placed at the bottom of the crankcase as well. The returned oil after the engine oil circuit is accumulated at the oil sump and delivered to the user components again. The Fig. 3.8 shows the oil circuit of a gasoline engine with the wet oil sump design. The oil pump sucks in oil from the oil pan and forces it through the heat exchanger, filter, and finally into the engine oil circuit. The delivered oil flow splits into the passages to the camshaft bearing and the main oil gallery to the crankshaft bearing. The gallery is a term used by the automotive industry to describe a narrow oil passage. The oil in the main oil gallery will flow along a thinner oil passage into the clearance between the main journal and the bearing shell. This clearance is able to store oil to lubricate the main bearings temporarily.

However, the oil inside the thinner passage does not directly lubricate the conrod bearings, which locates between the connecting rod and the conrod journal. It has to flow through a passage inside the crankshaft from the main bearing clearance to reach the conrod bearing. The details of the crankshaft passage are included in the following sub-section. There are also components like the pressure relief valve and oil level indicator to ensure the proper flow inside the circuit. After the delivery oil exits the bearings, it drips back to the oil sump due to gravity and accumulates for the next oil flow cycle.

This design is sufficient for most passenger vehicles' daily driving conditions, and it is also easier and economical to manufacture compared to the dry sump system. Therefore, this design is prevailing in the automotive industry for mass production passenger vehicles, and its details are included in this thesis.

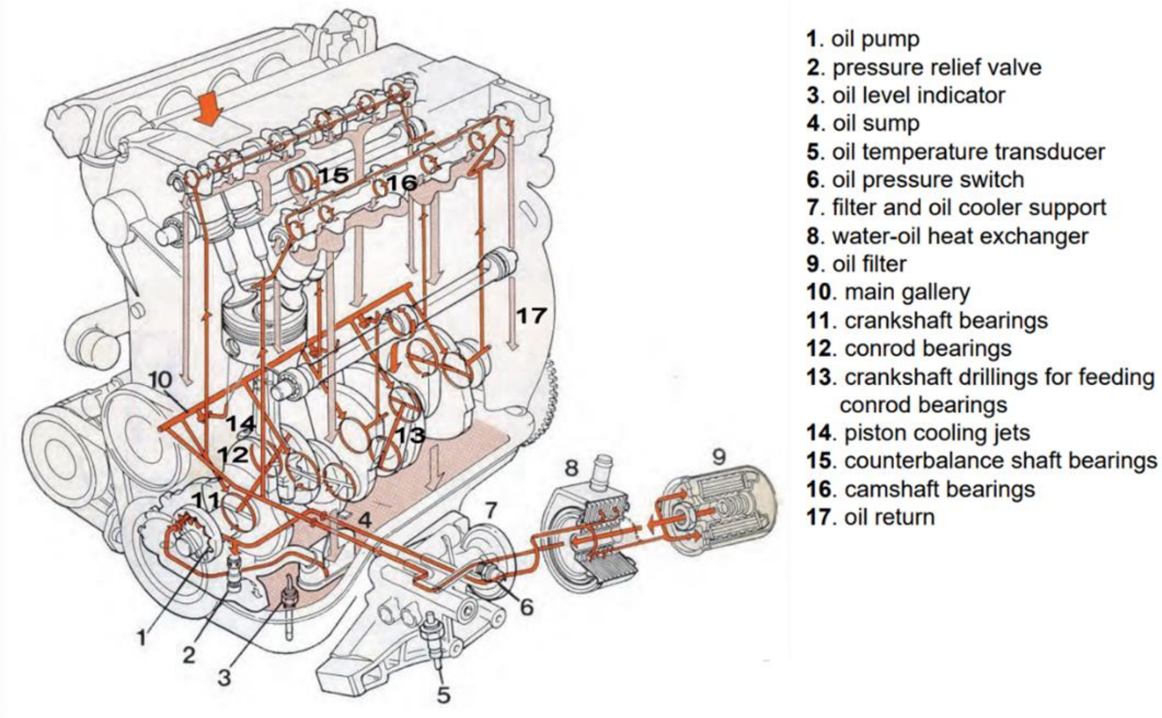

Fig. 3.8 Wet sump oil circuit of a passenger vehicle gasoline engine [12]

As an alternative to the wet sump design, the dry sump does not utilize the crankcase sump as an oil reservoir. The sump is relatively thin and shallow; therefore, the return oil is gathered by scavenge pumps and stored in a separated oil reservoir. There is not as much oil as the wet sump system in the sump, so it is called the “dry sump” system.

Compared to the wet sump pump, the dry sump system has less oil contamination and oil starvation. It is because the oil is in a separate tall reservoir. The piston also has less windage from the oil mist since the scavenge pump removes the oil below. [12] The thin crankcase sump also lowers the engine center of gravity. Unfortunately, the wet sump system is too expensive and complicated to manufacture and maintain, so it is mainly used in the racing car or high-performance vehicles rather than mass production vehicles.

3.4.1 Oil path inside crankshaft: the drills

The internal oil passages inside the crankshaft allow oil to flow from the main journal bearings to conrod bearings. The bearings and journals are designed to have some clearance in between so that the oil can flow through and provide necessary cooling and lubrication. The Fig. 3.9 shows a four-cylinder engine crankshaft and the oil passages inside it. There are drilling holes through the crankshaft that connect either two sides of the main bearing journal or connect the main journal and conrod journal. These oil passages ensure the oil flow from the oil gallery to the main bearing and then to the conrod bearing.

With the proper pressure and oil flow from the pump, the oil from the engine oil gallery firstly reaches the main bearing journal. Since the oil can only enter the main bearing from the oil gallery side, the other side far from the gallery could experience oil starvation. With the drilling through the main journal, the oil in the clearance can easily reach the side that does not directly contact the oil gallery. Since the conrod journal is constantly rotating about the shaft center, there is no constant contact between the conrod journal and the engine block. Consequently, it is not possible to directly supply oil to it from the main oil gallery. As a solution, the manufacturer drills a hole across the crank to allow the oil flowing from the main journal out to the conrod journal. These drills provide the necessary oil flow to the conrod bearing installed on the conrod journal.

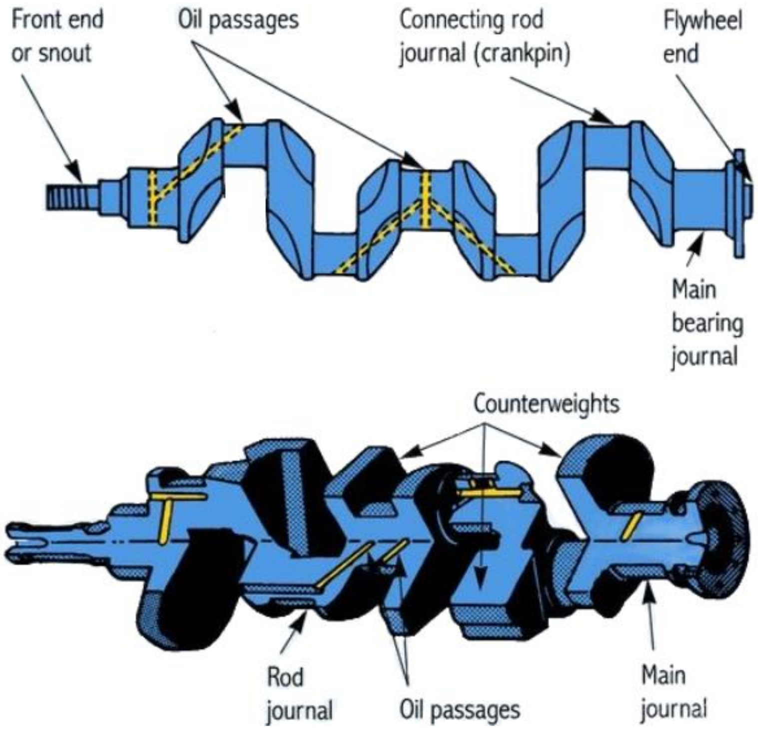

Fig. 3.9 Crank shaft oil passages [13]

In specific engine designs, an internal drill exists in the connecting rod, so oil from the conrod bearings can be supplied to the wrist pin for extra lubrication and cooling. The oil flow inside the connecting rod is also considered as a part of the oil circuit.

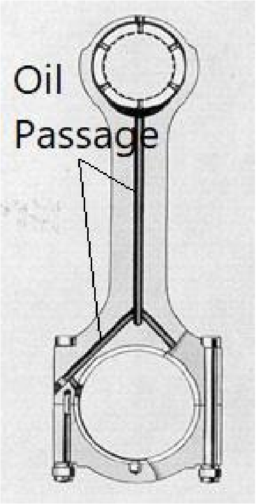

Fig. 3.10 Oil passages inside the connecting rods for piston pin lubrication [14]

3.4.2 Engine bearing constructions

There are mainly three types of engine bearings: crankshaft main bearing, connecting rod bearing (also called conrod bearing), and camshaft bearing. Unlike the conventional ball bearings, the main bearing and conrod bearing are made of two curved metal shells installed on the engine block. They must be two separate pieces for later assembly of the crankshaft. As the Fig. 3.11 shows, the two pieces of bearing shells are designed to fit into the engine block or connecting rod and form a cylindrical shape. The inner diameter of the shells is slightly larger than the crankshaft journal so that engine oil can fill the clearance and the crankshaft can rotate freely. On the contrary, the camshaft bearing is a one-piece metal sleeve that slides into the installation position.

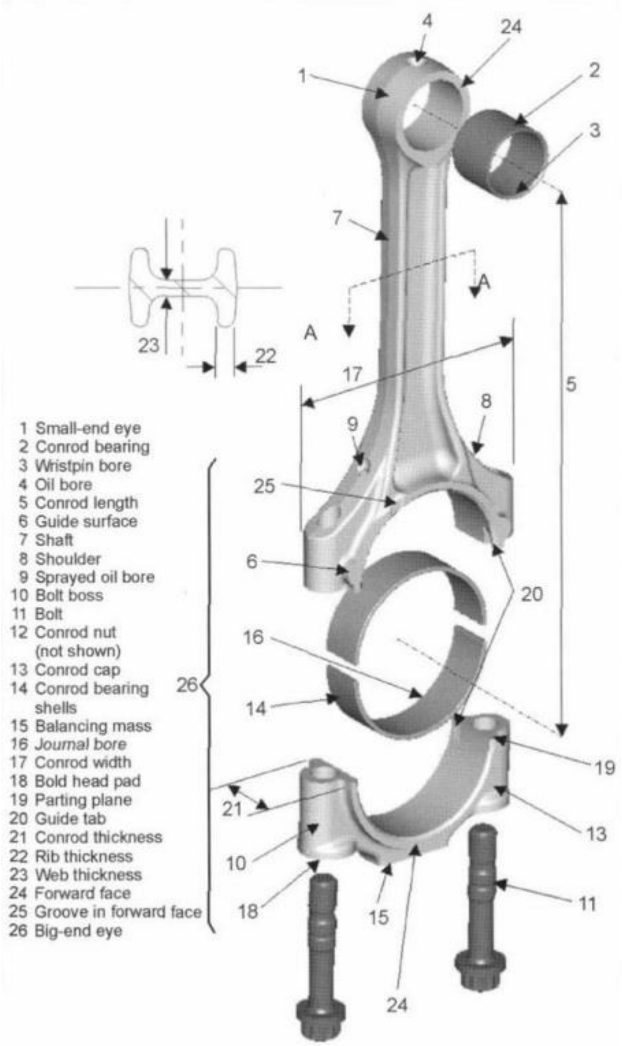

Fig. 3.11 Geometry and designations for a connecting rod with connecting bearing [15]

3.4.3 Bearing feeding: holes and grooves

The supplied oil from the main oil gallery first enters the main journal's clearance from the top area. Meanwhile, the crankshaft sinks slightly to create a larger clearance on the top and a smaller clearance at the bottom. As the bottom half of the bearing bears more load and any openings will interrupt the load distribution, the feeding hole and groove must be placed in the top of the bearing. The Fig. 3.12 shows the three types of feeding: with a feeding hole or circumferential groove.

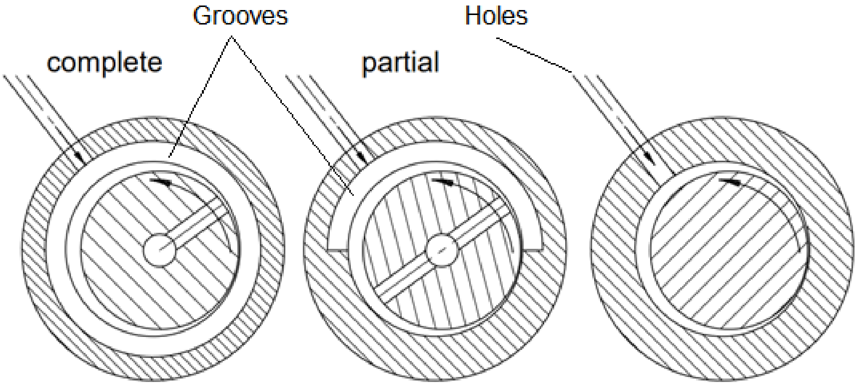

Fig. 3.12 Journal bearings feeding [12]

It is essential to ensure continuous oil flow around the bearing to compensate for the flow leaks from the sides. The continuous flow also provides necessary cooling because the temperature significantly influences the viscosity and the load capacity. The Fig. 3.12 demonstrates three types of journal bearing feeding, including feeding hole, partial circumferential groove, and complete circumferential groove. The eccentricity between the journal and bearing is due to operation load, and the clearance is necessary for oil flow. As the schematic shows, the feed hole provides the necessary passage for the oil to enter the clearance between the engine bearings and the journal. Furthermore, the grooves ensure a sufficient clearance for the oil to spread around the bearing better. The groove is not necessary for every engine design, and its geometry depends on engine load and user components' needs. It is mostly included in the bearing design when the conrod bearing from downstream requires more oil flow.

3.4.4 Cavitation in the passages

The drilling inside the crankshaft provides better oil flow around the bearing and also increases the ability to develop oil cavitation. The demonstrates the cross-section view of a crankshaft. The crankshaft journal is shown in the middle, and the cross-drill is shown as the shadow area. As the oil flows from the main journal to the conrod journal, it enters the cross-drill passages at point 1, and then leaves the exit point 3 to feed the conrod bearing. Point 2 is the closest point on the cross-drill to the rotation center of the crankshaft. From point 1 to point 2, the oil moves following the centrifugal force direction because the cross-drill is rotating and the radius to the rotation center decreases. From point 2 to point 3, the oil moves against the centrifugal force while the radius increase. In conclusion, from the oil inlet to the conrod bearing oil supple hole (delivering oil from the upstream), the radius of a moving point along the cross-drill will first decrease and then increase, and so will the centrifugal pressure. Consequently, point 2 has the lowest pressure along the passage. The figure on the right shows the pressure inside the passage versus the distance. Relative equations to calculate the pressure distribution are included in the Appendix A. If the local pressure near point 2 is less than atmospheric pressure, the small nuclei or dissolved air will release into the oil and develop into cavitation. This could happen when sufficient supply pressure at the oil inlet 1 is not met, or the engine is operated under extreme conditions.

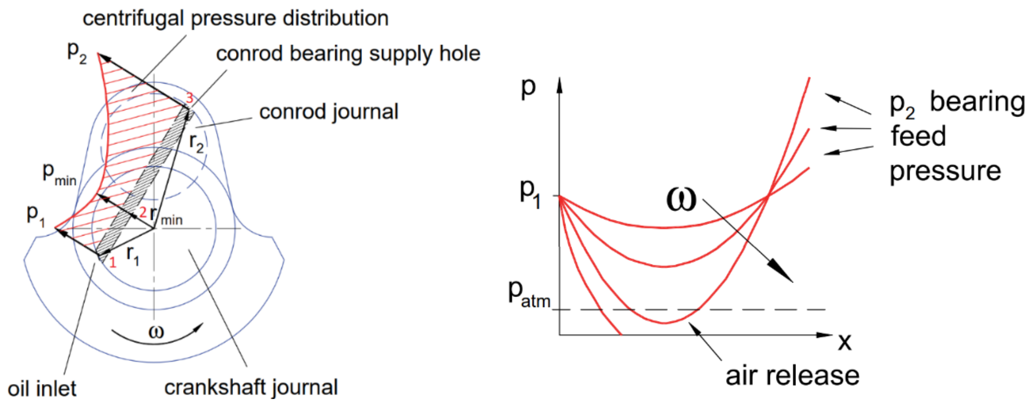

Fig. 3.13 Centrifugal pressure distribution along the cross-drill passage [12]

3.5 Numerical Simulation

The cavitation phenomenon involves formation of the vapor bubbles in liquid phase and Singhal et al. [5] proposed a cavitation model in which cavitation mass transfer between liquid and vapor phase is formulated using Rayleigh-Plesset equation. This cavitation model considers the effects of bubbles formation, pressure and velocity variations, and the incompressibility of the dissolved gases. It assumes that in the working fluid, the non-condensable gas (NCG) in the liquid is non-dissolvable gas (free gas) bubbles following the ideal gas law. In this model, all the non-condensable gas can freely expand with the decrease of pressure in cavitating zones. The mass fraction of non-condensable gases is pre-described and remains the same in a cavitating flow. This model was applied to pumps by Athavale et al. [16] and the results showed cavitation zones on the suction side of the pumps. The Singhal model was implemented by Ding et al. [6] who developed a novel CFD tool called PumpLinx® (by Simerics Inc) specialized for pump cavitation simulations, where this cavitation model is referred as constant gas mass fraction model. The tool PumpLinx is later integrated into Simerics MP+ which provides capability for multi-purposes and multi-phases simulation. The 3D transient simulation of an axial flow water pump was chosen [6] as a test case to demonstrate and validate the code capability. Frosina et al. [11] demonstrated Simerics' capability to simulate sliding vane pump's performance and validated the software package with experimental data. This thesis further explores the potential of CFD simulation on the pivoting VDVP and its response to cavitation.

CHAPTER 4 Numerical models

This chapter consists of two parts: the 3D simulation and 1D simulation set-up. The first part discussed the problem overview, defining fluid domain and grid, setting up physic and boundary conditions, and setting up the simulation parameters for the pump and bearings models respectively. The 3D solver and governing equations are also discussed. The first part also includes the grid and time step independence test of the 3D models. The second part included the modelling procedures of the 1D simulation.

4.1 3D Simulation

This section describes the numerical modal setup for both the 3D VDVP and bearing models. The performance of the pump and bearing are recorded under steady-state operation. The steady state is determined as the average value of flow and turbulence parameters, including the outlet flow rate, velocity, and pressure, maintained constant over a cycle in which the pump or bearing rotates.

4.1.1 Overview

4.1.1.1 Variable displacement vane pump (VDVP)

The variable displacement vane pump model consists of the inlet, outlet, spring chamber and pump chambers (or simply chambers), as shown in Fig. 4.1. The oil enters the pump at 1.01 x 10^5 Pa and exits with 6 to 7 x 10^5 Pa. The outlet pressure is based on the pump angular speed and oil temperature. The figure below shows the mesh of the 3D VDVP pump simulation for discussion. The grid details are in the section below.

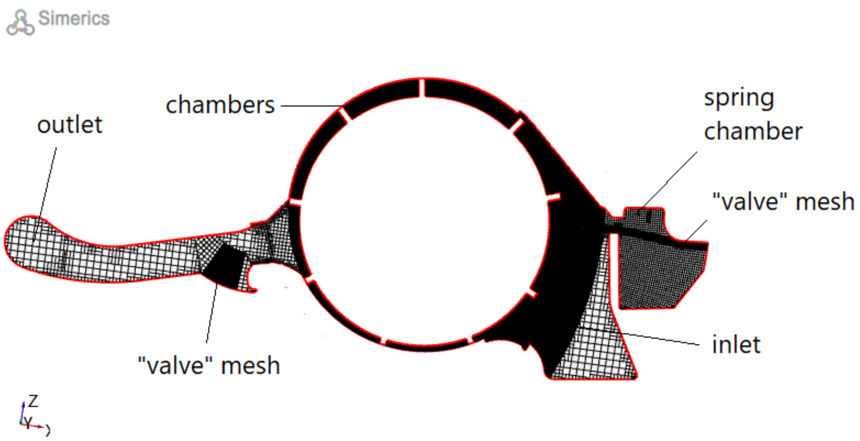

Fig. 4.1 VDVP fluid domains

4.1.1.2 Bearings and bearing deformation

The inlet pressure is 4.86×10^5 Pa, and the outlet pressure is 1.01×10^5 Pa. The inlet oil contains 6% of gas in volume, and the gravity acceleration 9.81 m/s^2 is included in the bearing model. In addition, the bearings are installed on a four strokes engine rotating at 4000 rpm. This thesis defines the modified bearing distortion data to characterize the clearance deformation. The bearing clearance shape varies over the four strokes, so the cavitation over two cycles or total of 720° is collected from the simulation. The flow rate from the side of bearings and the flow split between the conrod and main bearings are collected as simulation results.

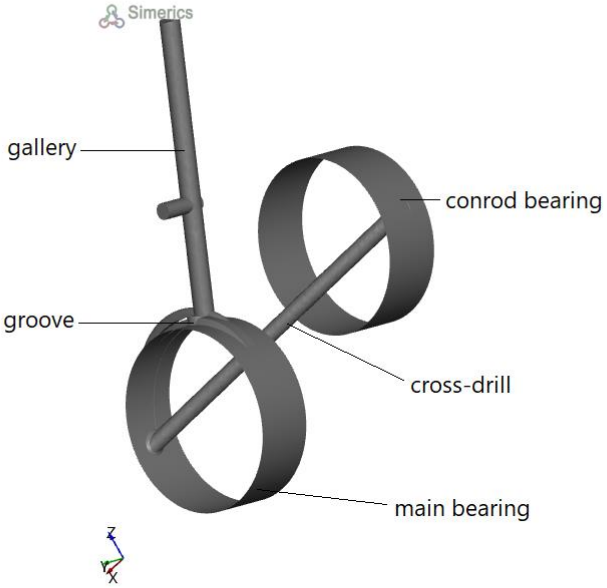

Fig. 4.2 Bearing overview

The main bearings and connecting rod (conrod) bearings are deformed during engine operation. The engine load presses the bearing sleeve along the line of the piston stroke. The distorted sleeve is often referred to as the “lemon shape”. Since the bearing sleeves are deformed, the oil in the clearance is also in lemon shape. The main bearing and conrod bearings clearance distortion are shown in the figures below. The distortion magnitude of the bearing shell is exaggerated for visualization. The fluid domain discussed in section 5.2 are the fluid inside the clearance between the bearing shells and crankshaft.

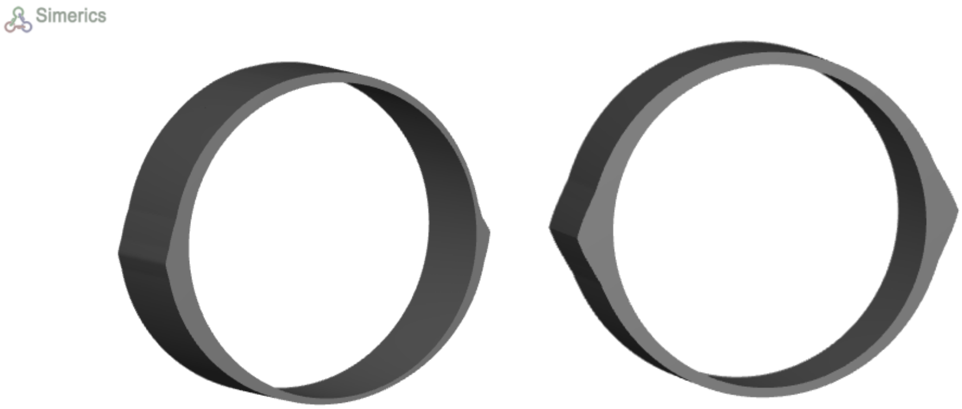

Fig. 4.2.1 Bearing “lemon shape” distortion

4.1.2 Fluid domains and grid

The pump geometry is provided by the manufacturer SLPT. The fluid domain inside the pump is extracted and trimmed with GT-SpaceClaim® 2016. Then the CAD file of the fluid domain is imported into the 3D CFD software Simerics MP+®; The fluid domains are defined in Simerics based on their functions: i.e., inlet, chambers, and outlet; Simerics has the built-in mesh generator for the chambers, by which the user defines the vane tip gap and numbers of chambers. When the eccentricity ring rotates, the fluid domains next to the eccentricity ring will slightly expand or contract. The variable volumes are discretized with the built-in “valve” mesh. The inlet and outlet are generated with the binary tree mesh. Generally, the hexahedral grids are generated inside the fluid domain. The adjacent meshes are connected by the interfaces where the miss-matched grids from gap or overlap are adjusted.

The bearing geometry is also provided by the OEM. The preparation of the CAD file is the same as the pump model. The fluid domain is discretized with the hexahedral grid, too.

4.1.3 Physic and conditions

The physical conditions are defined after the meshes are built. Five models including model for vane, valve, cavitation, turbulence, and rotation are coupled to complete the simulation. The vane model defines the pump chambers, their configuration and rotational velocity. The valve model couples with the rotational model to characterize the eccentricity ring rotation and deformation of nearby fluid volumes. Singhal's gas constant gas mass fraction [5] is adopted to describe the cavitation development inside the pump. The initial gas mass fraction is set to 9×10^{-5}, and the influence of various gas contents on the cavitation is examined in section 5.1.6; The standard k - ε model is adopted for modeling the turbulence. The rotating fluid domains including the bearings and cross-drill are defined with the rotation model, which characterizes the rotation speed and direction. The pump operates with SAE 0W-20 oil, whose density and viscosity are temperature dependent.

The rotation entities in the models are the pump chambers and bearings. According to the equation $Re = \frac{\Omega \cdot r^2}{v}$ (where Ω is the rotational speed in rad/s, r is the radius in meter, and v is the fluid kinetic viscosity). The Reynolds number of the pump rotating with 5000 rpm and 100°C is 1×10^5, and the Reynolds number of the bearings operating at 4000 rpm and 100°C is 3.5×10^4. Therefore, the flow inside the rotating entities is considered turbulent. Both pump and bearing models adopt the standard k - ε model, with constants C_μ, = 0.09, C_1, = 1.44 and C_2 = 1.92. The turbulent Prandtl numbers of turbulence kinetic energy and dissipate rate are 1 and 1.3, respectively. Different turbulent Prandtl numbers have been examined with no significant impact on the pump's effective flow rate and cavitation development. Near the walls, the y^+ value is not checked, and the boundary layers are not resolved due to the complexity of the geometry and grid requirements.

The inlet boundary condition for the pump model is specified as pressure inlet with 1.01×10^5 Pa and infinity flow normal to the inlet port. The outlet boundary is a specific pressure outlet whose value depends on the design specification.

For bearing simulations, the inlet pressure is set as specific pressure inlet 4.86×10^5 Pa, which is the same as the target oil gallery pressure. The outlet is the two sides of bearings with the pressure of 1.01×10^5 Pa.

4.1.4 Equations and solver

In Simerics Inc, hydrodynamic governing equations for continuity, momentum equation for vapor-liquid mixture considered homogeneous and incompressible and the volume fraction equation for the liquid phase are solved. The summation of the vapor non-Condensable Gas (NCG)volume fraction α = (volume of the vapor/ total volume) and the liquid volume fraction γ = (volume of liquid/total volume) is equal to unity. The transition from one phase to another is ensured by the inter-phase transfer via source terms in the transport equation. This method has the advantage to take into account the time dependence of mass transfer phenomena by empirical laws in the source terms. To model the cavitating turbulent flow, the source term in the transport equation considers the interfacial velocity of bubble at collapse. It is based on the Rayleigh–Plesset equation, which emphasizes the fundamental bubble dynamics.

The turbulence is modelled with two-equations standard k-epsilon model and the Simerics Inc adopts Singhal's constant gas mass fraction model as the cavitation model. Non-Condensable Gas (NCG) is any gas in the liquid that is different from the liquid's vapor. As such, it can dissolve or be released but is not generated or absorbed from the fluid. In the pump and bearing model, NCG is the air inside the motor oil; The mixture density is computed based on the gas molecular weight, the local pressure, and temperature, according to the ideal gas law. The details of the cavitation model are included in Appendix B. Gravity is not considered in the pump simulation, but it is included in the bearing simulation with $g=9.81 m/s^2$ pointing to negative z direction.

The governing equations are solved by the Finite Volume discretization method with the SIMPLE algorithm for the velocity-pressure coupling. The second-order upwind scheme was used for solving the velocity and upwind scheme is used for the pressure.

The variables monitored for convergence are flow (velocity and pressure), turbulence (turbulent kinetic energy and the turbulent energy dissipation rate), and cavitation (gas volume fraction, vapor volume fraction, and dissolved gas volume fraction). The simulation is considered converged when these essential variables' residual drop below the tolerance. The residual represents the imbalance of conserved variables from the discretized equations at each cell. For the transient simulation, the default convergence criteria in Simerics is 0.1. However, for accuracy purposes, the pump simulation set the criteria as 0.001, 0.01, and 0.001 for the flow, turbulence, and cavitation, respectively. For bearings, the converge criteria for solving the flow, turbulence, and cavitation models are 0.001, equivalent to 10^{-3}.

4.1.5 Set-up the simulation

The variable displacement vane pump simulation runs for 20 revolutions per case. The number of iterations is 20. The number of time step is considered as 360 per revolution of the pump chambers or the main bearing. Thus, one time step is equivalent to one degree of rotation. Additionally, the corresponding real-time changes with different operating speeds. For example, when the pump operates under 5000rpm, one time step is equal to 3.33×10^{-5}s. In other words, the simulation time is 0.24s for 20 revolutions.

The simulation runs on two platforms: 1. The HP Zbook 15 G5 with intel® Core™ i7-8850H CPU@ 2.60GHz and 64-bit Windows 10 Enterprise. On the laptop, one case requires 12 cores CPU run for 21.4 hours. 2. The high-performance server with 32 cores, in which the same case runs for 8 hours for 20 revolutions.

The bearing simulation runs for eight revolutions per case. The time step is 3.33×10^{-5}s, equivalent to 1degree of the main bearing rotation. In addition, each time step is reached after 60 iterations to converge. The bearing simulations are performed on HP Zbook 15 G5, in which each case takes 10 hours.

4.1.6 Grid independence test

The numerical error occurs when the discretized model is used to calculate the continuous equations. In other words, the discretized error is because of the inappropriate grid or time step size. [17] More discretization will provide more accurate results but will also cost more CPU time. Therefore, the grid size and time step need to be appropriately selected for accurate results with acceptable simulation time. In this section, the grid independence test is conducted.

The bearing model is initially modeled with 193,042 cells. Then the fine and coarse meshes are applied on the same model as 289,282 and 154,655 cells.

With the three mesh sizes, two results analysis is conducted: Firstly, the average mass and volume flow rate of the outlet oil-gas mixture is compared. The errors of the refine and coarse meshes are less than 3% and 2%. This deviation is considered acceptable; Secondly, the time-average data on three points inside the fluid domain is compared. The figure below shows the bearing model and selected points. Point a is inside the oil gallery; point b is at the interface between groove and oil gallery; point c is at the one side of the groove. The velocity magnitude, radial and tangential velocity relative to the bearing rotation, and pressure are compared. The difference between the coarse mesh and the standard mesh are: ±12%, ±17%, ±19% and ±2%. The difference between the refined mesh and the standard mesh are: ±4.5, ±4.5%, ±1% and ±0.1%. The coarse mesh can predict the outlet flow rate with a small deviation, but it is insufficient to calculate the velocity inside the gallery and groove. Therefore, the standard and fine mesh settings are accepted.

In conclusion, the influence of the grid size variation on each fluid domain is examined. The differences are acceptable, and the grid size with 193042 cells is adopted for the bearing numerical modeling.

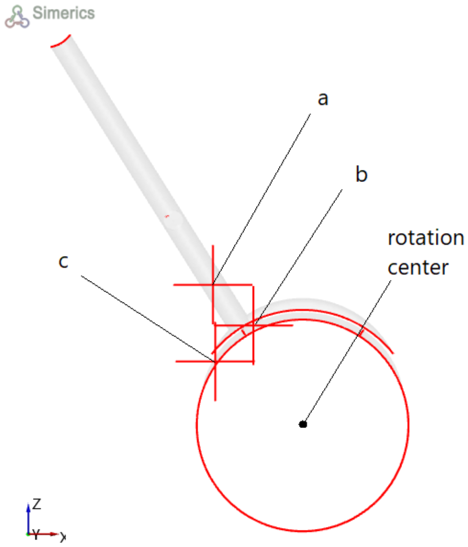

Fig. 4.3 The bearing fluid domain and locations of probe

4.1.7 Time step independence test

The original time step 3.33×10^{-5} equals one degree of main bearing rotation. Then, the time step is refined as 0.5 and 0.25 degrees of main bearing rotation. The simulation with the smaller time step takes approximately two times the previous set-up. Additionally, the time step test is conducted with the same grid size. The bearing outlet flow rate and the same points a, b, and c in the figure 4.3 are compared. The deviations of the outlet flow rate between different time step set-ups are less than ±2.5%. Similar to the grid test, the velocity magnitude, radial and tangential velocity relative to the bearing rotation, and pressure are compared. The difference between the refined time-step settings and the standard model are ±2, ±4%, 0.1%, and ±0.1%. Therefore, the simulation model is not influenced by the time step size.

4.2 1D simulation

This section is dedicated to the numerical modal set-up for the 1D VDVP and bearing model.

The 1D simulation software adopted in this thesis is GT-Suite. It is a simulation tool with capabilities and libraries for various automotive applications [18]. The software package includes the pump and bearings models, which include the corresponding fluid domain and control functions.

The 3D CAD file is imported into the GT as geometry information. The user needs to divide the fluid domain into sub-domains based on their function, similar to the 3D model preparation. Unlike the 3D package, the 1D software does not display the geometry in the user interface. It recognizes the volume and surface area, then stores the information under each subdomain's name. GT has the built-in VDVP and bearing models. The block charts of these models are shown as the figures. (The pump model inherits the inlet, outlet, and chambers volume from the 3D CAD file. The angular speed and eccentricity control data are entered as the manufacturer data; The bearing model inherits the oil galleries, groove, cross-drills, and bearings geometry from the CAD file. The angular speed is set as the OEM data as well) After the user classifies each domain into the corresponding function group in the block chart, the inlet and outlet environment is set the same as the boundary conditions in the 3D model.

The Fig. 4.4 shows the principle of the pump model. The inlet, chambers, and outlet domains are imported from the CAD file. As the GT pump template requires, the fluid volume inside the rotating chambers is split into individual volumes. The eccentricity control function can decide the pump geometry's eccentricity as described in the literature review. The angular speed of pump rotation is also a user input value. With the fluid domains and control functions set-up, the model can calculate the flow motions from the inlet environment to the inlet, chambers, outlet, and outlet environment; Fig. 4.5 shows the workflow of building the 1D bearing model. The geometry of the simplified oil circuit (oil galleries and bearing geometry) is also imported from the CAD drawing. Under different angular speeds, the bearing geometry will vary. Specifically, the distortion data provided by the OEM varies under different angular speeds. After the user defines these data and rpm, the model can calculate the flow from the oil gallery to the bearing volumes.

Cho et al. [19] and Buono et al. [20] validated and implemented the GT 1D model with measured pump data. Additionally, Krishnah [7] correlated the 1D bearing model with the results from other 1D simulation tool MIT psim. In this thesis, the GT 1D models for the pump and bearing were developed. The pump model is corelated with the results obtained

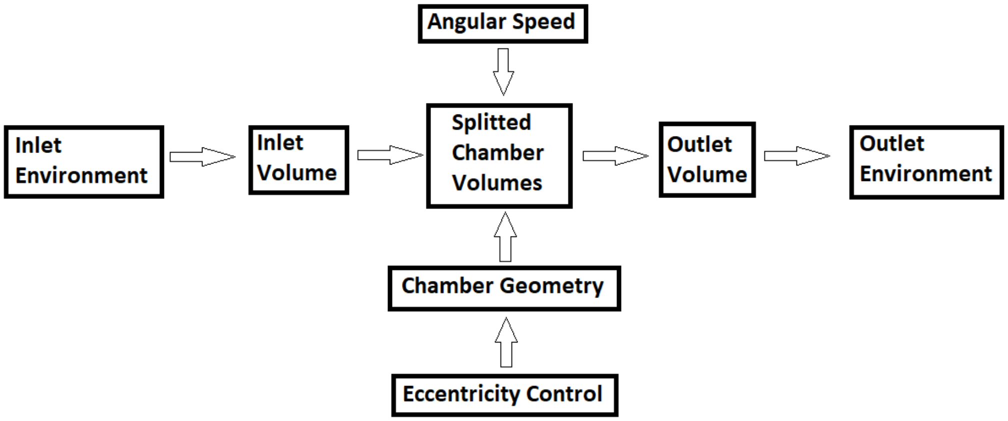

Fig. 4.4 Block chart of GT-Suite pump model

from the 3D CFD software and experimental data provided by the supplier. Due to the unavailability of the experimental data, the bearing model is investigated in terms of bearing flow rate and flow split.

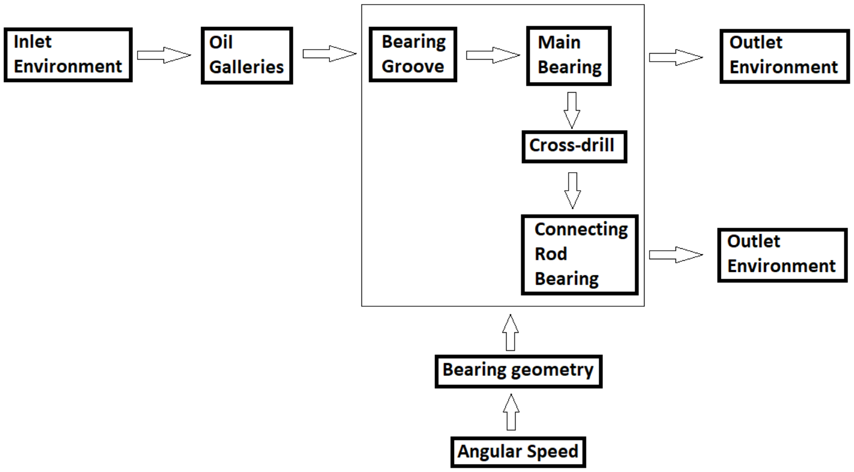

Fig. 4.5 Block chart of GT-Suite bearing model

CHAPTER 5 Results and discussion

The results section begins with analyzing the instantaneous pressure and velocity fields inside the 3D CFD pump model. The numerical models and experimental data are compared for two oil temperatures: 100°C and 50°C, respectively. Furthermore, the 3D CFD and 1D simulation models under variable operating conditions are discussed. The onset of cavitation for different inlet initial gas contents, and the corresponding resulting gas fraction in the chambers are also investigated. Then the three cam-ring designs with different cross-sections are examined. The flow visualization inside the chambers is presented to study the cavitation. The second part of Chapter 5 presents visualization of cavitation in the thin film bearings. The 3D CFD and 1D simulation results of flow rate and flow split are also discussed.

5.1 Variable displacement vane pump (VDVP)

This section is dedicated to the simulation results from both the 3D and 1D VDVP models.

5.1.1 Instantaneous Pressure Contour at the 20th revolution

A cross-section at Y = - 0.408m from the origin point is used to demonstrate the pressure contour inside the VDVP. As shown in Fig 5.1, the origin point is at the center of the outlet port, and the cross-section is located 0.408m below. Additionally, the figure shows the side of the VDVP from the perspective parallel to the Z axis. The cross-section Y=-0.408 is perpendicular to the Y axis and extends toward and outward the paper. This cross-section location is selected because it intersects all the fluid domains inside the pump. Thus, all the contours in this section are plotted on this cross-section. The contours are plotted at the 7608th time step, when the pump is operating steadily at the 20th revolution. The operation conditions of the pump are at 5000 rpm and 100°C and 50°C. The post-processing adopts the absolute pressure in Pa. The primary fluid domains shown in Figs. 5.2 and 5.3 are outlet, rotating chambers (or simply chambers), inlet and spring chamber. The range of absolute pressure in this cross-section varies from 501 to 9.14×10^5 Pa.

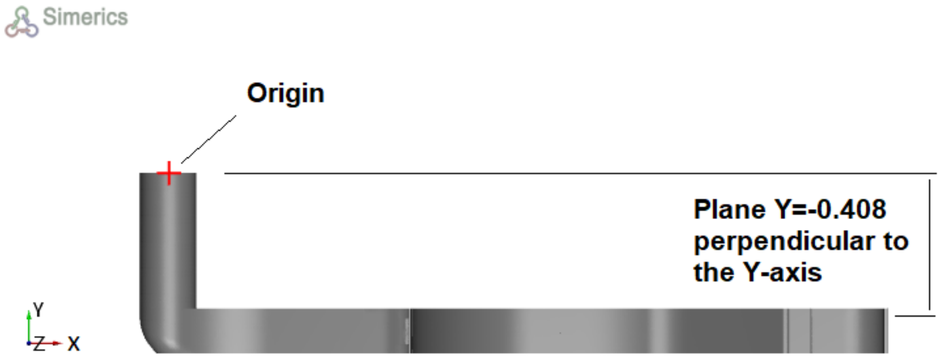

Fig 5.1 Sideview of the origin, VDVP and cross-section Y=-0.408m

The low-pressure area covers the spring chamber, inlet and the chambers closed to the inlet. As discussed in section 3.3.1, the eccentricity and rotation of the pump will generate a low-pressure zone in the chambers and the inlet domain. The local pressure could be even lower than the atmospheric pressure. Since the solubility of the gas in the fluid is proportional to the fluid pressure [8] The decrease of the local fluid pressure increases the possibility of the formation and growth of gas bubbles. As section 5.1.3 shows, the gaseous cavitation mainly occurs in the low-pressure zones. However, the vapor cavitation only occurs when the local pressure is lower than the oil vapor pressure (Pv). The absolute Pv for SAE 0W-20 oil at 50°C and 100°C are 0.0188 and 0.0415 Pa. [21] Thus, the vapor cavitation rarely occurs in the pump unless the local pressure is extremely low, or certain components are over-heated. The Figs. 5.2 and 5.3 show the instantaneous absolute pressure distribution in the VDVP after 20 revolutions operating at the angular speed of 5000 rpm and different temperatures of 50°C and 100°C, respectively.

The highest local pressure inside the model is as much as 9 MPa which is typical for the vane pumps used for automotive applications. The high pressure occurs in the outlet port and chambers near the outlet. As discussed in the literature review, cavities formed in the suction port could burst under this pressure.

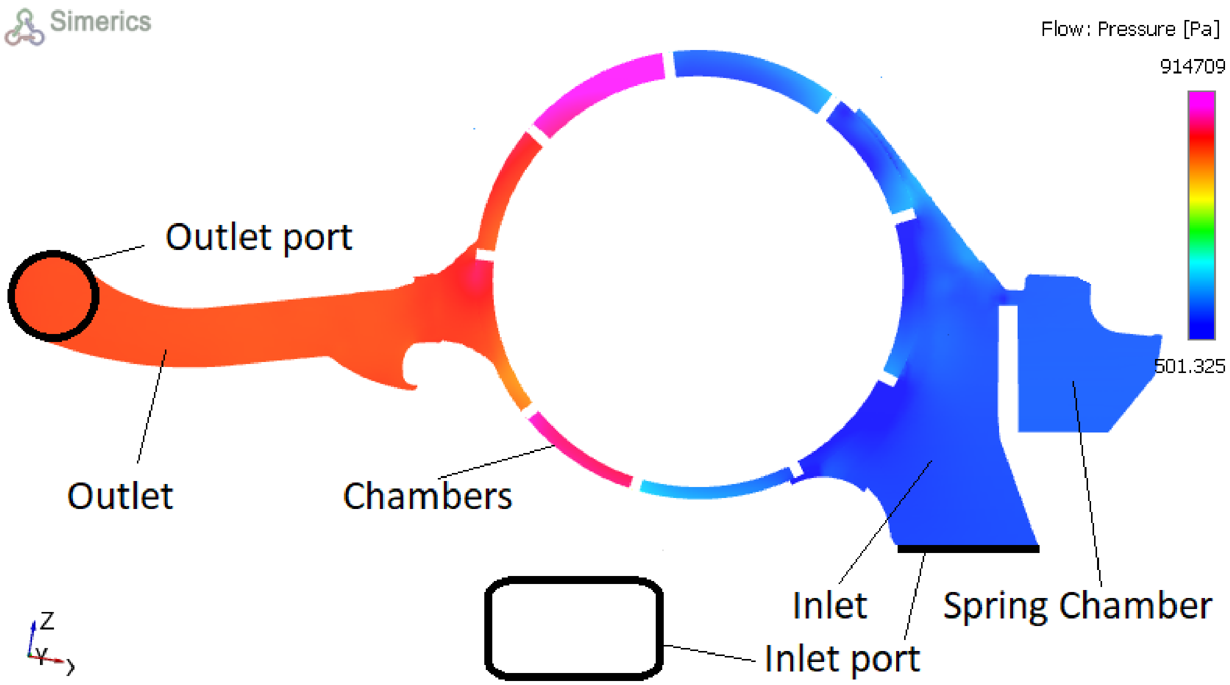

Fig. 5.1 Instantaneous pressure contour of VDVP at 5000 rpm and 100°C. Note the inlet port area is 4.13cm^2, and outlet port area is 2cm^2.

The 100°C and 50°C have the highest pressure occurring on the chambers near the outlet. Compared to the 100°C case, the 50°C degrees case has less outlet pressure simply because the boundary condition on the outlet port is less. Near the inlet side, both cases have the local pressure less than the atmosphere on the trailing side of the vanes (the pump operates counterclockwise). The local low pressure near the vane will introduce cavitation. The relative discussion is included with the cavitation contours in section 5.1.3.

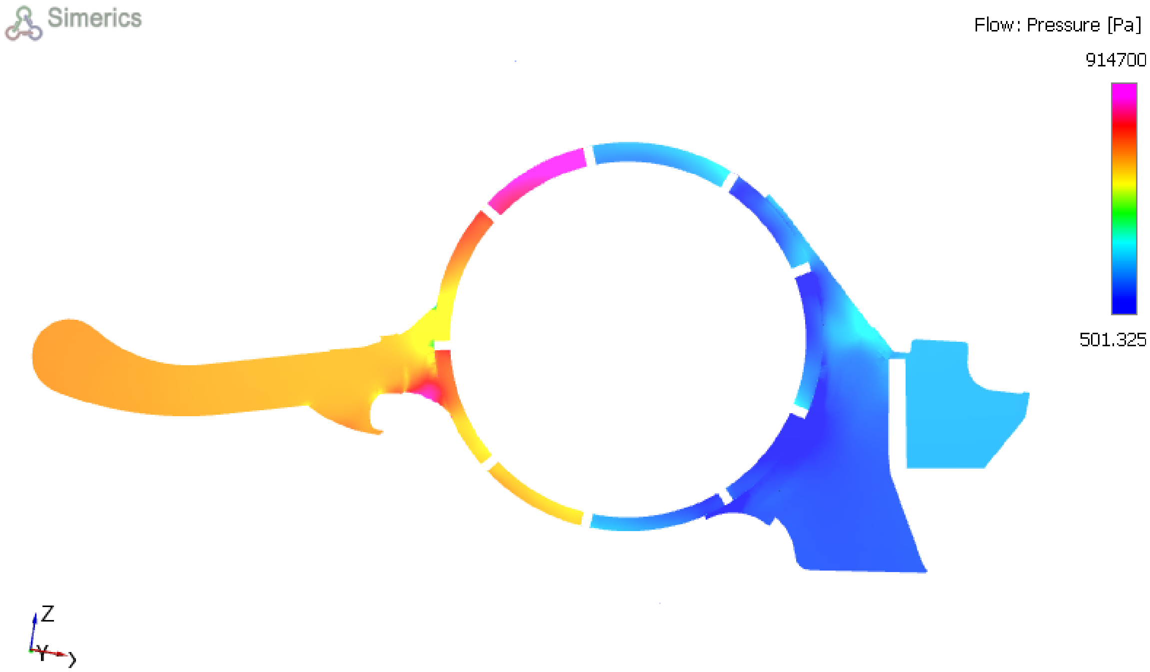

Fig. 5.2 Instantaneous pressure contour of VDVP at 5000rpm and 50°C

5.1.2 Instantaneous Velocity Contour at the 20th revolution

The instantaneous velocity contours are plotted on the same cross-section as the pressure contour, which intercept with main fluid domains. Fig. 5.3 shows the velocity magnitude of the oil inside the pump. The highest velocity magnitude occurs in the chambers, and the relatively lower velocity magnitude is obtained in the inlet and outlet areas.

Generally, the oil in the spring chamber, inlet port, and outlet port has relatively low velocity because of their large volume. Compared to the outlet, the inlet has a relatively lower velocity magnitude than the outlet area because of its larger throttling area shown in Fig. 5.1. Specifically, the inlet port size is 4.13cm^2, and the outlet port area is 2cm^2. Thus, the inlet would have a smaller velocity magnitude in general. Additionally, the outlet is closer to the delivery side, so the fluid velocity magnitude is higher than the inlet area. The spring chamber is a dead volume and only provides room for the cam-ring return spring.

This spring chamber design is not entirely sealed, so there is only a small fluid motion in this dead volume.

Generally, the oil in the spring chamber, inlet port, and outlet port has relatively low velocity because of their large volume. The spring chamber is a dead volume and only provides room for the cam-ring return spring. This spring chamber design is almost entirely sealed, so the fluid is nearly stagnant in this dead volume. On the contrary, the largest velocity magnitude occurs in the rotating chambers. The rotation motion from the drive shaft keeps the chambering rotating at high speed. The fluid between the chambers and the inlet or outlet also has high velocity because the fluid near the chambers is about to be sucked in or expelled. The local high velocity will lead to low pressure, which favors cavitation development. The cavitation contours in the section 5.1.3 reveal cavitation locates in the high-velocity areas.

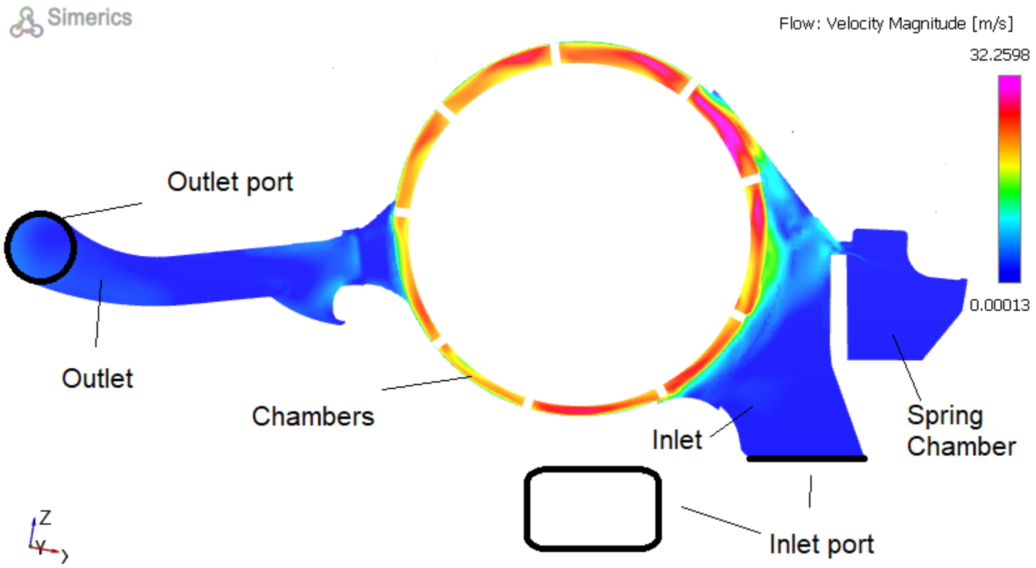

Fig. 5.3 Velocity magnitude contour of VDVP at 5000rpm and 100°C in steady state

Figure below is the velocity vector plot on the same cross-section Y=-0.408. The velocity vector plot reveals the intensity and direction of velocity vector distribution. Each vector is plotted based on one cell. So, the vector density is dependent on the mesh, and the vector length is determined by the velocity magnitude. Figures 5.5a, 5.5b, 5.5d, 5.5e, and 5.5f are the magnified view of the projected velocity vector. The figure 5.5c is the detail view of the local vectors in figure 5.5b, which shows the velocity direction when the chambers are about to detach from the inlet.

The path of the oil inside the pump is: entering by the inlet port, passing the inlet and spring chamber, entering the rotating chambers from the inlet side, being carried by the chambers to the outlet side, then leaving the chambers and flowing out through the outlet. As stated in section 3.3.1, the eccentricity is the essential reason of the suction and delivery power. There is a small stream inside the dead volume (spring chamber) because it is not completely isolated from the inlet. This flow is so small that it does not make a significant impact. The vectors in the inlet and outlet are generally less dense. Due to the rotation motion, the longest vector arrows exist on the chambers and nearby fluid domains.

In the chambers, the mesh size is consistent and does not deform when the eccentricity changes. However, the vector shown in figure 5.5e is not uniform: when the rotating motion of the vane pushes the fluid forward, the flow inside the chambers is tumbling while moving forward. The evidence is the contours of Vy (velocity pointing inward and outward of the paper) in Fig. 6.5 and Fig. 6.6 show the Vy in the chamber varies from -8 to 8 m/s. It means the flows in two opposite directions exist simultaneously within one chamber. Hence, the tumbling flow causes the vector distribution in figure e.

As the chambers rotate counterclockwise, they approach and detach the inlet at points a and b. At point a, point b, and the vane tip, the velocity vectors abruptly change their direction and magnitude (figures 5.5a, 5.5b, 5.5c, and 5.5d), because of the sudden change in local geometry. It explains the cause of local low pressure and induced gaseous cavitation. In addition, the vector size is twice the unit vector because this size is appropriate to visualize the vector distribution. The vector starting from the cells on the chamber surface will end outside of the initial cells; Therefore, in Figures 5.5a and 5.5b, there is no vector on the void between the chambers, where the solid vanes exist. When the delivered flow exits chambers, there are swirls inside the outlet passage shown in figure 5.5f. As the flow moves downstream, the velocity vectors tend to be uniform in length and point to the outlet port. The local vector distribution in the figures 5.5 a-f is rather disorder, which favors the cavitation development discussed in section 5.1.3.

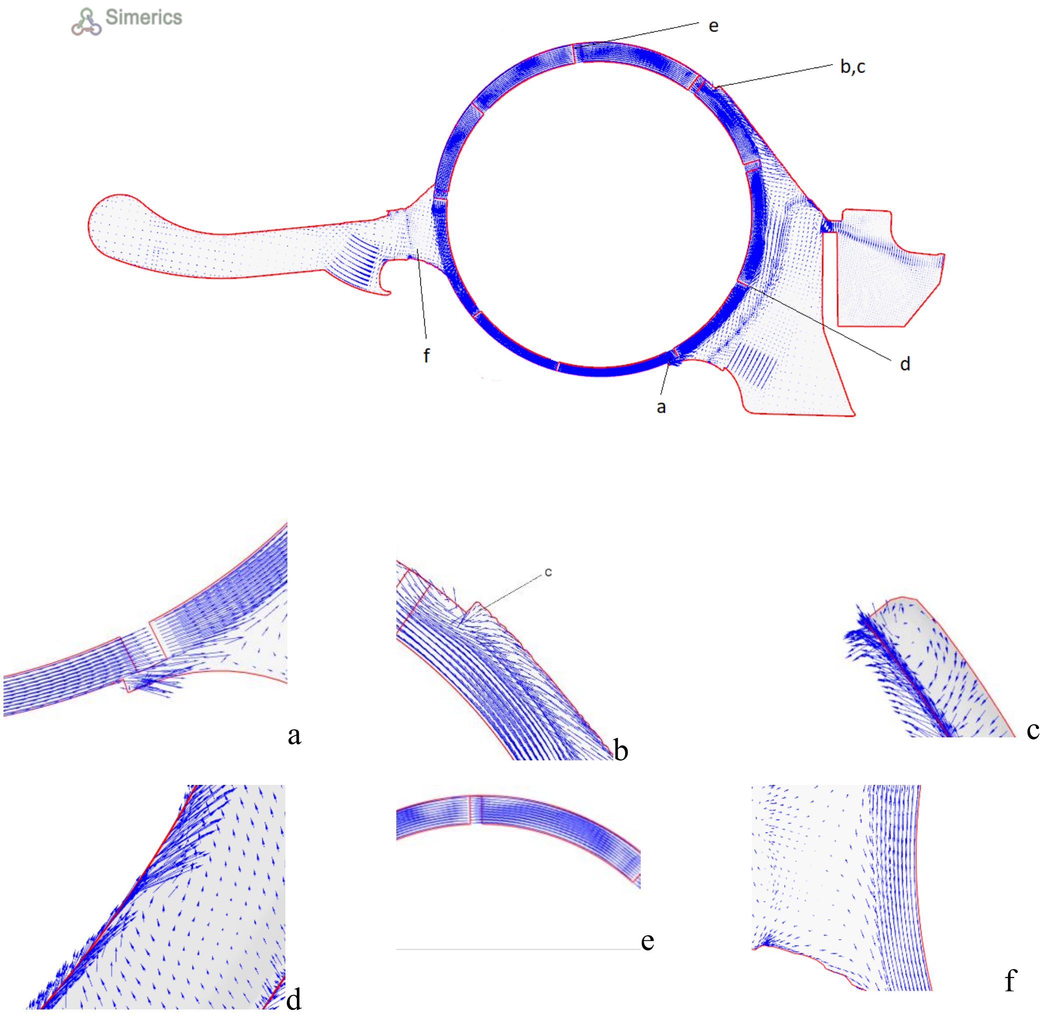

Fig. 5.4 Instantaneous velocity vectors of VDVP at 5000rpm and 100°C at the 20th revolution

Fig. 5.5 shows the velocity contour at 50°C. The high velocity region is the rotating chambers and nearby fluid domains. The highest velocity also exists in the chambers and nearby fluid. However, the inlet, especially the area close to the chamber, has higher velocity than the 100°C case. As higher velocity leads to lower pressure, the lower temperature is expected to have more cavitation. This is also shows in the 5.1.3. Separated velocity contours on the same cross-section Y= -0.408 in X, Y, and Z directions are included in the Appendix C.

The velocity vector plot at 50ºC is included in the appendix. The vector size is not the same as the 100ºC case, which has vector arrows on the void between the chambers where the solid vanes exist. The 50ºC case clearly shows the vectors do not exist in the void. However, it shows the same trend as the 100ºC case near the outlet, inlet, and chambers: The largest vectors exist in the chambers, and the vector distribution is chaotic near the potential cavitation areas in figure 5.5 a-f.

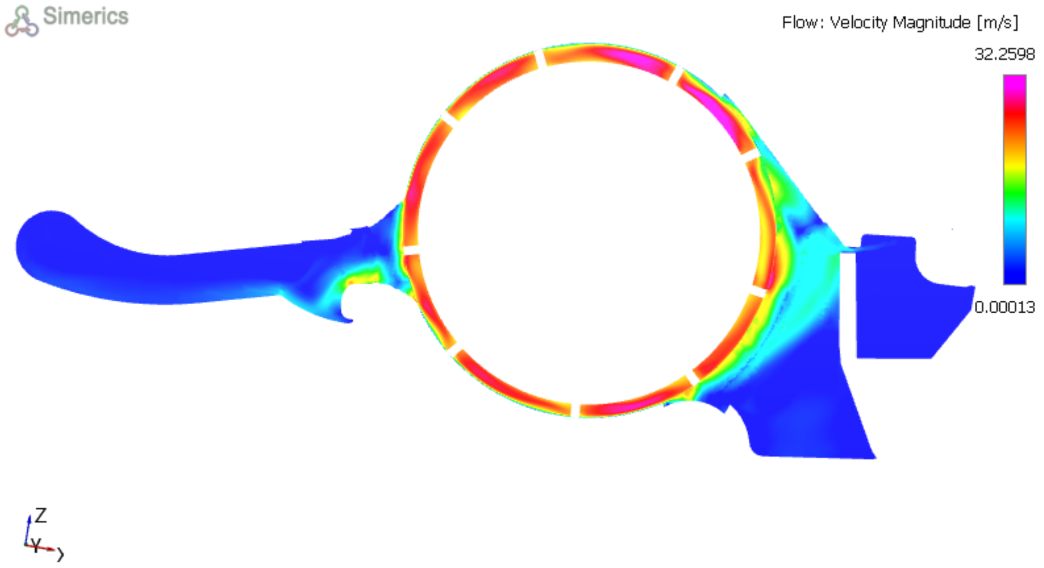

Fig. 5.5 Velocity magnitude contour of VDVP at 5000rpm and 50ºC in steady state

5.1.3 Instantaneous gaseous cavitation contours

The contours below represent the gaseous cavitation at 100ºC and 50ºC. Although the contours are instantaneous, the pump operates steadily, and the simulation converges at this time step. The distribution of the total gas volume fraction is adequate to reflect the gaseous cavitation inside the pump.

Both simulations at 100ºC and 50ºC contain mixture of 6% gas by volume in the oil, which is equivalent to 9×10^{-5} gas mass fraction. This value is common in the engineering application, and often observed in daily driving conditions. [22] Additionally, the cavitation at various gas fraction is presented in section 5.1.6.

In both cases, the lowest gas volume fraction is observed in the outlet (less than 1%), and a higher value is observed in the inlet (less than 7%). The fraction is calculated by dividing the total gas volume by the fluid domain volume. The highest value is near the vane inside the chambers. Specifically, 30% of the gas volume fraction occurs near the vane tip on both adjacent chambers and the inlet domain. The first reason is that the local low pressure due to vane rotation leads to the gas bubble growth. As stated in Section 5.1.1: The rapid rotation motion causes low pressure in the local fluid domain because the inertia of fluid mass does not allow it to follow the vane motion. To be specific, the fluid enters the chamber and is driven by the rotation motion from the drive shaft. Under 5000 rpm, the vanes that form and separate the chambers rotate rapidly. The fluid on the trailing side of the vanes cannot perfectly follow the motion of the vanes because of its inertia. As a result, the trailing side of the vane will generate low pressure. The resulting low pressure tends to help the dissolved gas escape or help the gas nuclei grow. The second reason is the leakage flow in the vane tip clearance trend to develop into the cavitation vortex, as stated in the section 3.2.3. The resulting gaseous cavitation is reported in the figures 5.6, where the purple area means at least 30% volume is occupied by gas.

Additionally, the high gas content area exists only near the vane, where the gaseous cavitation starts. The outlet side, however, does not have a significant amount of gas in the fluid. The outlet pressure is as much as 9×10^{5} Pa, so the outlet and vicinal chambers are under high pressure. The gas bubble will collapse under this pressure so there is no countable gas on the outlet side with 0 - 0.3 scale.

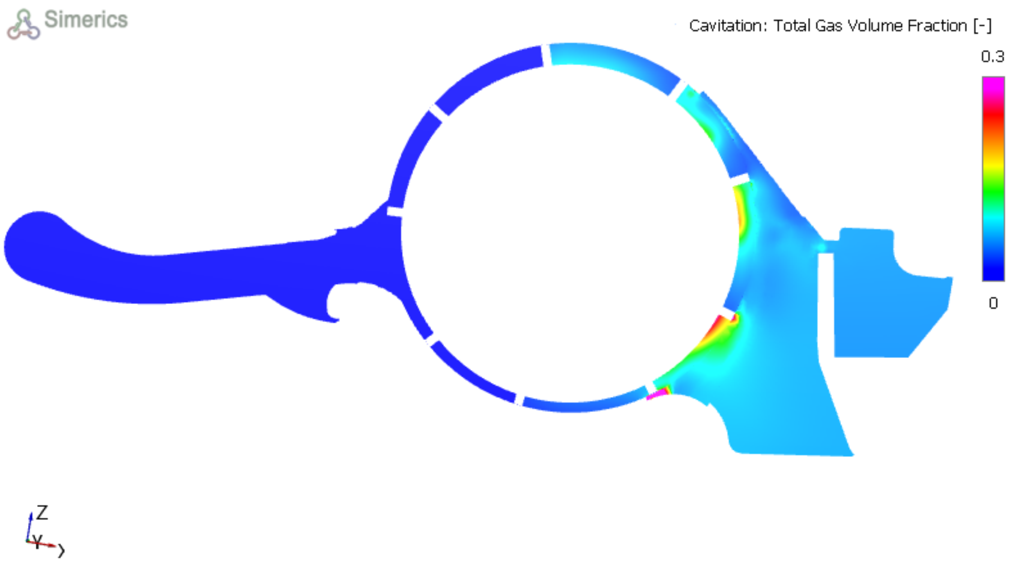

Fig. 5.6 Gaseous cavitation contour of VDVP at 5000 rpm and 100ºC in steady state

The figure below shows the same total gas volume fraction contour with the oil temperature of 50ºC. It is clear that under the same angular speed and inlet gas content, the vane tip generates more gaseous cavitation under 50ºC. Compared to the 100ºC case, the oil viscosity increases when the temperature decreases, causing more difficulty for the oil to follow the vane motion. Therefore, the low-temperature case has more gaseous cavitation. Some large gas cavities propagate from the vane tip to the inlet area.

Additionally, since the cam-ring geometry will affect the inlet flow, the study of alternative cam-ring geometry is also conducted in Section 5.1.7.

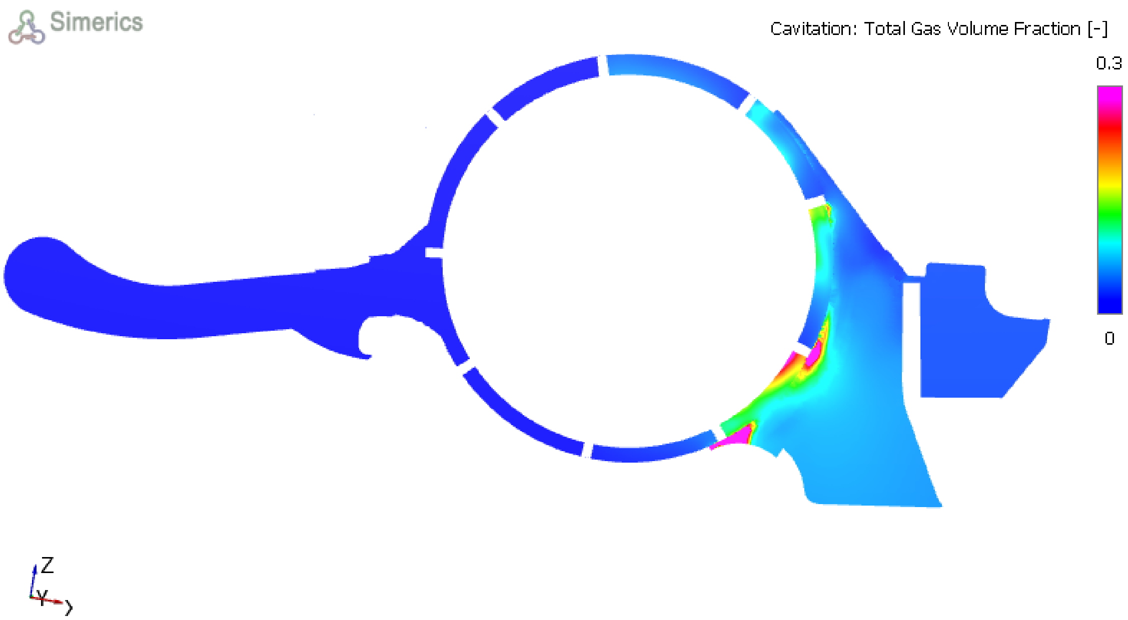

Fig. 5.7 Gaseous cavitation contour of VDVP at 5000rpm and 50°C in steady state

5.1.4 Instantaneous vapor cavitation contours

Fig. 5.8 shows the vapor volume fraction on plane Y=-0.408. The vapor cavitation fraction is four magnitudes lower than the gaseous cavitation. Under the 50°C condition, only $1.1\text{x}10^{-6}$ cm^3 vapor is inside the chambers. Therefore, the pump operation conditions do not cause significant vapor cavitation. For this reason, this section does not include the contours of vapor cavitation. However, the 3D simulation still accounts for vapor cavitation. The vapor cavitation of bearings is included in section 5.2.4 and 5.2.6.

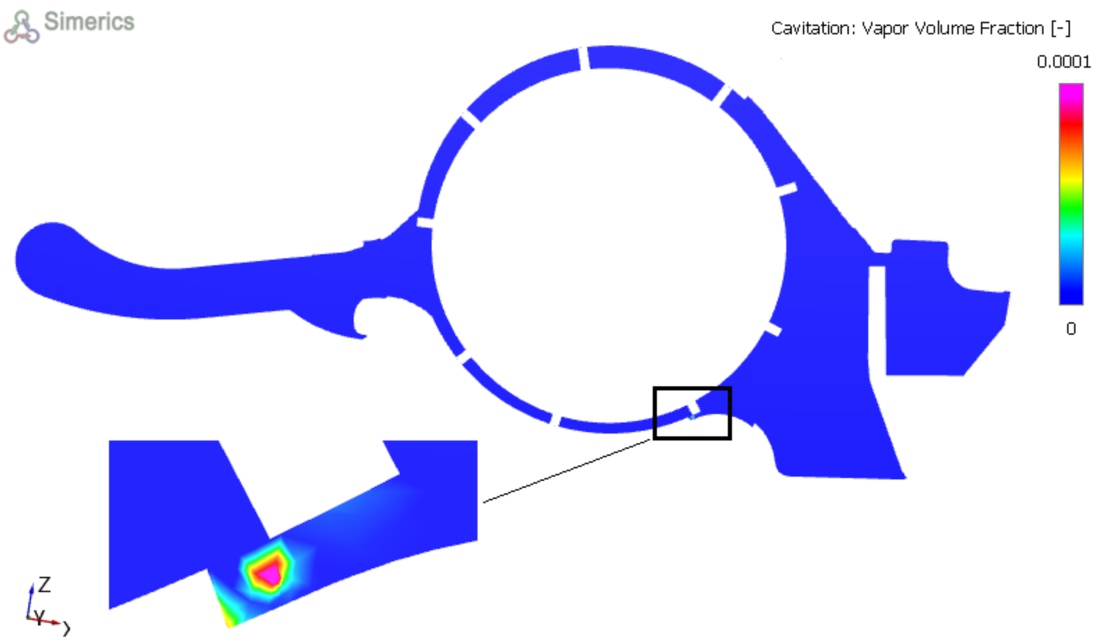

Fig. 5.8 Vapor cavitation contour of VDVP at 5000rpm and 100°C in steady state

5.1.5 Validation of the 3D and 1D simulations at 100°C and 50°C

5.1.5.1 Flow rate vs angular speed curves

The experiment data of the VDVP in this thesis was provided by the SLPT automotive. The experiment setup consists of an oil sump, VDVP, eccentricity control unit, and apparatus for flow rate and pressure measurements. The VDVP recirculate the oil from the sump. The flow meter and manometer are installed in the delivery pipe to monitor the flow rate and delivery pressure, which are controlled by the eccentricity control unit.

The pump performance is tested in the speed sweep where the pump speed was varied from lowest to highest rpm, and back down to the lowest speed. The normalized experimental data are shown in Fig. 5.9. The solid curve represents the experimental delivery flow rate at each rotational speed. The discharge flow rate initially increases linearly with increasing rpm and stays almost flat at higher rpm. The volumetric loss at low speed is due to the flow leakage. At 1000 rpm a sharp peak is observed outside the linear range when the rotational speed is increased. For comparison, the experimental flow curve returning from 7000 rpm to 600 rpm is used for comparison with numerical models. For a fixed displacement vane pump at 50% to 100% of its maximum speed, its flow rate and speed will not maintain a linear relationship because insufficient filling of chambers occurs. [23] The insufficient filling indicates the volume of liquid is occupied by the gas, implying the onset of cavitation. What's more, the flow under cavitation will significantly decrease. However, this thesis requires the pump to meet a constant delivery flow target for the downstream oil circuit. Therefore, the flow rate curve will remain constant after 2000 rpm in the figure 5.9.

The pump flow rate is decided by its speed and displacement. The drive shaft controls the speed, and the eccentricity controls the displacement. The large eccentricity means the chamber volume has more deformation over one revolution, which will suck and expel more liquid. As shown in the section 3.3.2, the hydraulic mechanism will control the eccentricity accordingly to maintain the delivery flow rate at proper values.

As discussed in section 4.1.3, the outlet pressures in the simulations are set to match the conditions in the experiments, where the inlet pressure is set to be equal to the atmospheric pressure at 101 kPa. The simulation results for the delivery flow rate are collected after the pump operates in a steady state condition. As Fig. 5.9 shows, both the flow rate results extracted from the 3D and 1D models for several speed over the entire operating range. For the 100°C, the max and mean error between the simulations and experimental data are ±8% and ±4%, respectively.

Figures in section 5.1.5.1 and 5.1.5.2 are normalized with the maximum flow rate recorded in the experiment.

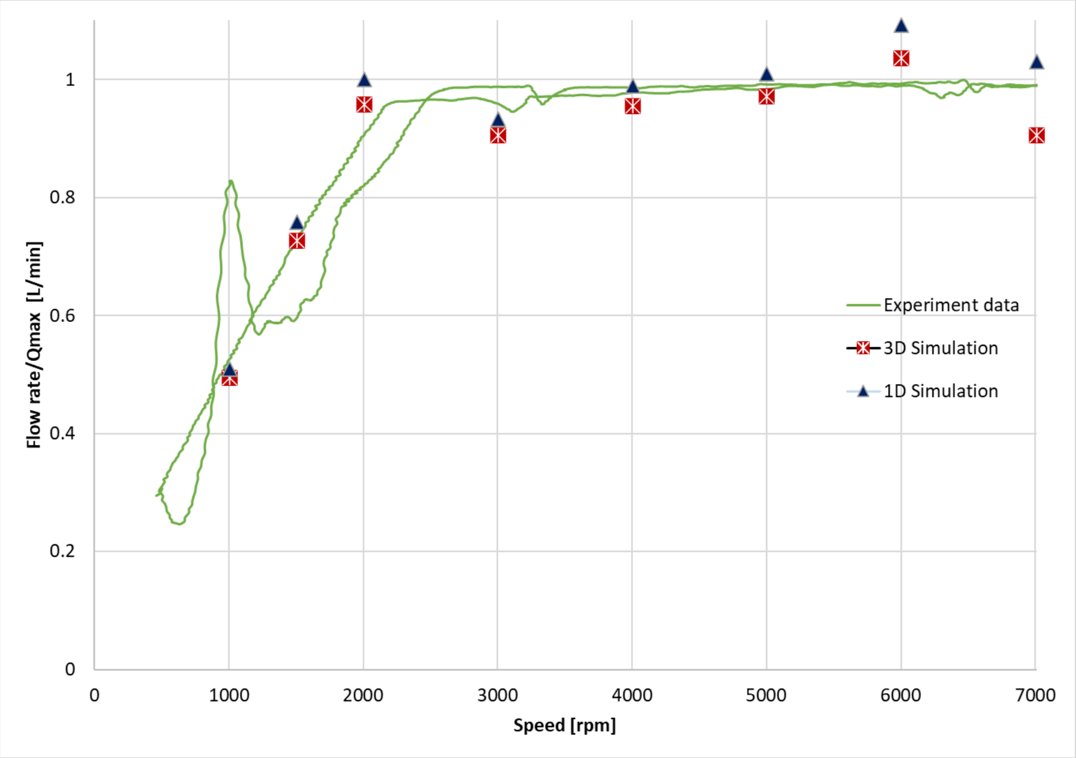

Fig. 5.9 Comparison between the normalized experiment data and numerical (3D and 1D) results at 100°C

For the 1D mode, the max and min errors are ±8% and ±4%. A more visual correlation between the numerical and experiment data is included in section Regression analysis of simulation results5.1.5.2.

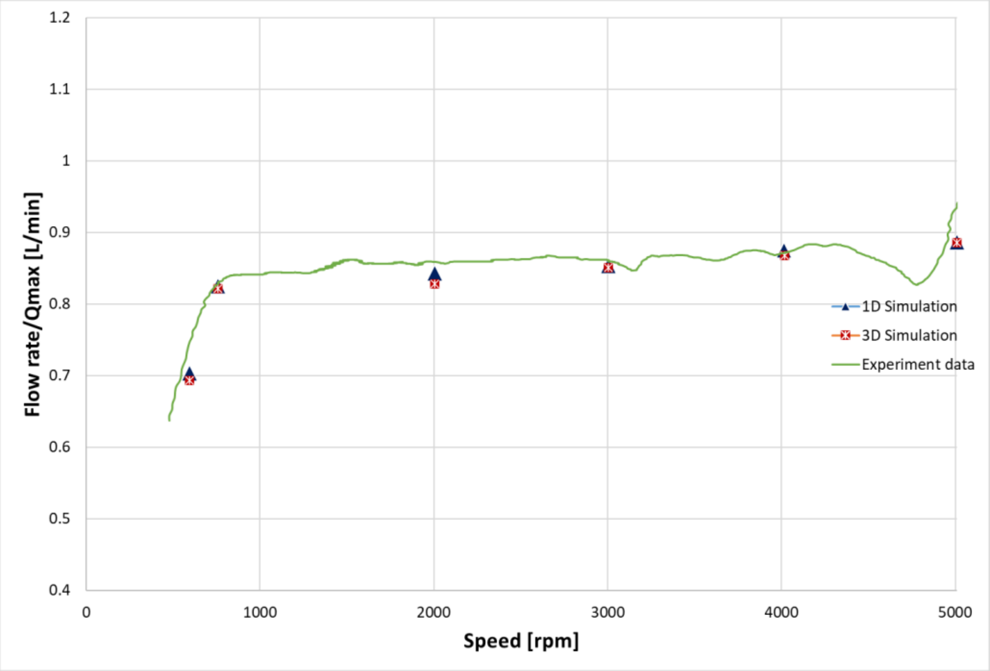

Fig. 5.10 Comparison between the normalized experiment data and numerical (3D and 1D) results at 50°C

Additional experiments at different temperatures are conducted and the performance of the pump is compared with the results from the numerical model. Fig. 5.10 compares the results from the experiments with numerical results at temperature of 50°C. The solid curve represents the pump flow rate from the experiment. In this figure, only the ramp-up half of experiment data was shown. The linear phase starts from the minimum speed and shortly ends at 800rpm. After that, the delivery flow is maintained at a pre-set level to meet the requirement of the oil circuit. At the high rpm range, the pump experience high flow rate fluctuation. The uncertainty from the experiment determines that it does not respond to the speed sweep test ideally. For the same reason, experiment data at high speed (5000-7000rpm) was not used for model validation.

The triangle points represent the 1D simulation results, and the squares represent the 3D simulation result. The average and maximum errors for 3D simulations are ±3% and ±7%, and the errors for 1D simulations are ±2% and ±6%. The regression analysis results are included in Fig. 5.12 below.

5.1.5.2 Regression analysis of simulation results

The figure correlates the normalized experiment data and simulation results with the regression analysis method. This figure includes the same normalized data as Fig. 5.9, and it is meant to provide a more direct comparison with the experimental data. Most of the flow rate data points are located around the 0.9 – 1 since the pump flow rate is maintained nearly constant at high rotational speeds.

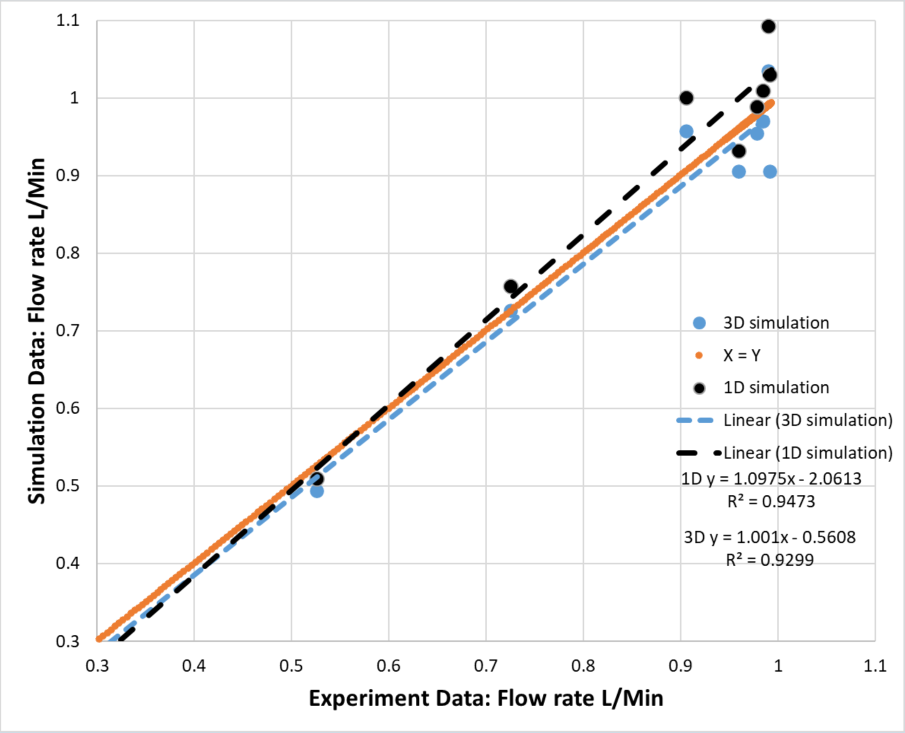

Fig. 5.11 Correlation between the normalized experiment data and simulation results at 100°C

The solid orange line is the perfect fit between the simulation flow rate equals the experiment data. The blue dots represent the flow rate from the 3D simulation, and the blue dash line is the fitting line of these dots. The regression analysis shows that the fitting line slope is 1.001 and interception is -0.5608. The R-square value is 0.9299, which means the line fits into 92.99% of the data points. Similarly, the black dots represent the flow rate from the 1D simulation, and the black dash line is the fitting line of these dots. The regression analysis shows that the fitting line slope is 1.0975 and the interception is -2.0613. The R-square value is 0.9473, which means the line fits into 94.73% of the data points.

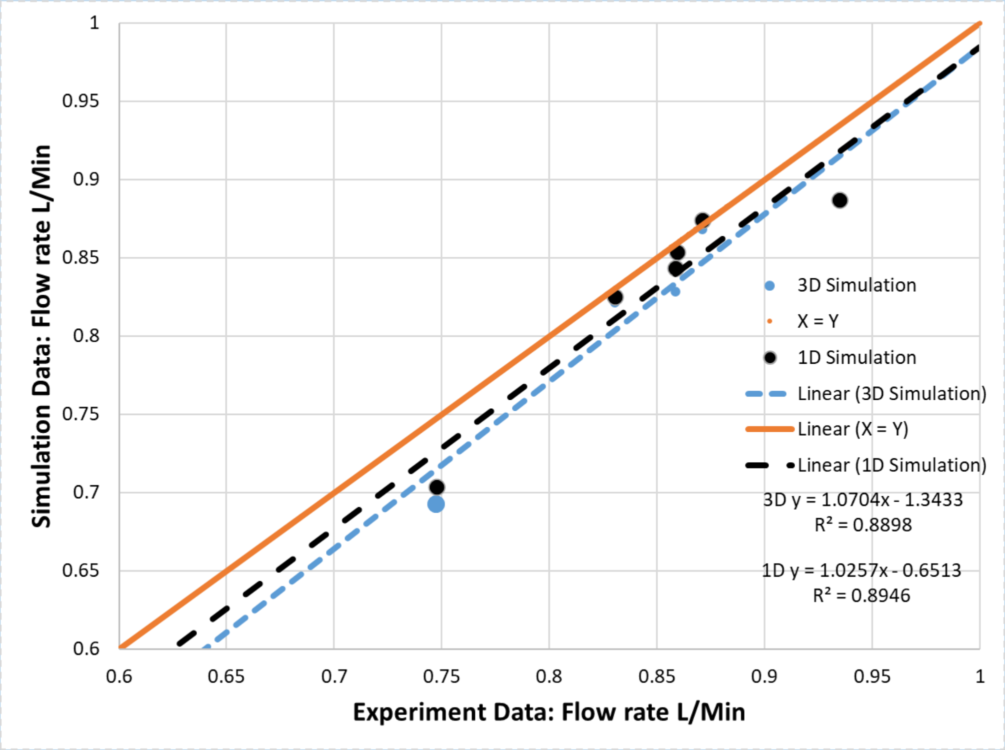

Fig. 5.12 Correlation between the normalized experiment data and simulation results at 50°C

According to the regression result of 100°C data, the 3D model has less interception, and the slope is almost equal to one, meaning it is close to the perfect fit. Neither of the 50°C results is close to the perfect line, but the 3D fitting line still has less interception, meaning it is closer to the perfect fit. Thus, the 3D simulation is recommended for VDVP simulation for accuracy.

5.1.6 Cavitation sensitivity test to initial gas volume fraction

The cavitation sensitivity test was performed for the validated pump model discussed in section 5.1.5. The test results are obtained from both the 3D CFD and 1D models for comparison and the boundary conditions are listed in Table 1. The simulations for each case were carried out with the same boundary conditions. Three inlet gas volumetric fraction (5%, 10% and 15%) in the infinity inlet oil flow are tested for 1D and 3D models. In this study, 15% is considered the maximum gas content as the engine oil does not contain more gas than this value in practice. [4] The eccentricity angle is defined as the angle that the eccentricity-ring/cam-ring has rotated from the at-rest (maximum displacement) position.

Table 1 Boundary conditions for cavitation sensitivity test

Boundary conditions	
Inlet pressure (Pa)	101325
Outlet pressure (Pa)	714325
Temperature (°C)	100
Eccentricity angle (degrees)	2.2

The results of the cavitation sensitivity test from simulations are shown in Table 2, where cases 1-3, and cases 4-6 are obtained from 1D simulation, and 3D simulation, respectively. 1D simulations generally have a higher gas fraction in each fluid domain, resulting in a lower effective flow rate. The effective flow rate is the actual volume of fluid passing per unit time when the outlet is fluid-air mixture. (The reason is that the 1D simulation adopts the lump parameter system. It characterized the inlet by its volume, area, and opening angle. The influence of the geometry on the cavitation is not fully considered in the 1D model.) The overall difference between the 1D and 3D simulation results for the gas fraction is less than 15% on average. Moreover, the difference between cases with 10% and 15% initial gas contents is 9%.

The initial gas volume fraction in the infinity supply oil defines the gas amount at the simulation's beginning. [21] This quantity is applied to the sub-sections in the pump, and it will change as the simulation progresses. As table 2 shows, the gas fractions are generally higher in the inlet and chambers, and lower on the outlet: Both 1D and 3D CFD models reveal that the gas volume fraction in the inlet region is higher than the gas fraction in supplied oil. The vane rotation creates a low-pressure zone in the inlet domain, and the gas bubble in oil will expand as the supplied oil enters the inlet. More specifically, the gas volume is high on the inlet and suction side of the rotating chamber. As soon as the chambers reach the outlet side, the local high pressure will compress the gas bubbles into smaller volumes. As stated before in the literature review, the bubble volume affects pump operation and oil supply to downstream components.

Table 2 volumetric gas fraction in different fluid domain under various initial gas content

	Volumetric Gas Fraction (%)					
	1D			3D CFD		
Flow Domain	case 1*	case 2	case 3	case 4	case 5	case 6
Initial	5.00	10.00	15.00	5.00	10.00	15.00
Inlet	6.67	11.69	16.65	5.50	10.50	15.20
Chamber	5.05	8.02	10.94	4.00	8.00	11.20
Outlet	1.03	1.82	2.68	0.72	1.54	2.42
Delivery pipe	1.04	1.82	2.69	0.73	1.50	2.45
Environment	0.00	0.00	0.00	0.00	0.00	0.00
Flow Rate L/min	34.02	30.86	28.32	36.50	33.50	31.00

*Note that the initial gas fraction in suppled oil for cases 1 and 4, cases 2 and 5, and cases 3 and 6 are 5, 10, and 15 %, respectively. The information is obtained from the lump system, or integral over the fluid domain from the 3D model.

5.1.7 Cavitation sensitivity test to alternative cam-ring designs

Two alternative eccentricity ring designs are implemented in the 3D numerical model to examine their effect on cavitation. The reason, set-up and results are included in this section.

Rundo et al. [24] have proved that the inlet side geometry of the eccentricity ring has a high impact on the vane pump fill efficiency, which leads to different delivery flow rates. Similarly, it is believed that the alternative cam-ring designs on this pump will also affect the delivery flow rate. The reason is that different cam-ring configurations on the inlet side will influence the cavitation severity inside the pump.

The figure below shows the view of the variable vane pump from the inlet flow direction. Although it is a sliding-type VDVP, the main configuration of the inlet, eccentricity ring, chambers and outlet is similar to the pivoting type VDVP in this thesis. What's more, the eccentricity of this sliding pump was fixed, so it is considered as a conventional vane pump. This thesis adopts this method in this section, so the pivoting VDVP also operates as a fixed displacement conventional vane pump.

As shown in the figure, the black arrow to the right indicates the rotation direction, and the blue arrow pointing into the paper indicates the direction of the incoming flow. The red solid that the blue arrow points to is the eccentricity ring. It separates the inlet flow and the fluid inside the pump chambers. In other words, the incoming oil from the sump must flow through the eccentricity ring before entering the pump chambers. Parameters h1 h2 are the height of the additional milling on the eccentricity ring. Some inlet flow will flow into the chambers through the millings. It has been proved the different heights of the milling significantly influence the chambers' filling capability. [24]

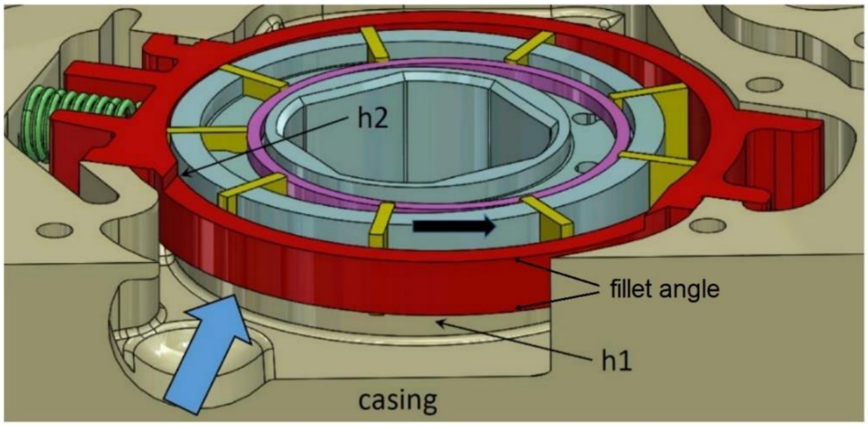

Fig. 5.13 View of the pump from the inlet pipe with the indication of the direction of the flow, the location of the cuttings h1 and h2, and the direction of rotation (black arrow). [24]

This section is dedicated to studying the effect of different cam-ring designs on the introduced cavitation. Different configurations are achieved by altering the fillet angle on the edge of milling. Compared to the original design, the alternative design A has a smaller fillet angle on the incoming side of the cam-ring, and design B has a more significant fillet angle on the incoming side of the cam-ring. The only differences are the cross-section shape on the incoming side, shown in Fig. 5.14.

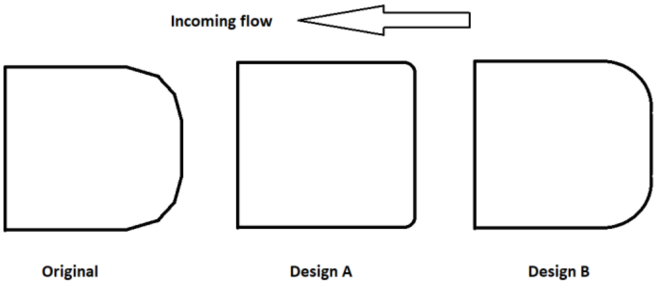

Fig. 5.14 Cam-ring cross-sections designs

Table 3 includes the boundary conditions in the study. Note the eccentricity angle is defined as the angle that the eccentricity-ring/cam-ring has rotated from the at-rest (maximum displacement) position. Each simulation case runs for 15 revolutions in total. Since the model requires the first few revolutions to prime the pump and reach convergence, only data of the last three revolutions are recorded to examine the cavitation response to each cam-ring design.

Table 3 Boundary conditions for cam-ring design test

Boundary conditions	
Inlet pressure (kPa)	101.3
Outlet pressure (kPa)	714.3
Temperature (^oC)	100
Eccentricity angle (degrees)	2.2
Inlet gas volume fraction	5% 10% or 15%

The cavitation development within one revolution of the shaft is present in

Fig. 5.15. The figure includes the 3D view of the gas volume fraction of pump chambers that rotate counterclockwise. The adjacent inlet on the right and outlet on the left are shown in Fig. 5.1. The 3D view is more effective than the 2D view in simultaneously visualizing the cavitation development on the inner and top surfaces of the fluid domain. Six snapshots are included for one case, and each is 60 degrees apart. The developed cavitation mainly occurs on the inlet side of the rotating chambers, which are the chambers on the right of each snapshot. Precisely, the large bubbles locate near the trailing side of vanes and the tip clearances of vane tips. The rapid motion from the vanes will dramatically decrease the local pressure of the nearby fluid, and the nuclei and dissolved gas will develop into cavitation. The leakage flow in the vane tip clearance could also introduce the cavitation vortex. The cavitation bubbles will further develop in the local low-pressure zones. As the chambers rotate counterclockwise, the bubble size gradually decreases while approaching the high-pressure side of the pump. The bubbles inside the pump chambers significantly affect the filling capability and the delivery flow rate. The qualitative analysis of the cavitation bubble inside the chambers and its influence on flow rate are discussed next.

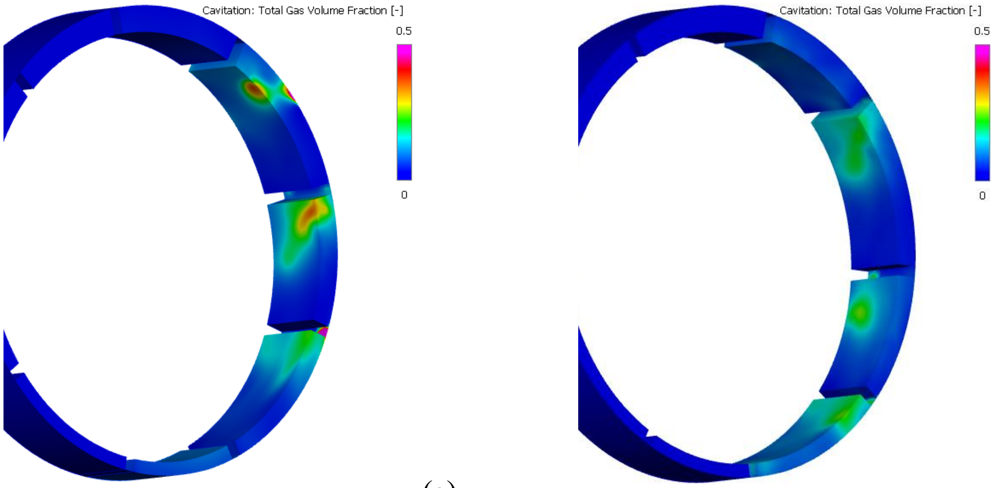

(a) (b)

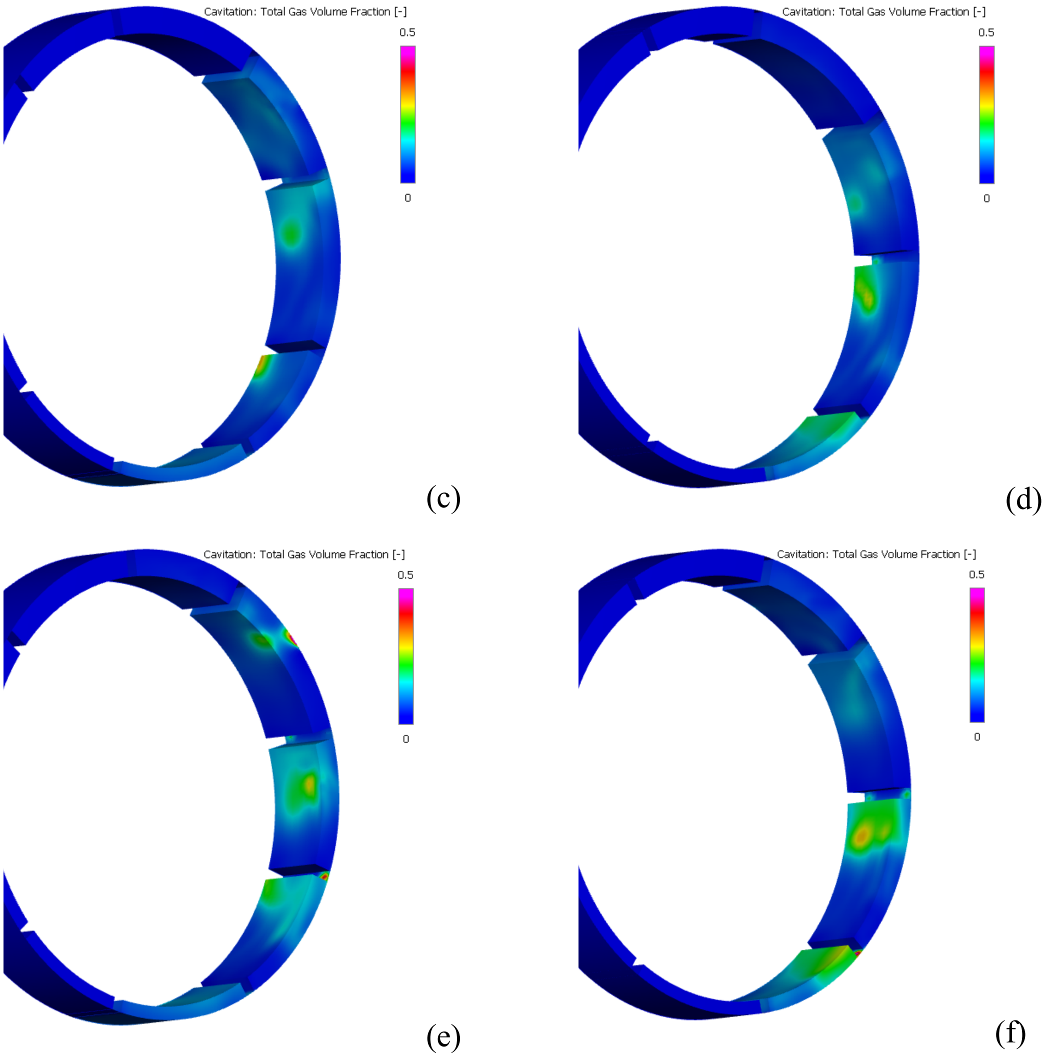

Fig. 5.15 3D view of cavitation development in VDVP chambers to show gas volume on the inner and top surfaces simultaneously. The chambers rotate in counterclockwise direction.

Table 4 summarizes the average total gas volume fraction (The average volume fraction of the free NCG, dissolved gas, and vapor in a liquid for a selected volume. [25]) of each cam-ring design with several initial aeration levels. The data record the average value over eight revolutions or 2880 time-steps after the pump model operates in steady condition. Design A has the highest total gas volume fraction in the rotating chambers with all three initial gas content. Meanwhile, design B has the least total gas fraction under different initial gas content. The three cam-ring designs will introduce cavitation in the following order: Design A> Original Design > Design B.

As discussed in the section 5.1.1, the vapor cavitation only occurs under extreme conditions. Vapor volume in rotating chambers is less than 1x10^{-5} cm^3 for all cases. Thus, it will not be further discussed in this section.

Table 4 Cavitation: total gas volume fraction on chambers

Chambers: Total gas fraction			
Initial	Design A	Design B	Original
5%	0.0538	0.0373	0.0410
10%	0.104	0.0725	0.0790
15%	0.140	0.104	0.107

Fig. 5.13 above use the blue arrow to indicate the direction of inlet flow entering pump chambers. Following this direction, Fig. 5.16, Fig. 5.18, and Fig. 5.20 plot the gaseous cavitation on the interfaces where the fluid from the millings enters the chambers. The Fig. 5.17,Fig. 5.19 and Fig. 5.21 however, show the gas volume fraction on the millings in a 3D view.

Fig. 5.17 shows the developed cavitation near the vane tip clearance of design A. The solid vane directly contacts the inlet domain. After the vane sweeps through at high velocity, it leads to a low-pressure zone after itself. The cavitation will likely develop in this low-pressure zone. The figure shows the cavitation indicated by the red area, where 70% of the volume is occupied by gas.

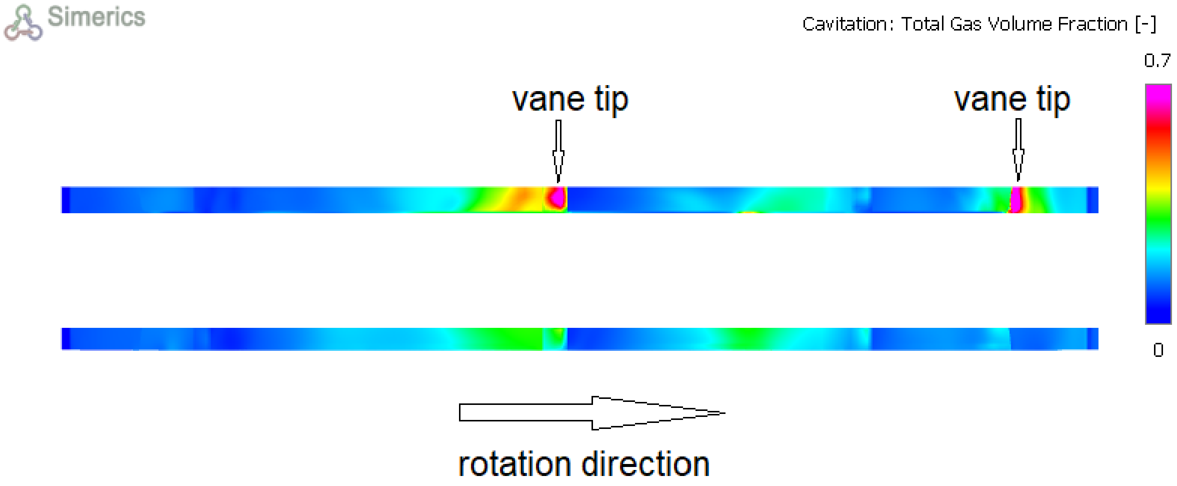

Fig. 5.16 Instantaneous gaseous cavitation observed from the inlet port: Design A

The figure below shows the corresponding gas volume fraction in the adjacent milling volume. The two arrows indicate the locations of the solid vane blades, whose tips contact the inlet fluid domain. Specifically, the vane tips are in contact with the fluid inside the millings. The cavitation bubbles near the vane tips do not only exist in the interface. They further expand in the nearby fluid, as the figure Fig. 5.17 shows.

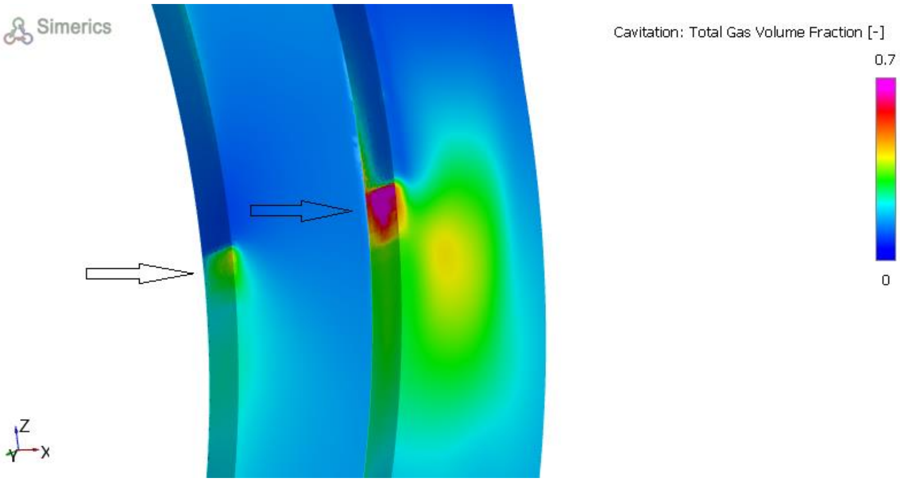

Fig. 5.17 Cavitation development near the vane tip of design A. The arrows show the location of vane tips.

The figures below visualize cavitation near the original design and design B, respectively. It is clear cavitation occurs near the vane tips in both designs. It is clear cavitation occurs near the vane tips in both designs. However, the original design has a larger gas volume, meaning it would introduce more cavitation than design B.

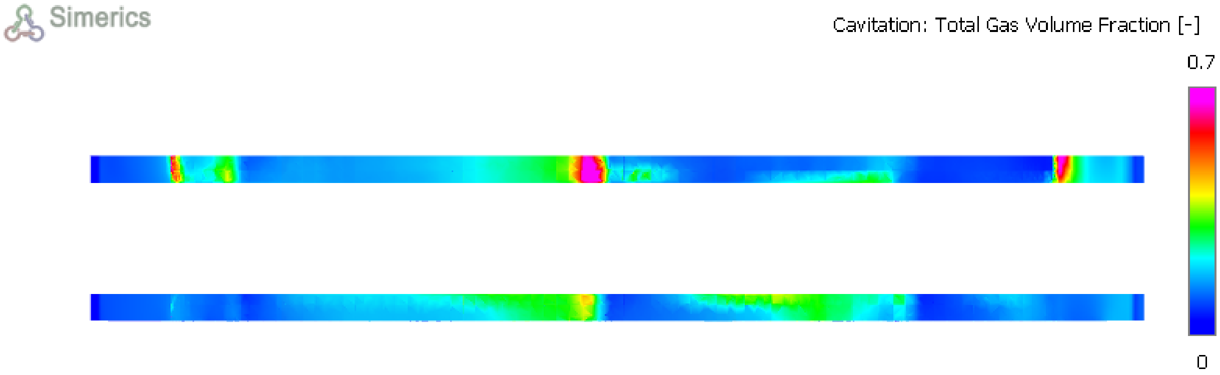

Fig. 5.18 Instantaneous gaseous cavitation observed from the inlet port: Original design

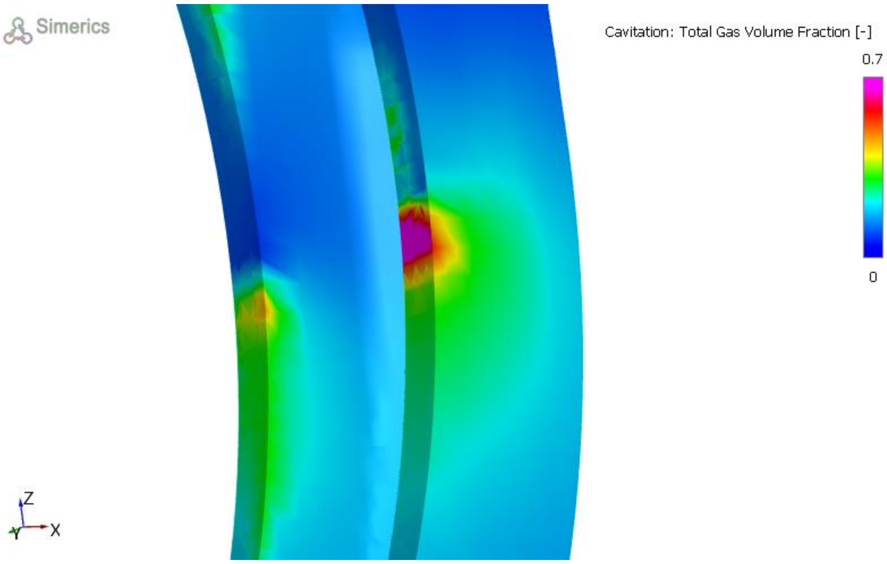

Fig. 5.19 Cavitation development near the vane tip of the original design

The design B has less gas volume near the vane tip, meaning the design would introduce less cavitation under the 5000 rpm and 100ºC. Table 4 also reveals the trend that the design B would introduce the less cavitation into the pump chambers. In summary, the cavitation onset in the three cam-ring designs is in the following order: Design A> Original Design > Design B.

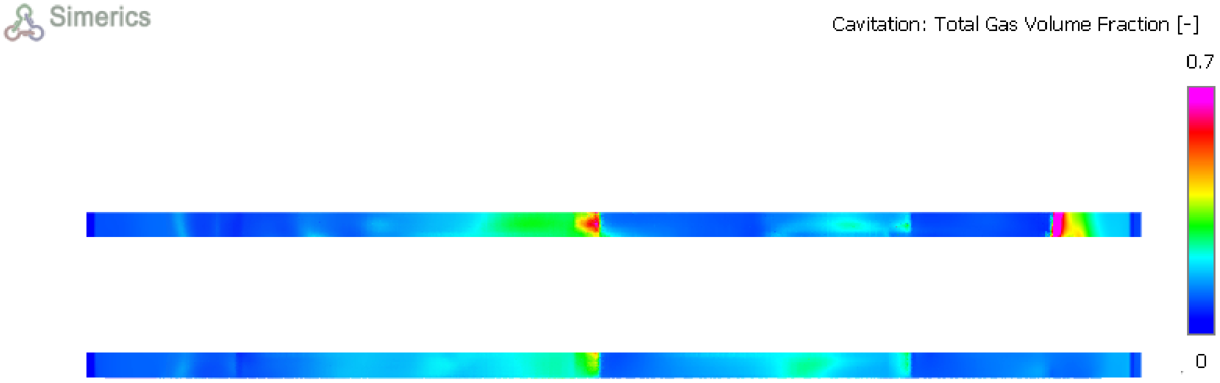

Fig. 5.20 Instantaneous gaseous cavitation observed from the inlet port Design B

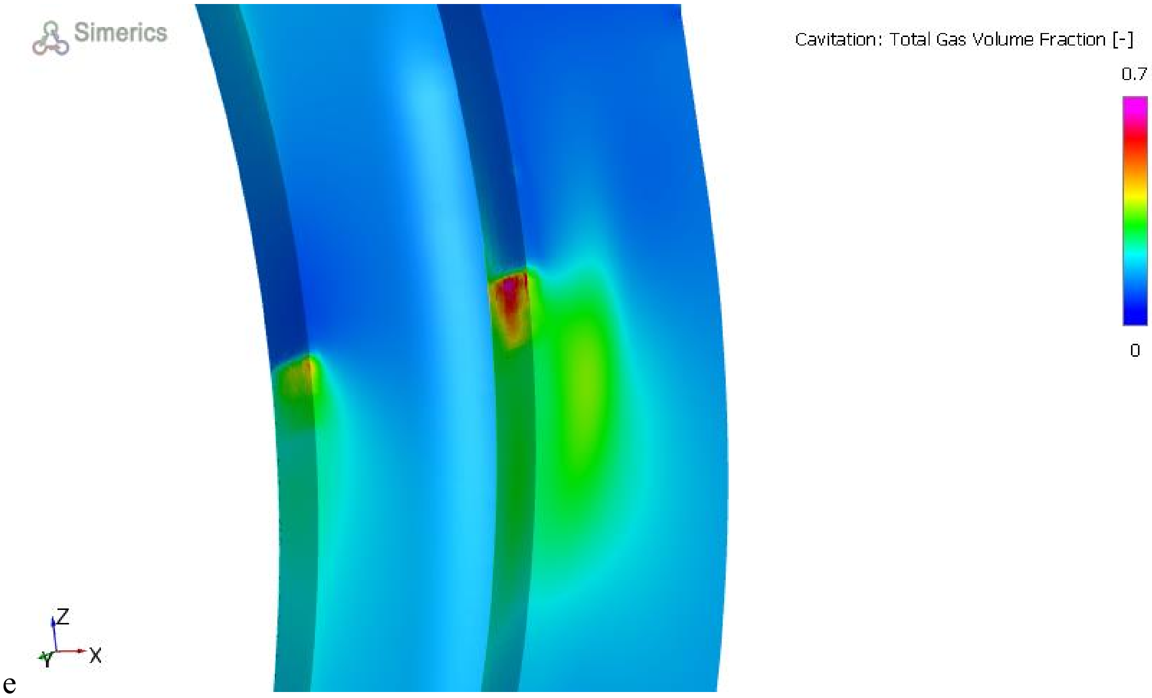

Fig. 5.21 Cavitation development near the vane tip of design B

To understand why design B introduces less cavitation into the pump, the Fig. 5.23 compares the radial velocity of inlet volume along the chambers. The Fig. 5.13 shows that the upstream fluid domain of the chambers is in a thin disc shape that surrounds it. Therefore, the radial velocity is much more prevailing than the axial or tangential velocity in the milling zone, especially for flow effectively entering pump chambers. Radial velocities of designs A and B with 15% initial gas fraction are plotted in the figure below, with the probe located 1mm from the edge as

Fig. 5.22. The inlet volume begins at crank angle 123° and ends at 237° clockwise. Design B's radial velocity profile has fewer fluctuations after 180°, where the counterclockwise rotating chambers first attach to the inlet volume. From 123° to 150°, design B has a larger radial flow before the chambers are about to detach from the inlet. In general, design B has less flow fluctuation and more positive radial velocity.

The outlet flow rate of design B is reported as 6% more than design A. It shows that the cam-ring geometry can affect the inlet radial velocity to change the outlet flow rate.

Moreover, design B is the optimized configuration for deducing cavitation and increasing filling capacity.

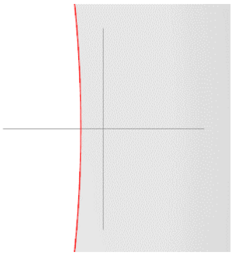

Fig. 5.22 The location of radial velocity probe is 1mm from the edge of the edge of inlet domain.

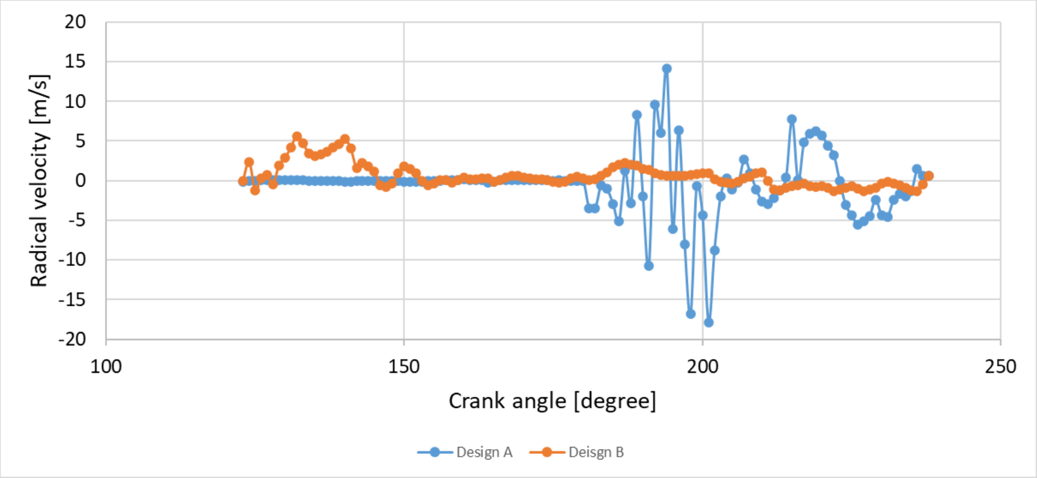

Fig. 5.23 Radial velocity along the edge of inlet for crank angles from 123° to 237°

5.2 Bearings

This section is dedicated to the simulation results from the 3D and 1D bearings models. The OEM provided the bearing distortion and orbiting data. It is necessary to modify these data to set up the bearing models successfully. The modification might cause a deviation from expected simulation results, which is identified in the corresponding sections.

5.2.1 Distortion

The main bearings and connecting rod (conrod) bearings are deformed during engine operation. The engine load presses the bearing sleeve along the line of the piston stroke. The distorted sleeve is often referred to as the “lemon shape”. Since the bearing sleeves are deformed, the oil in the clearance is also in lemon shape. The main bearing and conrod bearings clearance distortion are shown in the figures below. The distortion magnitude of the bearing shell is exaggerated for visualization. The fluid domain discussed in section 5.2 are the fluid inside the clearance between the bearing shells and crankshaft. The following paragraphs in this section will refer the fluid domain as “bearing” unless specified.

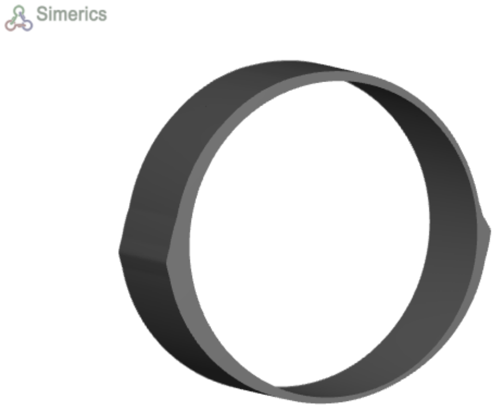

Fig. 5.24 Main bearing lemon shape

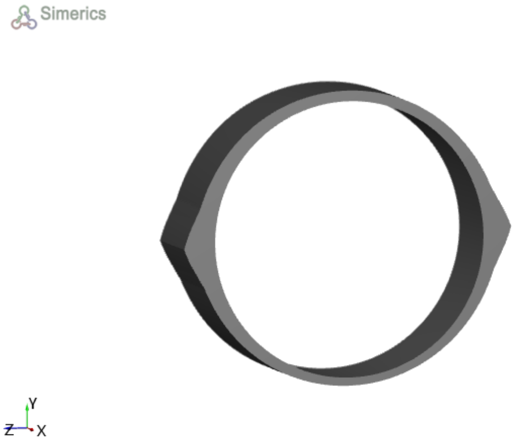

Fig. 5.25 Conrod bearing lemon shape

5.2.2 Bearing model Overview

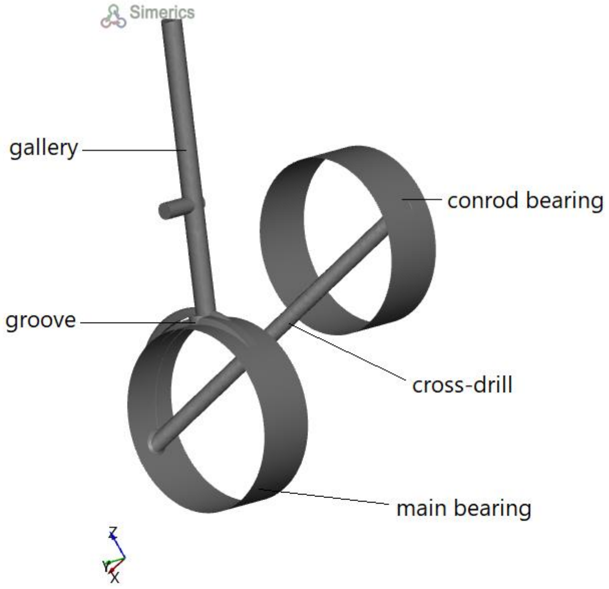

Fig. 5.26 Bearing model overview

The inlet pressure is 4.86 x 10^5 Pa, and the outlet pressure is 1.01x10^5 Pa. The inlet oil contains 6% of gas in volume. The gravity acceleration 9.81m/s^2 is included into the bearing model. The bearings are installed on a four strokes engine rotating with 4000rpm. The bearing distortion and orbiting data is modified to characterize the clearance deformation. The bearing clearance shape varies over the four strokes, so the cavitation over 720° is collected from the simulation. Fig. 5.26 is observed from the "front" side or "node" side of engine. The same perspective will be used for the following sections as well. For example, the conrod bearing in Fig. 5.26 is considered on the top right of the main bearing in the 3D space.

The oil contains 6% of gas in the oil.

The Fig. 5.27 visualize the gaseous cavitation development within one revolution. Each snapshot is 60° apart. Since the bearings are installed on a four strokes engine, snapshots from two revolutions are present to shows the cavitation development over one working cycle.

There is always low gas volume on the top, where the inlet oil enters the bearing, as the Fig. 5.26 shows. The constant oil supply prevents the large gas volume from developing near the groove. The gaseous cavitation in the main bearing is generally located on the top right quadrant. The engine load usually causes the crank to sink inside bearing shells, so the clearance on the upper half is larger than the bottom half. Therefore, the larger gap allows it more possible for cavitation onset.

5.2.3 Main bearing gaseous cavitation

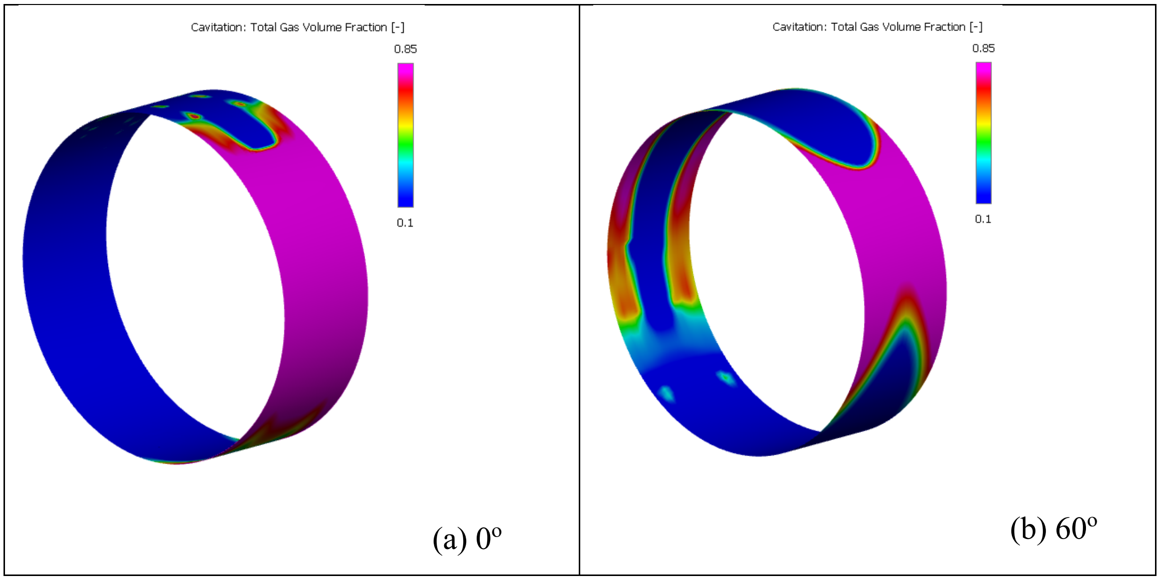

(a) 0°

(b) 60°

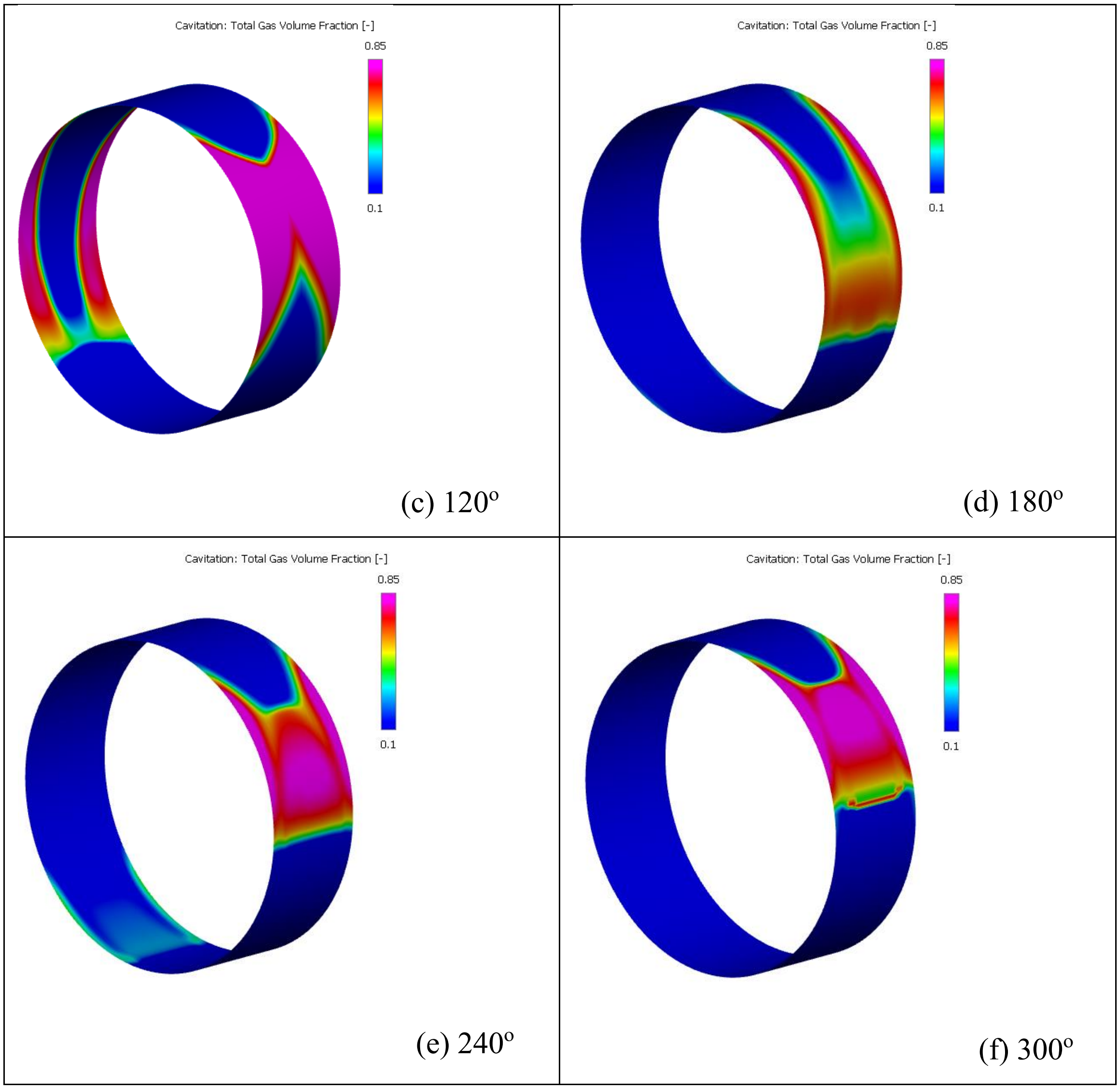

(c) 120°

(d) 180°

(e) 240°

(f) 300°

Fig. 5.27 Main bearing gaseous cavitation from 0° to 300°.

Apart from the constant oil supply, the oil inside the cross-drill could also alleviate cavitation. As figure I below shows, when the interface between the cross-drill and bearings reaches the cavitation area, the centrifugal force inside the cross-drill will expel the oil to fill the cavity. It is the round low cavitation zone among the 0.85 gas fraction area.

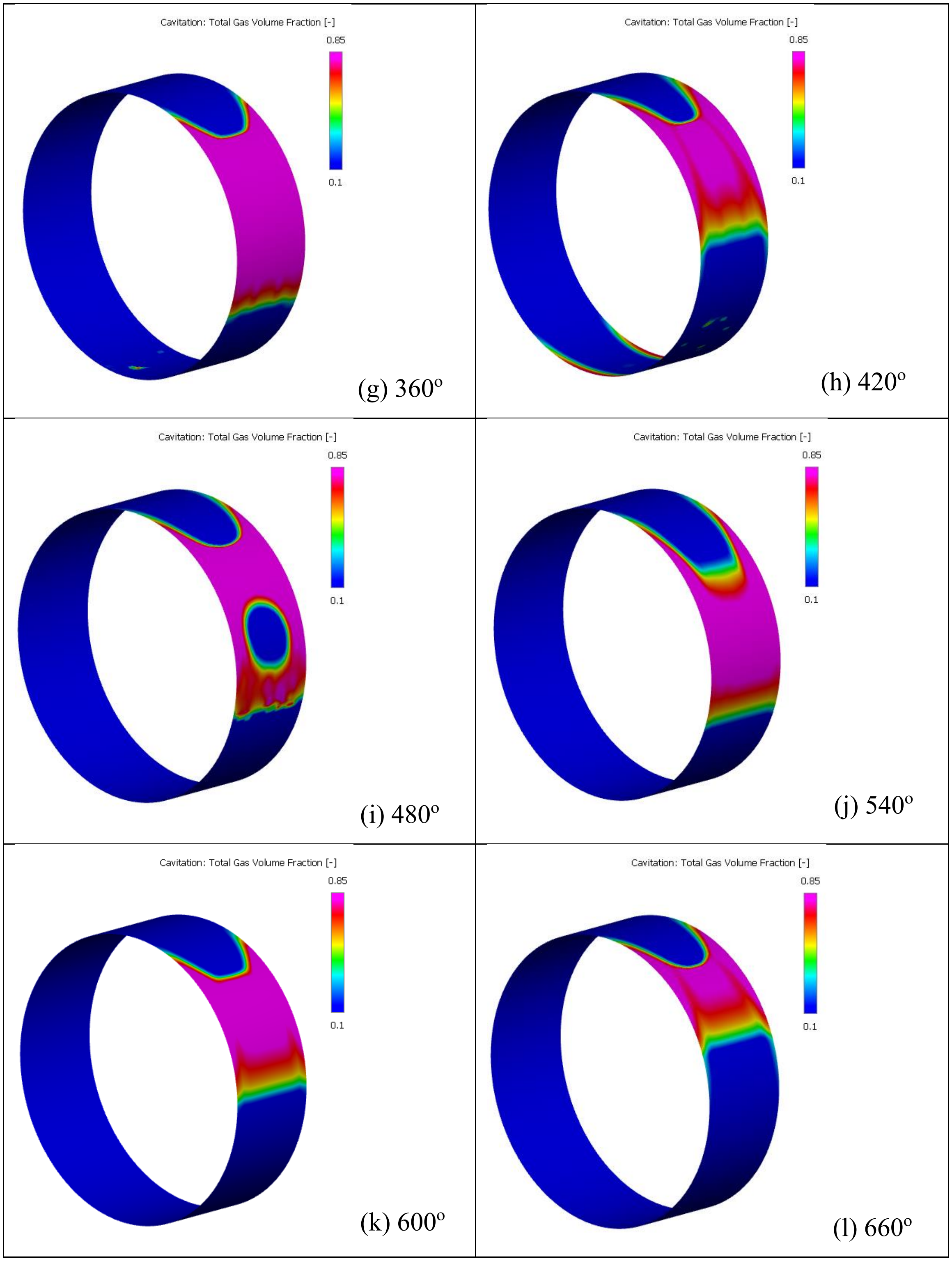

(g) 360°

(h) 420°

(i) 480°

(j) 540°

(k) 600°

(l) 660°

Fig. 5.28 Main bearing gaseous cavitation from 360 ° to 660°

5.2.4 Main bearing vapor cavitation

The vapor cavitation fraction inside the main bearing ranges from $1\text{x}10^{-7}$ to $6\text{x}10^{-13}$. Its magnitude is significantly lower than the gaseous cavitation because the oil vapor pressure is as low as 0.0415 Pa under 100°C. However, figures g to i still capture the vapor cavitation's inception. The vapor cavitation generally distributes at the top right quadrant. The figure g shows the vapor cavitation begins near the end of the "lemon shape." The sudden increase of the thickness favors the cavitation onset.

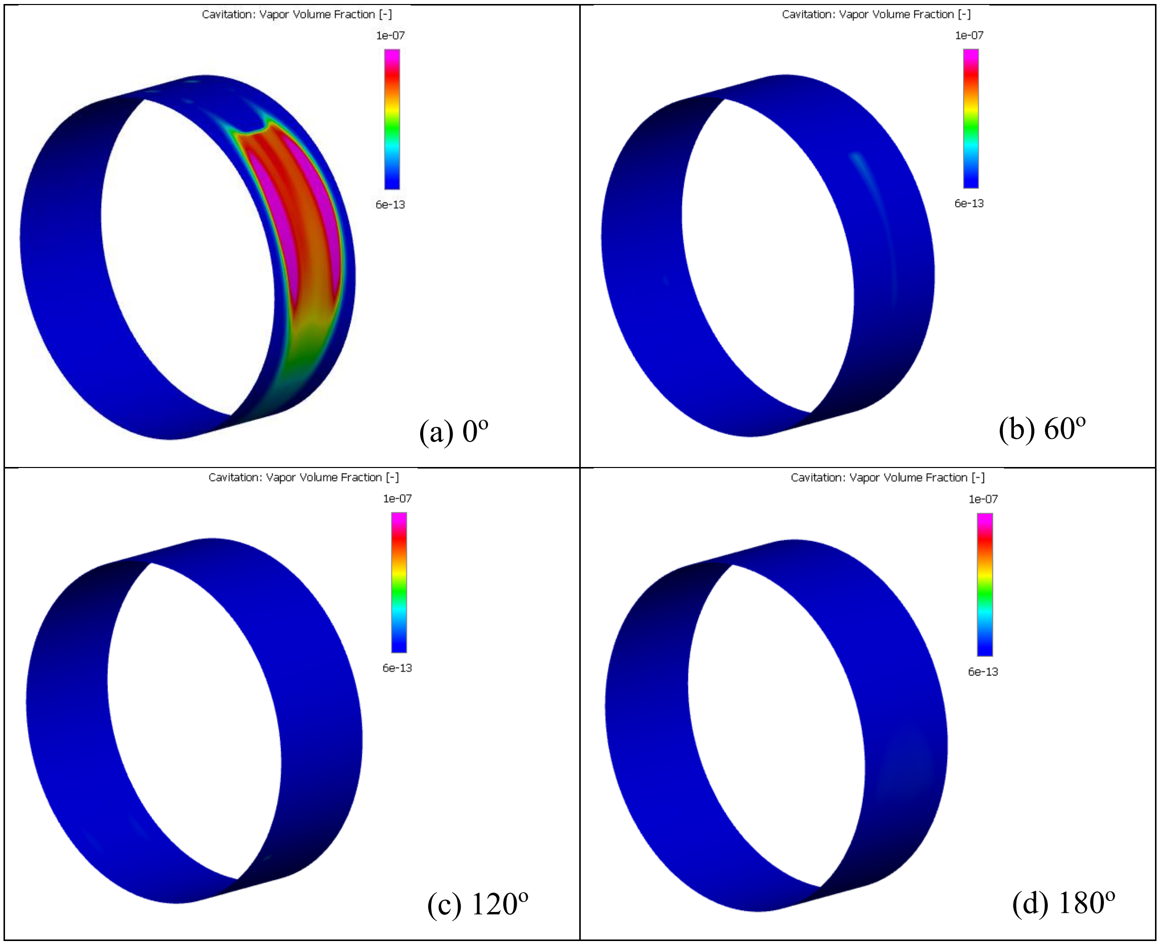

(a) 0°

(b) 60°

(c) 120°

(d) 180°

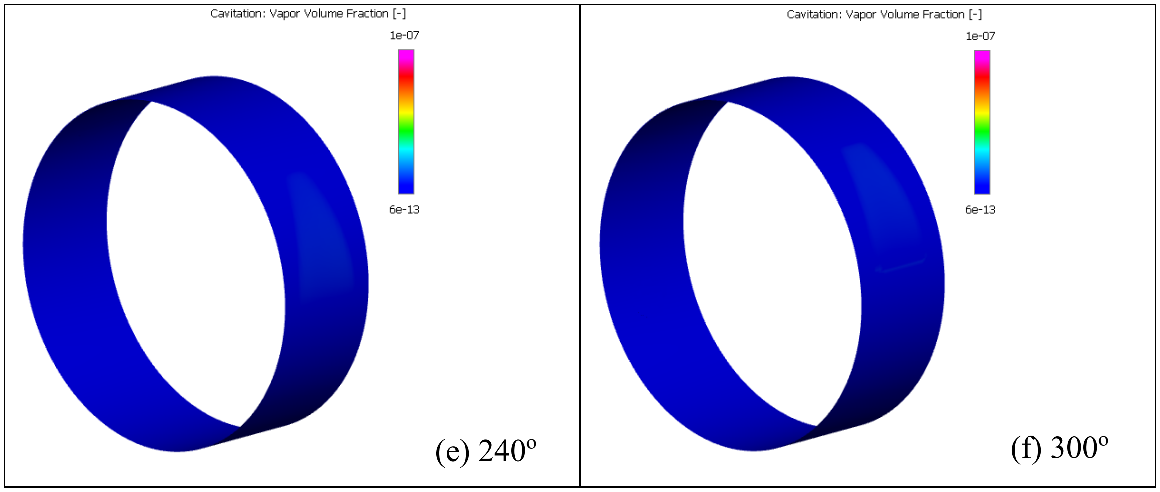

(e) 240°

(f) 300°

Fig. 5.29 Main bearing vapor cavitation from 0° to 300°

In practice, the bearing clearance is a range of thickness rather than a fixed value. This thesis has selected the nominal value of 0.0225mm as the bearing clearance, so the analysis results might not apply to bearings with extreme clearance thickness.

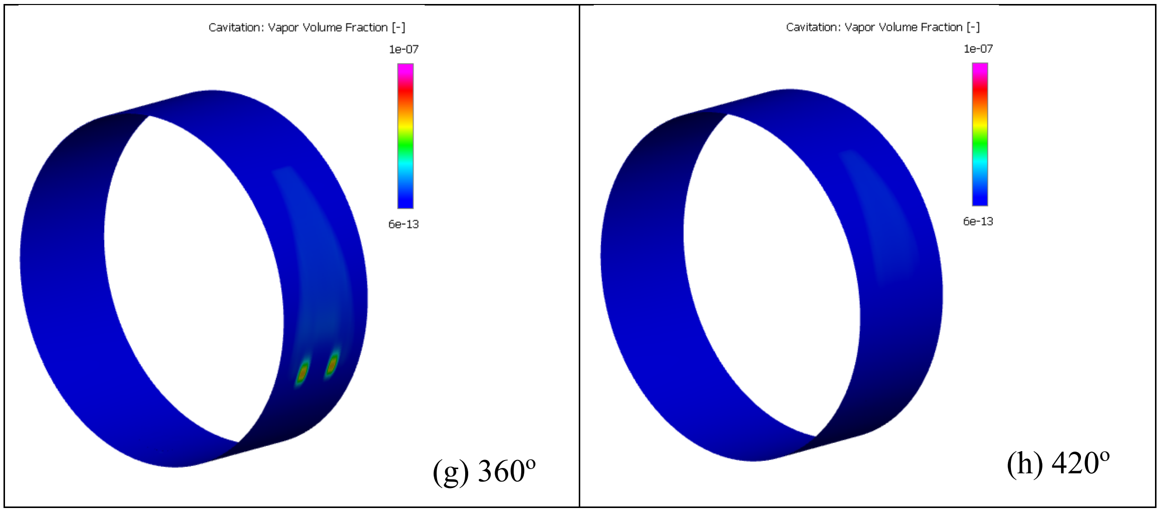

(g) 360°

(h) 420°

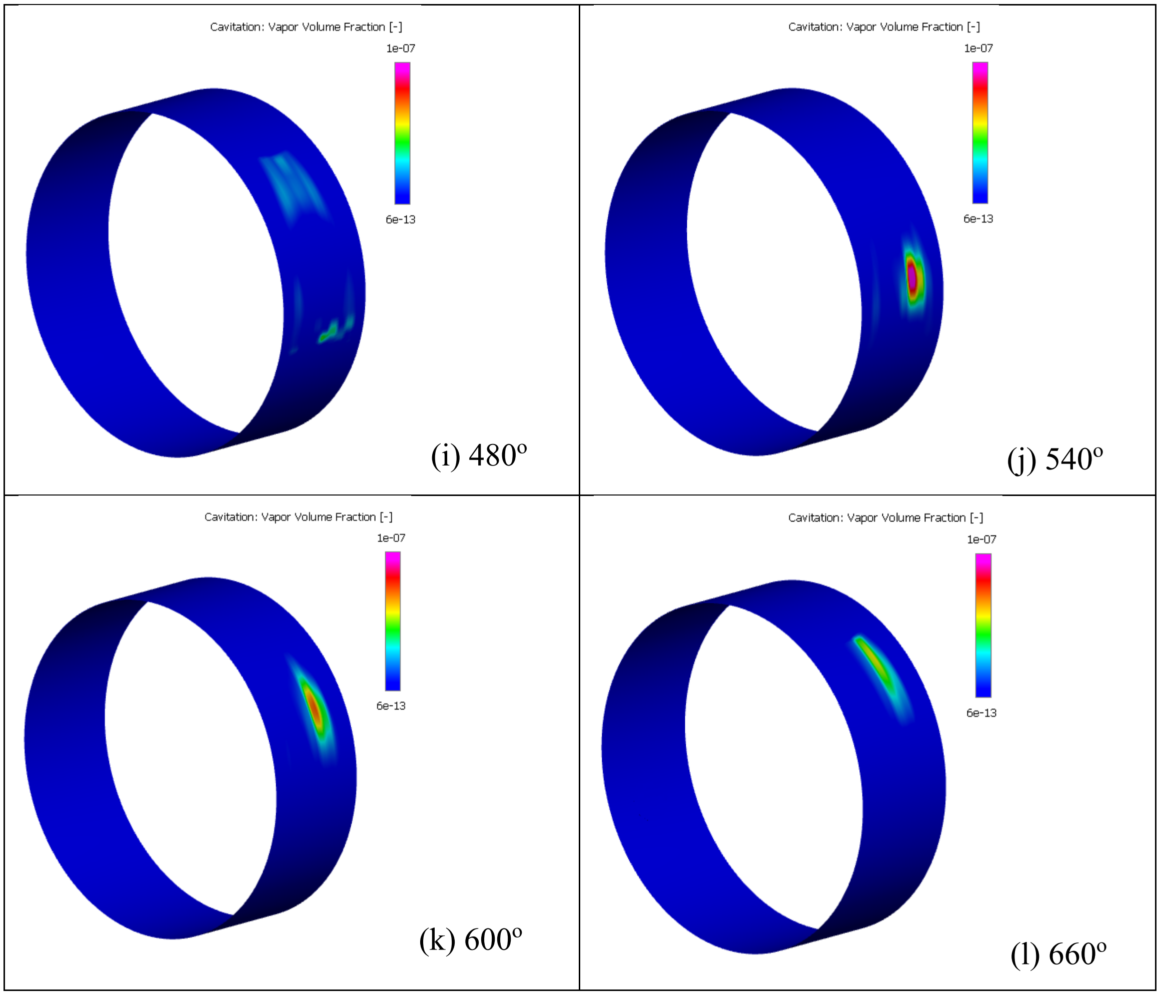

(i) 480°

(j) 540°

(k) 600°

(l) 660°

Fig. 5.30 Main bearing vapor cavitation from 360 ° to 660°

5.2.5 Conrod bearing gaseous cavitation

The conrod bearing only replies on the cross-drill for oil supple, so it will experience more oil starvation and cavitation than the main bearing. The section 5.2.5 includes the gas cavitation inside the conrod bearings over the entire working cycle. Obviously, the conrod bearing has more gaseous cavitation, and it appears at the bottom and top right quadrants.

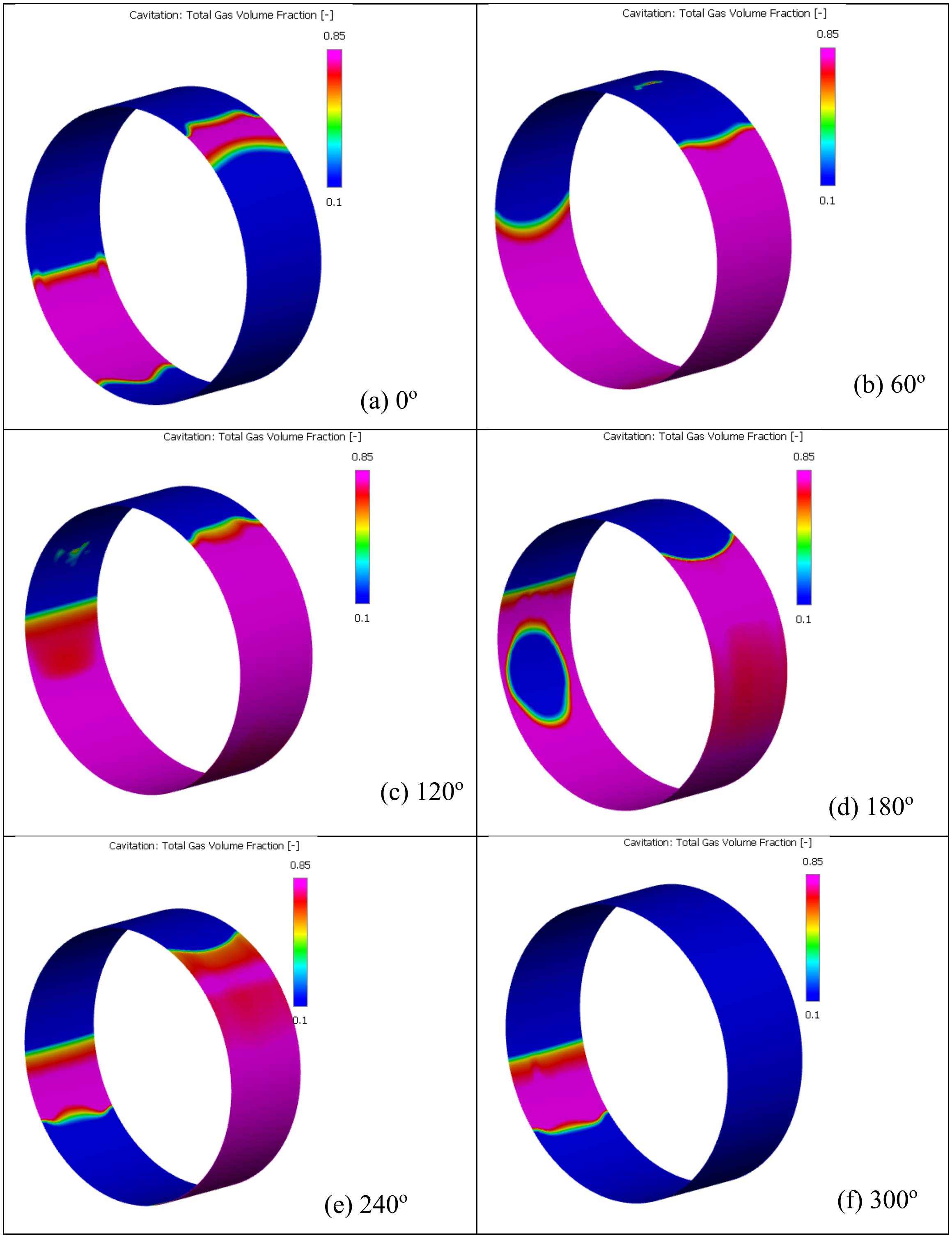

(a) 0°

(b) 60°

(c) 120°

(d) 180°

(e) 240°

(f) 300°

Fig. 5.31 Conrod bearing gaseous cavitation from 0° to 300°

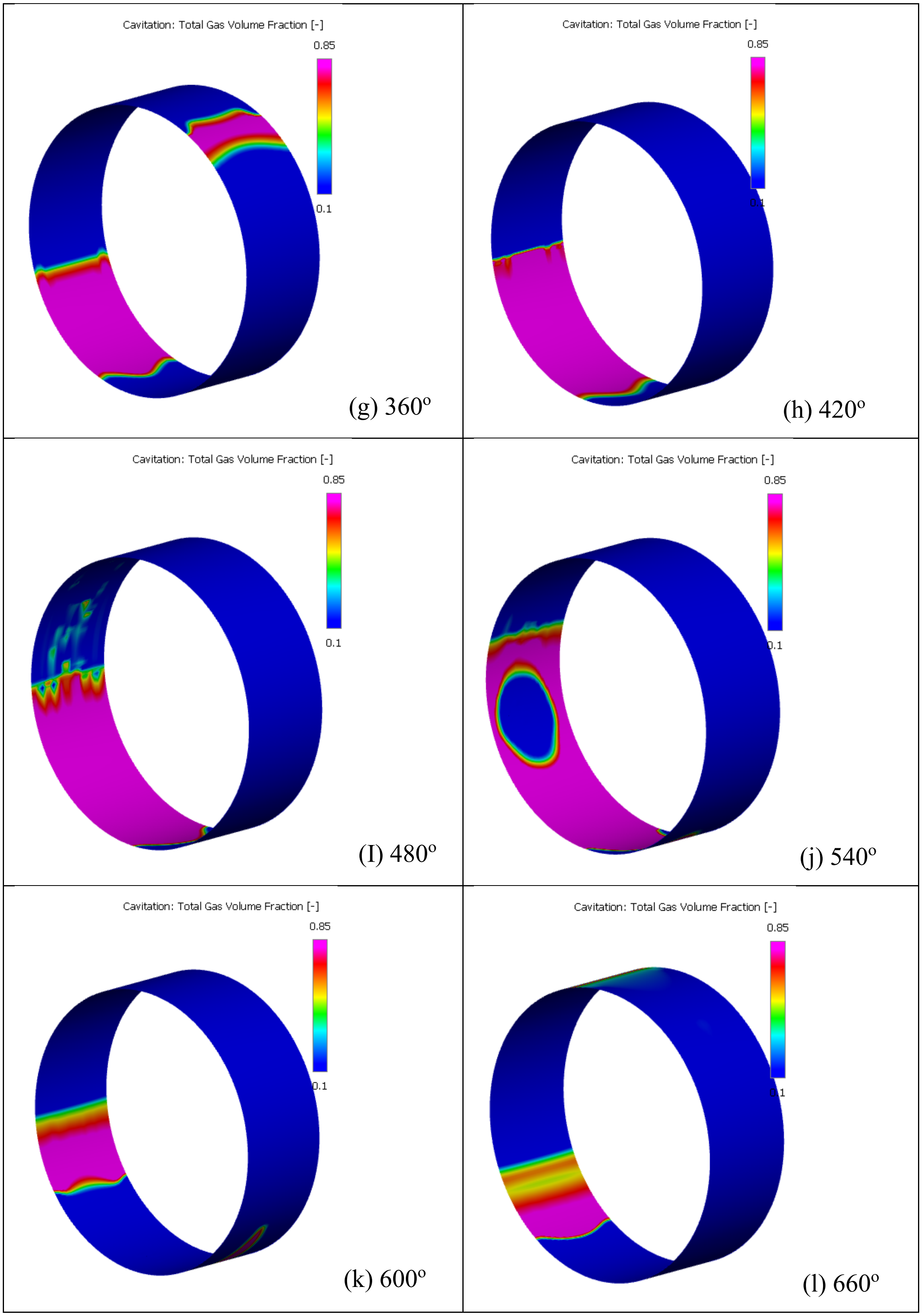

(g) 360°

(h) 420°

(I) 480°

(j) 540°

(k) 600°

(l) 660°

Fig. 5.32 Conrod bearing gaseous cavitation from 360 ° to 660°

5.2.6 Conrod bearing vapor cavitation

The vapor cavitation inside the conrod is more severe than the main bearing. The vapor cavitation fraction in the section ranges from $6x10^{-11}$ to $1x10^{-5}$. The onset of vapor cavitation usually starts from the bottom left of the conrod bearing and spreads to other regions.

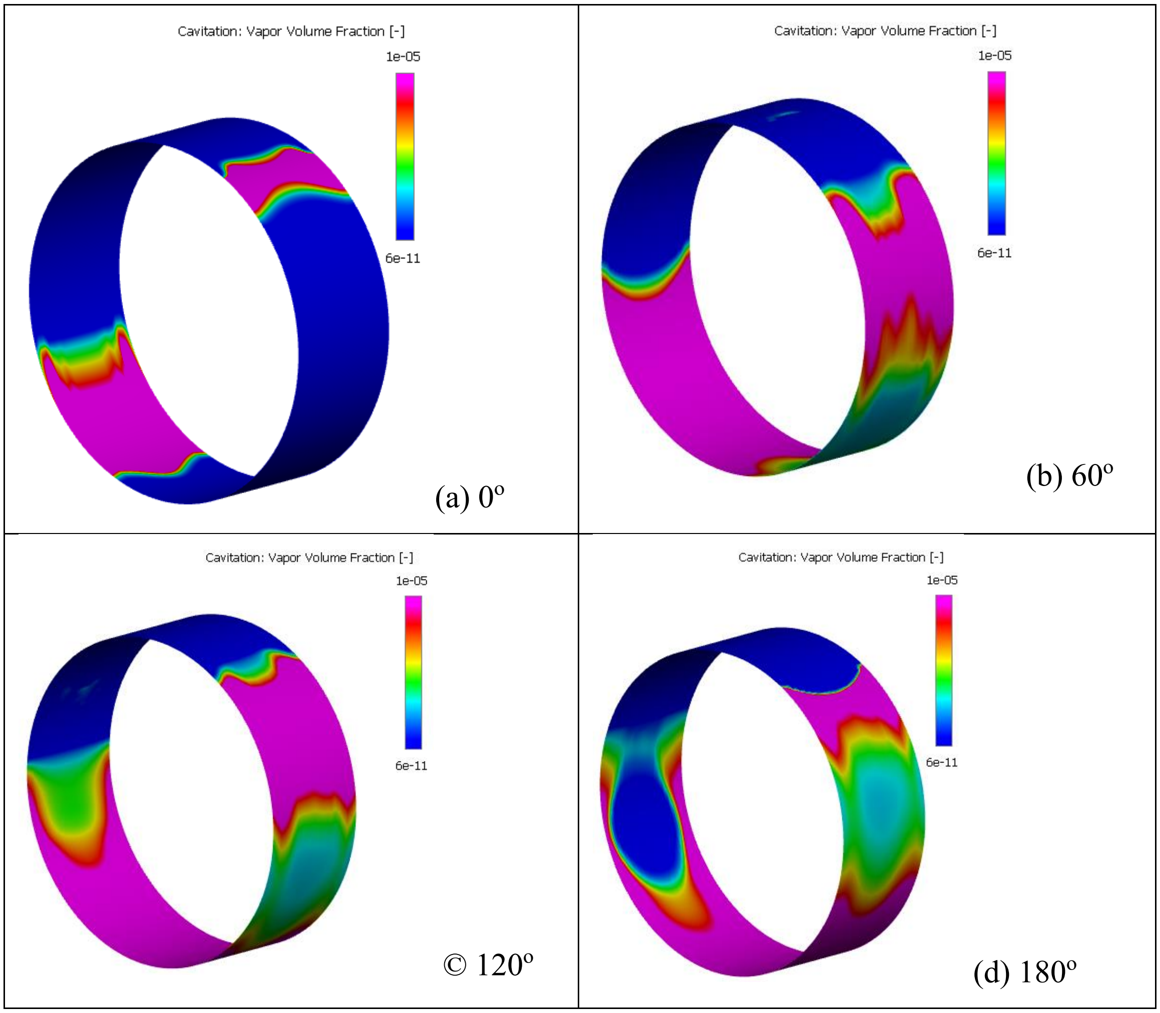

(a) 0°

(b) 60°

© 120°

(d) 180°

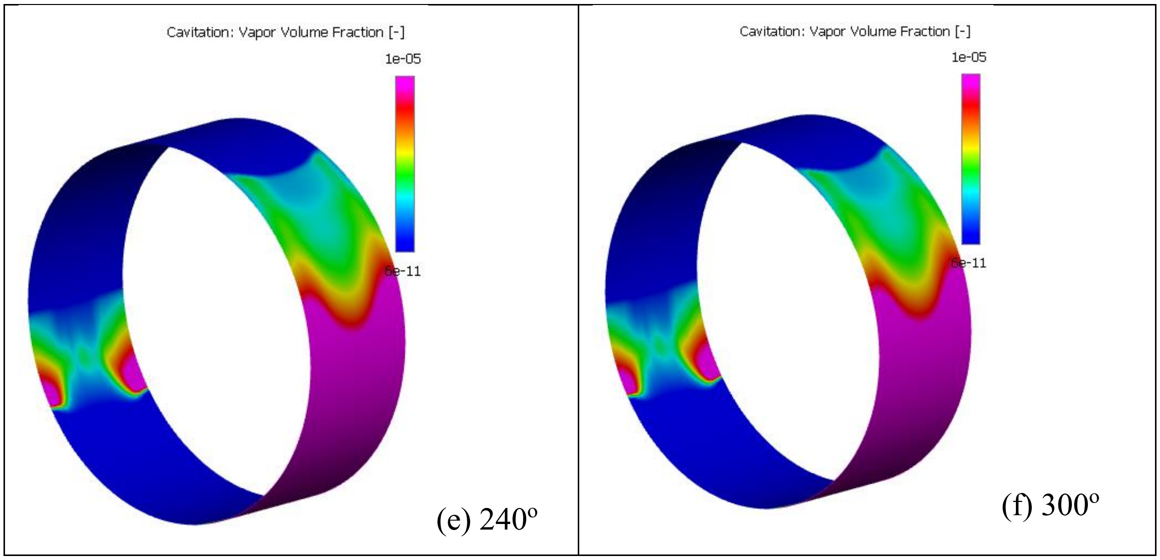

(e) 240°

(f) 300°

Fig. 5.33 Conrod bearing vapor cavitation from 0° to 300°

The snapshots from 240 to 360 degrees shows that the vapor cavitation occurs on the sides of the bearing first; then, two vapor volumes expand and merge in the middle of the bearing surface. It is because the oil supply hole on the cross-drill is in the middle of the conrod bearing. The oil supply from the cross-drill alleviates the vapor cavity in the middle.

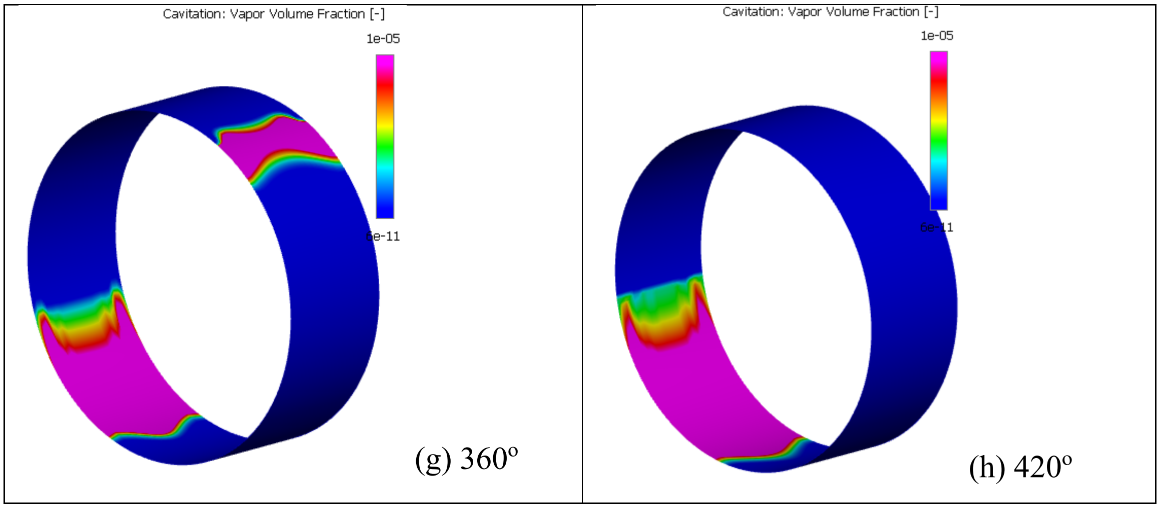

(g) 360°

(h) 420°

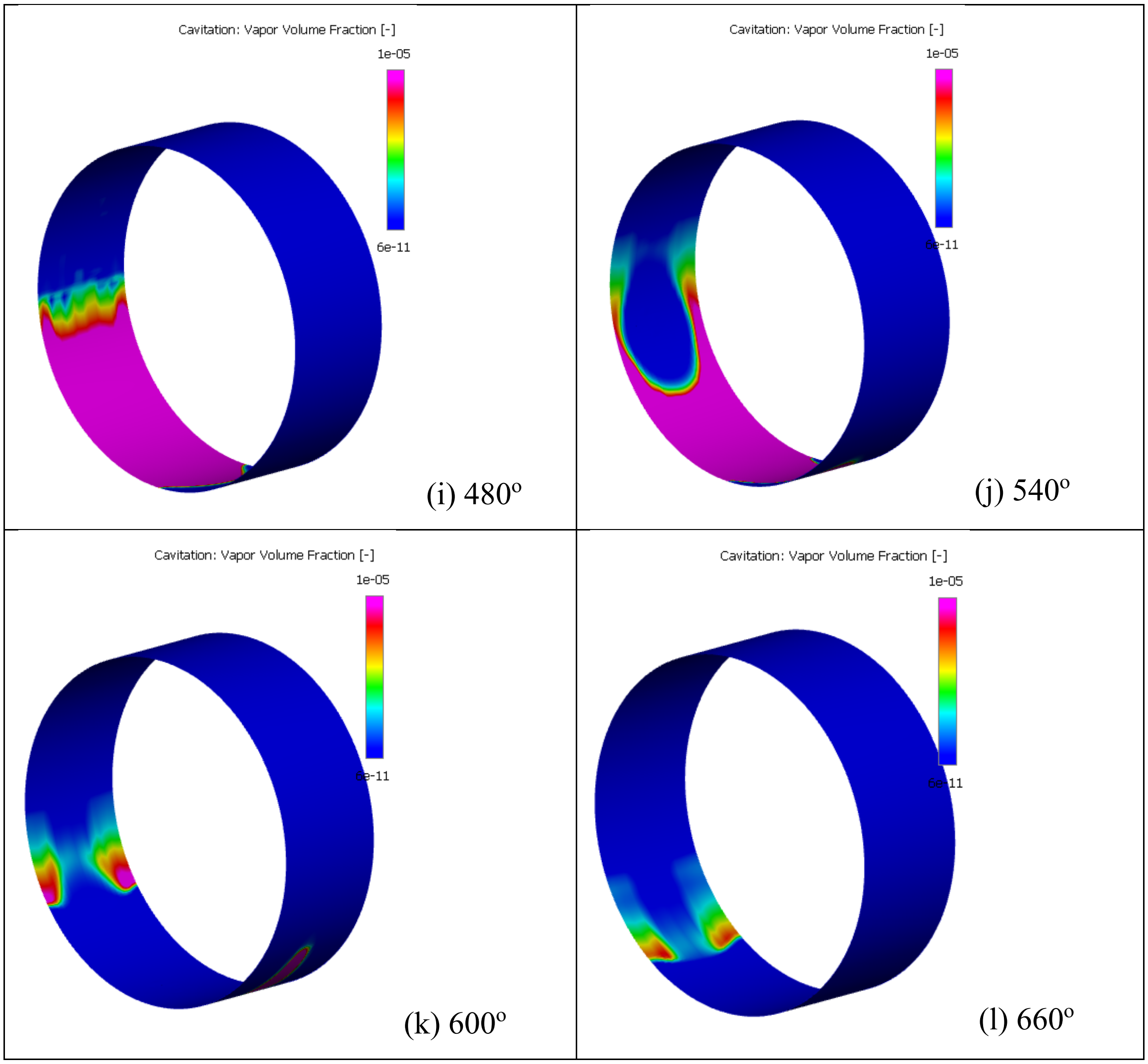

(i) 480°

(j) 540°

(k) 600°

(l) 660°

Fig. 5.34 Conrod bearing vapor cavitation from 360° to 660°

5.2.7 Bearings flow rate

The 3D simulate shows the flow rates out of the main bearing and conrod bearing are 0.361 L/min and 0.229 L/min with oil split ratio of 1.58. The 1D simulation reports corresponding flow rates as 0.298 L/min and 0.165 L/min with oil split ratio of 1.81.

This section visualizes the gaseous and vapor cavitation development inside the main and conrod bearing, respectively. The onset and severity of each cavitation are discussed. The flow rate and flow split on the bearings are also reported.

CHAPTER 6 Conclusions

- The 3D and 1D research simulation of the VDVP and bearings are conducted as stated in the objectives.
- The simulation models are correlated with the OEM experimental data. Multiple post-processing tools has been used to analyze the cavitation development and its causes inside the pump. The 3D CFD pump model shows that the cavitation develops near the vane tip and its trailing side, where the flow is more likely to separate.
- The pump cavitation sensitive responding to different inlet gas contents are tested. Generally, the cavitation starts to develop in the inlet volume, and reach the maximum quantity near the suction side of chambers. It is reported the cavitation quantities inside the cambers is corresponding to the initial gas content. The reason behind the gaseous and vapor cavitation development in each sub-section are also discussed.
- Alternative designs are tested to examine their influence on the induced cavitation. The simulation shows that Design B of the eccentricity ring geometry is favorable for introducing less cavitation. The optimal design B has the smoothest radial flow rate near the chambers, and the least induced cavitation.
- The cavitation development inside the main bearing and conrod bearings are captured and presented. With the given deformation data and 0.0225mm clearance, the gaseous cavitation is significantly larger than the vapor cavitation.
- The cavitation location is generally on the top for the main bearing, and rather scattered for the connecting rod bearing. Additionally, the connecting rod bearing has more gas volume fraction than the main bearing.
- Influence of the oil delivery on cavitation, and the cavitation development are also discussed. The groove can alleviate the development of cavitation. Upon experimentation and analyses, both the 3D and 1D simulations produced similar outlet flow rate and flow split between the main and conrod bearings with error less than 10%.
- The same methodology can be used for cavitation analysis of other pumps and bearings.

REFERENCES

[1] G. E. Totten, Y. H. Sun, R. J. Bishop and X. Lin, "Hydraulic System Cavitation: A Review," *SAE Transactions:JOURNAL OF COMMERCIAL VEHICLES (1998),* vol. 107, pp. 368-380, 1998.

[2] J.-P. Franc and J.-M. Michel, Fundamentals of Cavitation, 76 ed., KLUWER acedemic Publisher, 2004.

[3] V. Kasi, "A Review of Numerical Models for the Simulation of Cavitating Flows in Hydrofoils Master's thesis," Politecnico di Milano, Milan, 2020.

[4] R. Golf, "Kavitationsuntersuchung am DTC Propeller. Bachelor's thesis,," Universität DuisburgEssen, Duisburg, Germany, 2018.

[5] A. K. Singhal, M. M. Athavale, H. Li and Y. Jiang, "Mathematical Basis and Validation of the Full Cavitation Model," *Journal of Fluids Engineering,* vol. 124, no. 3, pp. 617-624, 2002.

[6] H. Ding, F. Visser, Y. Jiang and M. Furmanczyk, "Demonstration and Validation of a 3D CFD Simulation Tool Predicting Pump Performance and Cavitation for Industrial Applications," in *ASME Fluids Engineering Division Summer Meeting*, Vail, CO, USA, 2009.

[7] A. Krishnah, "SIMULATION OF AN ENGINE FRICTION STRIP TEST, Master's thesis," Chalmers University of Technology, Göteborg, Sweden, 2014.

[8] G. E. Totten, Y. H. Sun, R. J. Bishop and X. Lin, "Hydraulic System Cavitation: A Review," *SAE Transactions:JOURNAL OF COMMERCIAL VEHICLES (1998),* vol. 107, pp. 368-380, 1984.

[9] X. Luo, B. Ji and Y. TSUJIMOTO, "A review of cavitation in hydraulic machinery," *Journal of Hydrodynamics,* vol. 28, no. 3, 2016.

[10] R. Arndt, "Cavitation in Fluid Machinery and Hydraulic Structures," *Annual Review of Fluid Mechanics,* vol. 13, pp. 273-326, 1981.

[11] E. Frosina, A. Senatore, B. Dario and M. Olivetti, "A Tridimensional CFD Analysis of the Oil Pump of an High Performance Engine.," in *SAE Technical Papers*, Detroit, 2014.

[12] N. Nervegna and M. Rundo, Automotive fluid power systems (Slides) - Epics Edizioni (in English)., Torino: Collana Politeko (www.centroappunti.it), Reprint 2022.

[13] R. Krick, Director, *Modern Automotive Technology 7th edition.* [Film]. Tinley Park, Illionis: The Goodheart-Willcox Co., Inc.

[14] B. o. N. Personnel, "The Fleet Type Submarine Online Main Propulsion Diesels," 5 July 2007. [Online]. Available: https://archive.hnsa.org/doc/fleetsub/diesel/chap3.htm. [Accessed 08 September 2022].

[15] R. v. Basshuysen and F. Schaefer, Internal Combustion Engine Handbook, Verlag, Wiesbaden, Germany: SAE International, 2002, p. 94.

[16] M. Athavale, H. Li, J. Yu and A. K. Singhal, "Application of the Full Cavitation Model to Pumps and Inducers," International Journal of Rotating Machinery 8(1), 2002.

[17] Z. Alaswad, "Experimental and Numerical Study of a Synthetic Jet Ejector. Master's thesis.," Univerisity of Windsor, Windsor, 2019.

[18] GAMMA Technologies, "GT-SUITE," GAMMA Technologies, 2022. [Online]. Available: https://www.gtisoft.com/gt-suite/. [Accessed 18 August 2022].

[19] H. Cho, D. Jung, Z. S. Filipi, D. Assanis, J. Vanderslice and W. Bryzik, "Application of Controllable Electric Coolant Pump for Fuel Economy and Cooling Performance

Improvement," *ASME Journal of Engineering for Gas Turbines and Power,* vol. 129, no. 1, pp. 239-244, 2007.

[20] D. Buono, A. Senatore, E. Frosina, G. Buccilli and J. Harrison, "Modelling Approach on a Gerotor Pump Working in Cavitation Conditions," *Energy Procedia,* vol. 101, no. ATI 2016 - 71st Conference of the Italian Thermal Machines Engineering Association, pp. 701-709, November 2016.

[21] GT-Suite database, "Compressible Liquid Properties with Cavitation," 2022.

[22] B. A. Baran, "Engine Lubrication Oil Aeration," Massachusetts Institute of Technology, Cambridge, 2005.

[23] G. Altare and M. Rundo, "Computational Fluid Dynamics Analysis of Gerotor Lubricating Pumps at High Speed: Geometric Features Influencing the Filling Capability," *ASME J. Fluids Eng,* vol. 11, p. 138, 2016.

[24] M. Rundo, G. Altare and P. Casoli, "Simulation of the Filling Capability in Vane Pumps," *Energies,* vol. 12, no. 283, 2019.

[25] Simerics Inc., "Manual v5.1," 2020.

[26] "Application of the Full Cavitation Model to Pumps and Inducers.," 2002.

[27] A. Krishnah, "SIMULATION OF AN ENGINE FRICTION STRIP TEST," Chalmers University of Technology, Göteborg, Sweden, 2014.

Appendix A

Pressure distribution inside the crankshaft

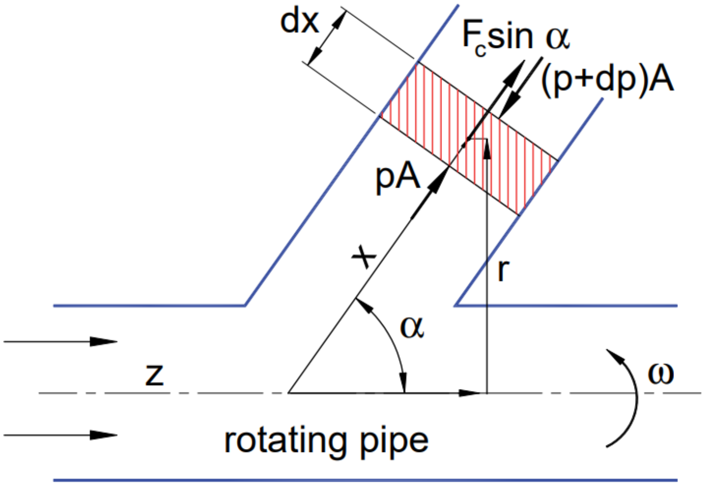

Equilibrium along the x axis

$$pA - (p + dp)A + F_c sin\alpha = 0 \tag{8}$$

Centrifugal force

$$F_c = \omega^2 r dm = \omega^2 \cdot x sin\alpha \cdot \rho A dx \tag{9}$$

$$dp = \rho(\omega \cdot sin\alpha)^2 \cdot x dx \tag{10}$$

Pressure inside the crankshaft

$$p - p_0 = \rho(\omega \cdot sin\alpha)^2 \int_{x_o}^{x} x\, dx \tag{11}$$

$$p = p_0 + \frac{1}{2}\rho\omega^2(r^2 - r_0^2) \tag{12}$$

Appendix B

The constant gas fraction model

Density of fluid-gas mixture

$$\frac{1}{\rho} = \frac{f_v}{\rho_v} + \frac{f_g}{\rho_g} + \frac{(1 - f_v - f_g)}{\rho_l} \qquad (2)$$

fg is a user defined value

ρ	Density of mixture
fv	Vapor mass fraction
fg	Non condensable gas mass fraction
l	Liquid

Mass and momentum conservation

$$\frac{\partial}{\partial \mathrm{t}} \int_{\mathrm{V}} \rho \, d\, V + \oint_{\mathrm{S}} \rho \left(\mathbf{u} - u_g \right) \cdot \, d\, s \quad = 0 \qquad (3)$$

$$\frac{\partial}{\partial t} \int_V \rho u dV + \oint_S \rho u (u - u_g) \cdot ds = \oint_S \tau \cdot ds - \oint_S p ds + \int_V F dV \qquad (4)$$

ug is the grid velocity, *V* is the control volume, and *S* is its enclosed surface. The terms on the right side of the momentum equation represent, respectively, the viscous shear force, the pressure force and the body force.

The equations are solved by the Finite Volume discretization method with SIMPLE algorithm for the velocity-pressure coupling.

This model considers Rayleigh - Plesset equation for the cavitation bubble:

$$\frac{\partial}{\partial t}\int_V \rho f_v dV + \oint_S \rho f_v (u - u_g) \cdot ds = \oint_S D_f \nabla f_v \cdot ds + \int_V (R_e - R_c)\, dV \tag{5}$$

$$R_e = C_e \frac{\sqrt{k}}{\sigma_l} \rho_l \rho_v [\frac{2}{3} \frac{(P_v - P)}{\rho_l}]^{0.5} (1 - f_v - f_g) P < P_v \tag{6}$$

$$R_c = C_c \frac{\sqrt{k}}{\sigma_l} \rho_l \rho_v [\frac{2}{3} \frac{(P - P_v)}{\rho_l}]^{0.5} f_v P > P_v \tag{7}$$

Where *Df* is the diffusivity of the vapor mass fraction. *Re* is vapor generation term and *Rc* is the condensation rate. The empirical parameter *Ce* and *Cc* are default.

Appendix C

Additional figures in Chapter 5.1.

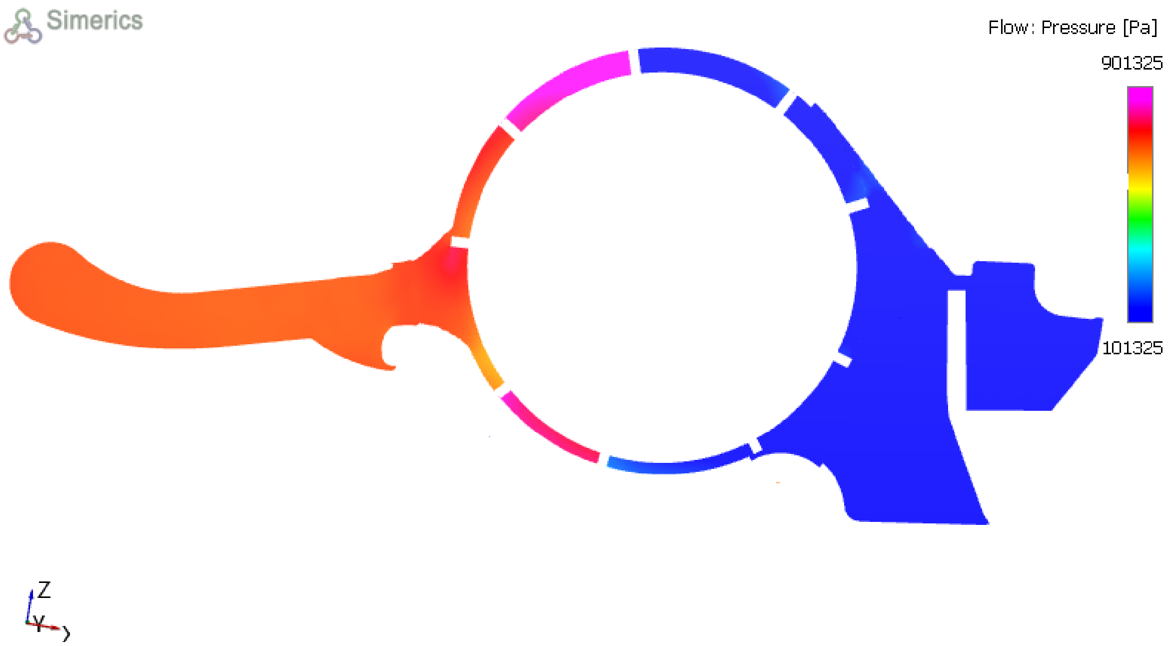

Fig. 6.1 Instantaneous pressure contour of VDVP at 5000 rpm and 100°C from 1.01×10^5 to 9.01×10^5

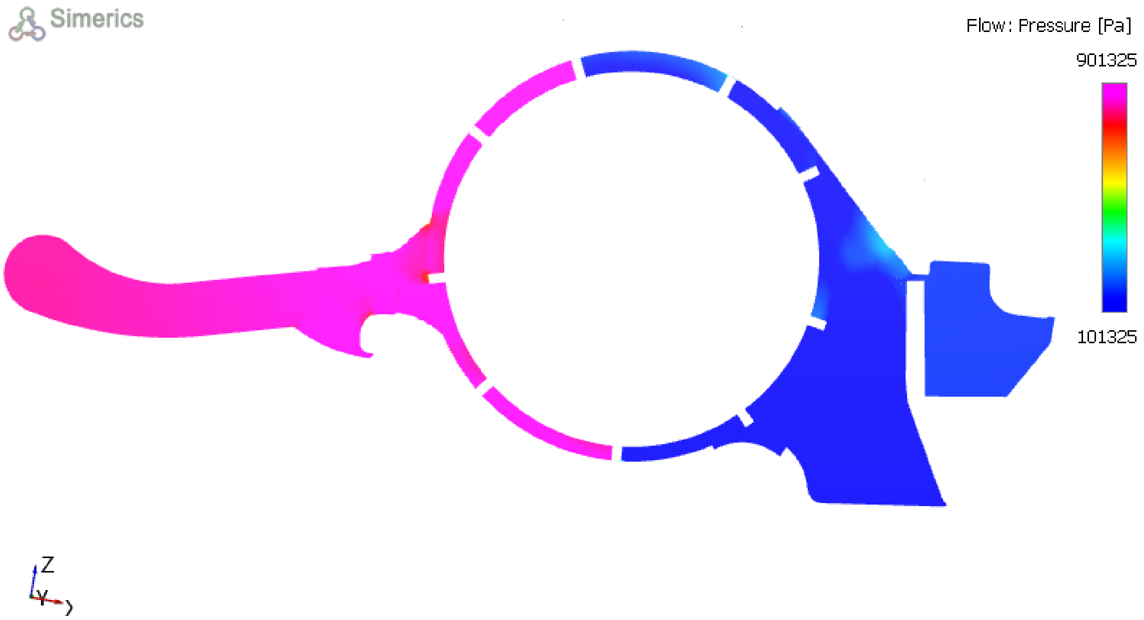

Fig. 6.2 Instantaneous pressure contour of VDVP at 5000 rpm and 50°C from 1.01×10^5 to 9.01×10^5

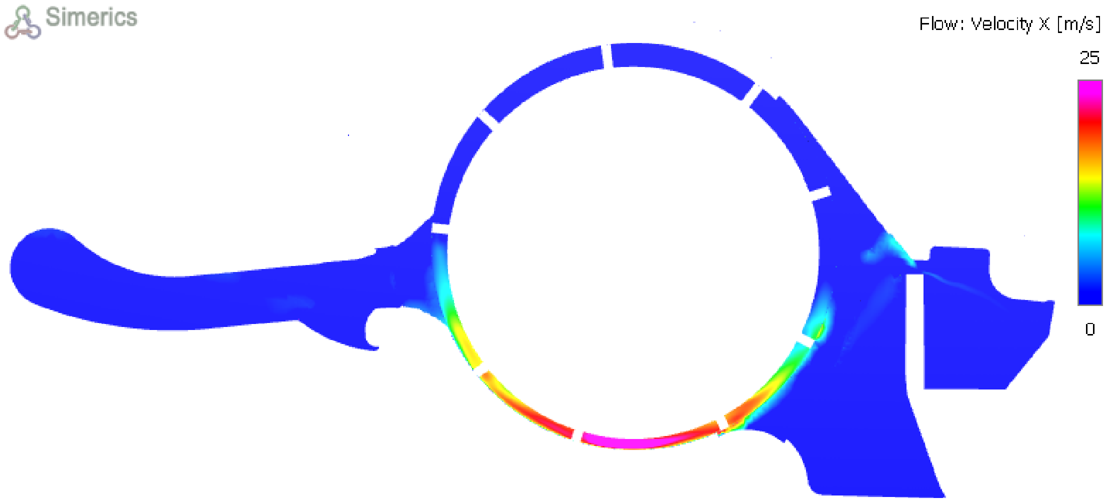

Fig. 6.3 Instantaneous velocity Vx contour of VDVP at 5000rpm and 100°C in steady state

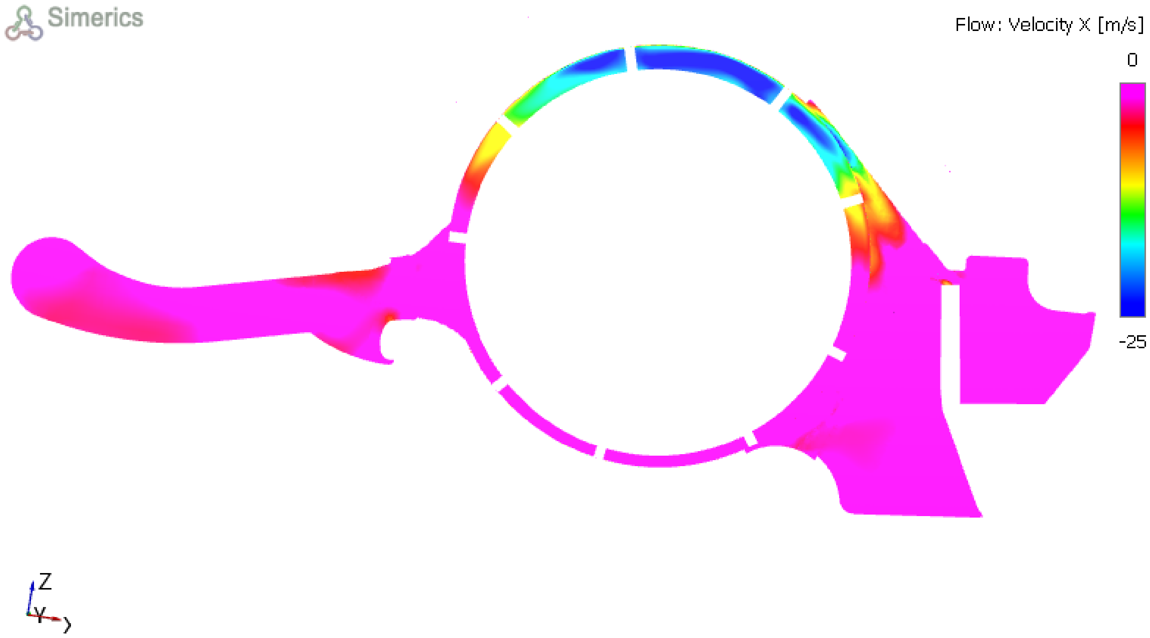

Fig. 6.4 Instantaneous velocity Vx contour of VDVP at 5000rpm and 100°C in steady state

Fig. 6.5 Instantaneous velocity Vy contour of VDVP at 5000rpm and 100ºC in steady state

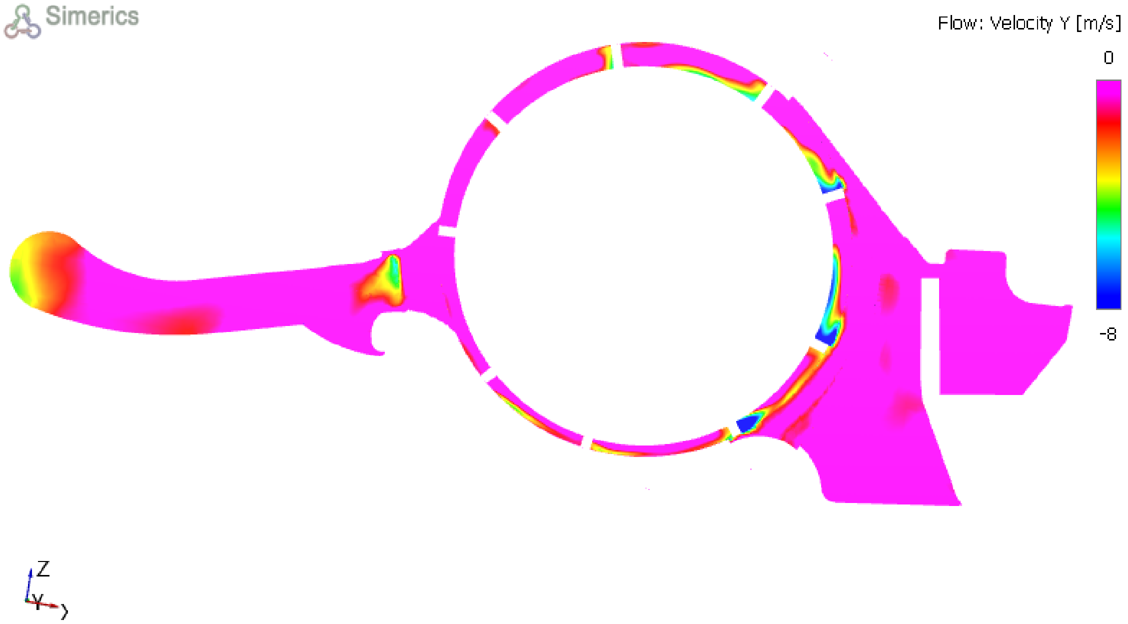

Fig. 6.6 Instantaneous velocity Vy contour of VDVP at 5000rpm and 100ºC in steady state

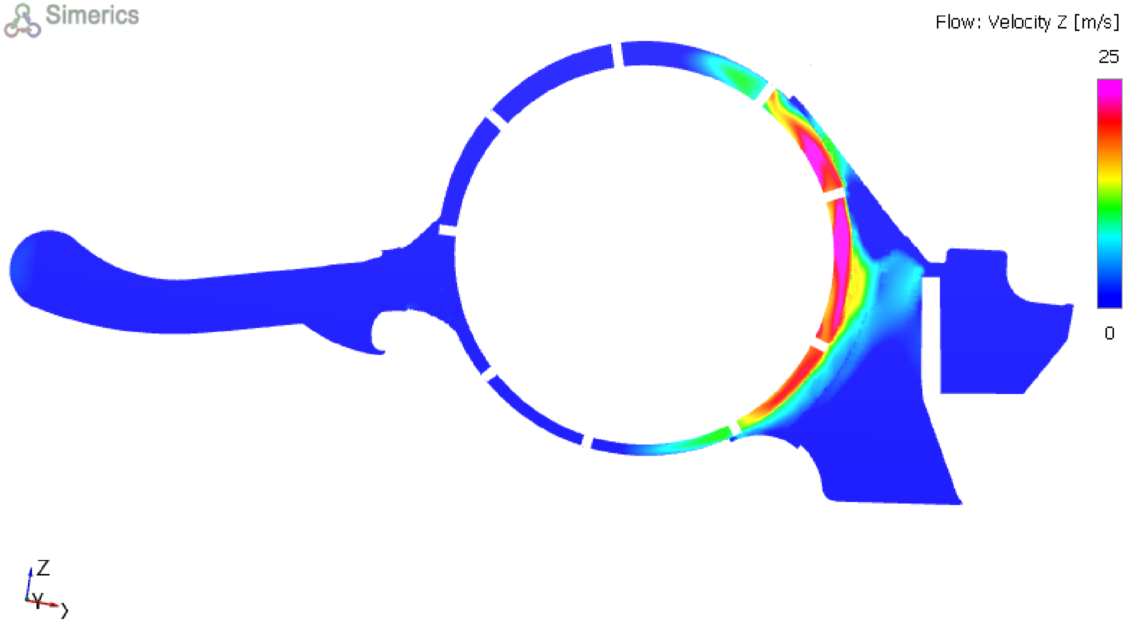

Fig. 6.7 Instantaneous velocity Vz contour of VDVP at 5000rpm and 100°C in steady state

Fig. 6.8 Instantaneous velocity V_z contour of VDVP at 5000rpm and 100°C in steady state

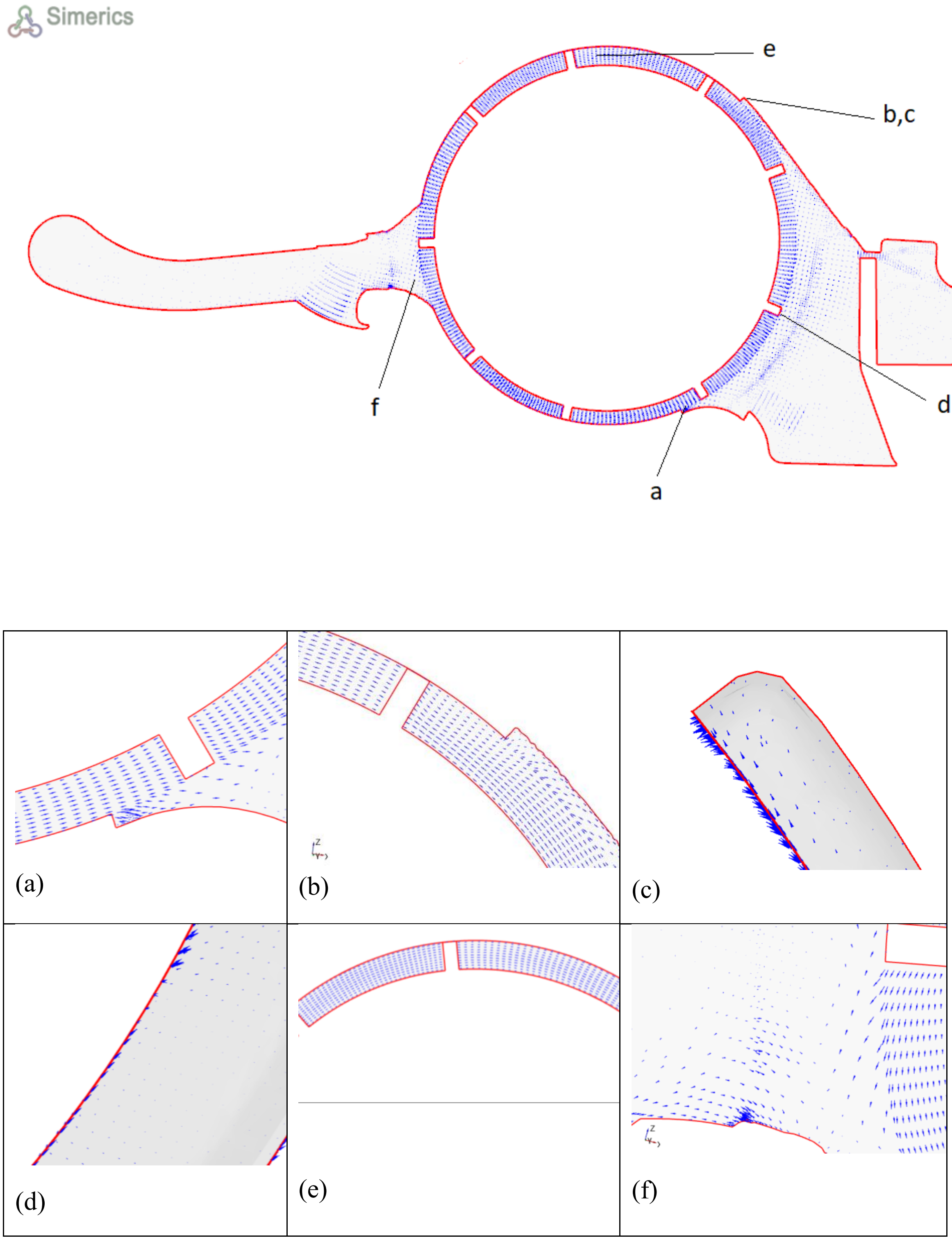

Fig. 6.9 Instantaneous velocity vectors of VDVP at 5000rpm and 50°C at the 20th revolution

VITA AUCTORIS

NAME: Jiaqi Xu

PLACE OF BIRTH: China

YEAR OF BIRTH: 1995

EDUCATION: University of Windsor, B.Sc., Windsor, ON, 2020

University of Windsor, M.Sc., Windsor, ON, 2022

Politecnico di Torino, M.Sc., Torino, Italy, 2022